Fall 2015

Space-based relative multitarget tracking

Keith Allen LeGrand

Department:

SPACE-BASED RELATIVE MULTITARGET TRACKING

by

KEITH ALLEN LEGRAND

A THESIS

Presented to the Faculty of the Graduate School of the

MISSOURI UNIVERSITY OF SCIENCE AND TECHNOLOGY

In Partial Fulfillment of the Requirements for the Degree

MASTER OF SCIENCE IN AEROSPACE ENGINEERING

2015

Approved by

Kyle Jordan DeMars, Co-advisor
Henry John Pernicka, Co-advisor
Michael Van Bredemann
Serhat Hosder

ABSTRACT

Access to space has expanded dramatically over the past decade. The growing popularity of small satellites, specifically cubesats, and the following launch initiatives have resulted in exponentially growing launch numbers into low Earth orbit. This growing congestion in space has punctuated the need for local space monitoring and autonomous satellite inspection. This work describes the development of a framework for monitoring local space and tracking multiple objects concurrently in a satellite's neighborhood. The development of this multitarget tracking systems has produced collateral developments in numerical methods, relative orbital mechanics, and initial relative orbit determination.

This work belongs to a class of navigation known as angles-only navigation, in which angles representing the direction to the target are measured but no range measurements are available. A key difference between this work and traditional angles-only relative navigation research is that angle measurements are collected from *two* separate cameras simultaneously. Such measurements, when coupled with the known location and orientation of the stereo cameras, can be used to resolve the relative range component of a target's position. This fact is exploited to form initial statistical representations of the targets' relative states, which are subsequently refined in Bayesian single-target and multitarget frameworks.

ACKNOWLEDGMENTS

I would first like to acknowledge my co-advisor Dr. Kyle DeMars. Your high expectations were unwavering, and you instilled in me a value for rigor. It has been an honor to work with you.

Secondly, I would like to thank my co-advisor Dr. Hank Pernicka. You encouraged me to start my research as a green undergraduate and provided me with more opportunities than I deserved along the way. As more than just an advisor, you have served me as a teacher, auto-mechanic, and most importantly, role model.

My deepest appreciation goes to my thesis committee members Dr. Mike Bredemann and Dr. Serhat Hosder. Thank you for your guidance and invaluable insight.

This work would not have been possible without the support of my manager Hung Nguyen and the Critical Skills Master's Program office of Sandia National Laboratories, who sponsored my graduate education.

Finally, I would like to thank my family for their persistent encouragement and genuine excitement. Specifically, I would like to thank my mother, Bonnie LeGrand, for her sincere interest in my work and her countless prayers. By this point, it is safe to say that you have read more astrodynamics papers than most kindergarten teachers.

TABLE OF CONTENTS

Page

ABSTRACT iii

ACKNOWLEDGMENTS iv

LIST OF ILLUSTRATIONS viii

LIST OF TABLES xi

SECTION

1 INTRODUCTION 1

1.1 SPACE-BASED ANGLES-ONLY NAVIGATION 1

1.2 CONTRIBUTIONS OF THE THESIS. 4

1.3 ORGANIZATION OF THE THESIS 5

2 SATELLITE RELATIVE MOTION 7

2.1 CLOHESSY-WILTSHIRE MODEL 7

2.2 SECOND-ORDER CLOHESSY-WILTSHIRE MODEL 10

3 THE RELATIVE LAMBERT PROBLEM 17

3.1 CW RELATIVE LAMBERT SOLUTION. 18

3.2 CW2 RELATIVE LAMBERT SOLUTION 20

3.2.1 Macaulay Resultant Expressions 22

3.2.2 Solution of Relative Lambert Problem Using Resultants 25

3.2.2.1 Homogenization 27

3.2.2.2 Matrix size 27

3.2.2.3 Construction of M 28

3.2.2.4 Construction of D 29

3.2.2.5 Matrix polynomial 30

3.2.3 Numerical Example 33

3.3 COMPARISON OF METHODS 35

4 STEREOSCOPIC IMAGING 44

5 SINGLE TARGET TRACKING 49

5.1 GAUSSIAN MIXTURE MODELS 50

5.1.1 Library of Solutions 51

5.2 GM APPROXIMATION OF STEREOSCOPIC MEASUREMENT UNCERTAINTY 53

5.3 LINKAGE 55

5.3.1 State Linking 55

5.3.2 Uncertainty Mapping. 57

5.4 RECURSIVE STATE ESTIMATION 61

5.4.1 Predictor. 62

5.4.2 Corrector 64

5.5 SIMULATION 66

6 MULTITARGET TRACKING 77

6.1 THE CARDINALIZED PROBABILITY HYPOTHESIS DENSITY FILTER 79

6.2 THE GAUSSIAN MIXTURE EXTENDED KALMAN CPHD 85

6.3 MEASUREMENT MODEL 89

6.3.1 Target-Originated Measurements 89

6.3.2 False Alarms 91

6.3.3 Probability of Detection 92
6.4 TARGET BIRTH 93
6.5 NUMERICAL CONSIDERATIONS AND ANALYSIS METRICS . . 99
6.5.1 GM Reduction 99
6.5.2 Cardinality Statistics 101
6.5.3 State Extraction 101
6.5.4 Multitarget Miss Distance 102
6.6 TRACKING SIMULATION 103
7 CONCLUSIONS 113
APPENDIX 116
BIBLIOGRAPHY 118
VITA 125

LIST OF ILLUSTRATIONS

Figure Page

2.1 Inspector/Target orbit geometry.. 9

3.1 Relative motion of target spacecraft over time.. 17

3.2 Illustration of cross-track velocity ambiguity in half-period multiple times of flight. 19

3.3 Geometric representation of f_1, f_2 and f_3 polynomial surfaces.. 23

3.4 The resultant polynomial roots correspond to the possible $\dot{z}_0$ solutions. . . . 34

3.5 Trajectories of solutions given by Clohessy-Wiltshire, second order Clohessy-Wiltshire, and traditional Lambert solvers 36

3.6 Flow chart of traditional Lambert approach to relative Lambert problem. . 37

3.7 Miss distances of Lambert solvers with constant t_f and $z_{f,\text{des}}$. 38

3.8 Miss distance histograms for the three Lambert solver methods.. 40

3.9 Histograms of the best 95% miss-distance solutions.. 41

3.10 The complete set of miss-distances, arranged by $\psi = n_0(t_f - t_0)$. 42

4.1 Centroid image coordinates and angle measurement deviations shown in image frame. 44

4.2 The stereoscopic LOS geometry. 45

4.3 Typical non-Gaussian distribution of triangulated positions generated from Gaussian-distributed angular measurements. 47

5.1 GM approximation of a uniform pdf for different numbers of components. . 52

5.2 Uncertainty bounding of bearings-only measurements. 53

5.3 Gaussian mixture approximating uniform uncertainty $\in \rho_{\min} \leq \rho \leq \rho_{\max}$. . 54

5.4 Gaussian mixture linkage between t_1 and t_2. 59

5.5 Block representation of the GM pdf construction and refinement algorithm. 67

5.6 True relative motion of target in Hill frame using two-body dynamics . . . 68

5.7 Position and velocity pdfs at $t_1 = 3350\,[\mathrm{s}]$. The truth is denoted by the cross markers.. 69

5.8 Overlaid position and velocity RSS over 100 runs of same orbit.. 70

5.9 Overlaid position and velocity error over 100 runs of same orbit. 71

5.10 Camera baseline study: average position and velocity uncertainty. 72

5.11 Number of initial components generated as a function of linkage Δt and along-track separation. 73

5.12 For very large initial relative ranges, the LOS vectors approach equivalence, requiring more components in the construction. 74

5.13 RSS of initial pdf as a function of linkage Δt and along-track separation. . 75

5.14 Shannon entropy, H_s, of initial pdf as a function of linkage Δt and along-track separation. 76

6.1 Due to the PHD filter's Poisson approximation of target cardinality, higher target numbers result in higher cardinality variance. 80

6.2 Block representation of the multitarget measurement structure. 82

6.3 Example of image processing subsystem output for a single target. 90

6.4 Example of false matches.. 91

6.5 Block diagram of space-based relative multitarget tracking framework. . . . 97

6.6 Example of one birth with two existing targets. 98

6.7 Relative position histories 105

6.8 Initial relative position and velocity intensities. 105

6.9 PHD and CPHD cardinality estimates and true target cardinality. 106

6.10 CPHD cardinality statistics. 107

6.11 Comparison of x-coordinate position estimates to the true x-coordinate position histories.. 108

6.12 Comparison of y-coordinate position estimates to the true y-coordinate position histories.. 108

6.13 Comparison of x-coordinate position estimates to the true x-coordinate position histories.. 109

6.14 Comparison of y-coordinate position estimates to the true y-coordinate position histories.. 109

6.15 First-order OSPA metric with cutoff $c = 10\,[\mathrm{m}]$. 111

6.16 Nondimensionalized recursion execution times.. 112

LIST OF TABLES

Table Page

6.1 Explanation of $\Upsilon_k^u[v, \boldsymbol{Y}](n)$, the likelihood of the multitarget observation $\boldsymbol{Y}$ given that there are n targets. 85

6.2 Initial relative states of targets. 104

1. INTRODUCTION

The eruption of the small satellite and cubesat markets has caused a dramatic global increase in the satellite launch tempo. In fact, the number of micro- and nanosatellites launched has grown exponentially each year since 2011 [1]. The small size, mass, and cost of small satellites have enabled new mission concepts that were once considered infeasible due to the restrictive cost of "big" satellites. Specifically, a number of small satellite constellations has recently been proposed [2–4]. Although these constellations promise great utility, the consequential congestion and collision threats are a cause of concern to many satellite operators. Many of these objects are tracked from ground-based RADAR and telescopes [5–8]. However, the ability for a satellite to track nearby objects without ground intervention and mitigate collision threats has obvious advantages.

1.1. SPACE-BASED ANGLES-ONLY NAVIGATION

Satellite proximity operations have been actively researched since the 1960s [9–11]. The ability to accurately track and predict the motion of nearby space objects is necessary for surveillance, inspection, formation flight, rendezvous, docking, and satellite servicing. Recent research has given special focus to accurate relative motion tracking and prediction using only angles data [12, 13]. As the name implies, angles-only navigation systems operate in the absence of range measurements, estimating the motion of a nearby target using only a time-history of noisy angular measurements typically taken from an optical navigation camera. For many applications, angles-only systems may be advantageous over ranging systems, such as RADAR. For instance, in uncooperative proximity operations, the passive nature of angles-only sensors may be preferable over active ranging sensors that are detectable by the target satellite. Furthermore, the required electromagnetic emission of most ranging

systems contributes to generally higher power consumption than comparable angles-only systems. For this reason, in small satellite designs with limited power availability, lower-power angles-only systems are often more attractive.

Angles-only navigation research is conducted on multiple fronts. For example, many efforts focus on the development of accurate and computationally efficient relative motion models [9, 11, 14, 15]. Perhaps the simplest and most popular relative satellite motion model is the Clohessy-Wiltshire (CW) model [16]. The CW model is linear, admits a closed-form general solution, and its equations are easily interpretable. Drawbacks of the model include the assumptions of simple two-body motion and a circular inspector orbit, although the negative effects of these assumptions can be mitigated by proper filter design [17]. A close variant of the CW model is the second-order Clohessy-Wiltshire (CW2) model [18]. Although the CW2 model makes the same dynamical assumptions as the CW model, it retains higher-order terms in its approximation whilst very computationally efficient and thus offers modest improvements over the CW model in its agreement to the reference two-body motion.

Another major focus of space-based angles-only navigation research is initial relative orbit determination (IROD). IROD is the process of initializing the state estimates that define the relative orbit of a target (most commonly, relative position and velocity). In general, angles-only IROD is performed deterministically [19] or by batch-processing a sequence of angular measurements to form an initial state estimate and covariance [12].

In past years, much research has been dedicated to the observability issues inherent of angles-only IROD under the CW model [20–23]. References [21] and [22] have shown that the Cartesian states representing the relative position and velocity of a target satellite are unobservable when all of the following common assumptions are made:

A1. The motion of the target satellite is modeled using the CW equations.[1]

A2. Angular measurements are taken in reference to the center of mass of the inspector satellite.

A3. No calibrated thrust maneuvers are performed by the inspector satellite.

Under the preceding assumptions, in a given relative orbital plane, an infinite number of relative orbits produce the same angular measurement history. In theory, the higher-order terms found in the CW2 model mitigate this ambiguity, thus relaxing Assumption A1. The use of the nonlinear CW2 equations in place of the linear CW model theoretically allows the relative states to be observed. However, existing angles-only CW2-based IROD methods fail in the presence of modest measurement noise, likely due to the inability to resolve and exploit the subtle differences in the CW and CW2 models [24].

One promising approach to angles-only proximity operations is through the relaxation of Assumption A2 by using a dual-camera system, or stereoscopic imager [25–27], as recently demonstrated with a single target by the Visual Estimation for Relative Tracking and Inspection of Generic Objects (VERTIGO) program [28]. The VERTIGO program, which was conducted in the Synchronized Position Hold, Engage, Reorient, Experimental Satellites (SPHERES) laboratory onboard the International Space Station, demonstrated the first fully autonomous robotics vision-based navigation strategy with a noncooperative spacecraft [28].

In this study, both Assumptions A1 and A2 are relaxed. Target satellite motion is modeled using the nonlinear CW2 equations, and angles-only measurements are taken of the targets from an inspector-hosted stereoscopic imager. A unique

[1]This includes derivative models expressed in alternative element sets that, nonetheless, obey the CW equations of motion.

method for performing IROD using stereoscopic measurements is presented. The presented IROD method accepts multiple relative motion models, and two examples are discussed. Both methods require the relative Lambert problem to be solved, which consists of finding the set of relative velocity solutions that satisfy a pair of temporally-separated relative position vectors and the associated time of flight. The relative Lambert solution under CW model assumptions is reviewed, and the solution for the CW2 relative Lambert problem is presented and analyzed.

Frameworks for angles-only navigation are established for single-target and multitarget tracking using Gaussian mixture (GM) filters. For single-target tracking, a Gaussian mixture square-root unscented Kalman filter (GMSRUKF) is employed to track *single* targets to high accuracy using angles-only data. A multitarget architecture for performing space-based angles-only tracking of *multiple* targets is then presented that makes use of recent developments in intensity filtering, namely the cardinalized probability hypothesis density (CPHD) filter.

1.2. CONTRIBUTIONS OF THE THESIS

In the pursuit of the space-based multitarget tracking solution presented in this work, collateral studies are performed in algebraic systems, relative orbital mechanics, and statistical IROD. The relative Lambert problem is formulated using CW2 mechanics and casted as a multivariate polynomial root-finding problem. To solve this polynomial system, a unique method for solving n multivariate polynomials with n unknowns is developed using Macaulay resultant expressions. While the application of Macaulay resultants to solve multipolynomial systems is not altogether new, a new and clear approach to the resultant matrix construction is presented that avoids the shortcomings and ambiguities of existing methods. The resultant method is employed to find all solutions to the second-order relative Lambert problem without introducing fictitious solutions. To the best of the author's knowledge, the applica-

tion of Macaulay resultants to the second-order relative Lambert problem is the first documented use of resultant theory in aerospace engineering.

The relative Lambert solver plays a critical role in the novel bearings-only IROD architecture, by "linking" together two temporally-separated parameterized probability density functions (pdfs). While many IROD methods predate this work, the presented framework is the first to leverage the statistical power of GMs.

Space-based tracking of a single satellite is a well-studied research problem. However, studies in multiple satellite tracking are largely found in the context of ground-based systems. In fact, to the best of the author's knowledge, this work is the first documented effort in space-based multitarget tracking. The presented multitarget tracking architecture is developed under the CPHD framework, and its performance is compared to a similar architecture based on the probability hypothesis density (PHD).

1.3. ORGANIZATION OF THE THESIS

This thesis is composed as follows:

- In Chapter 2, satellite relative motion is reviewed, and abbreviated derivations of the CW and CW2 relative motion models are provided.

- In Chapter 3, the relative Lambert problem is formulated. The solution for the relative Lambert problem under the CW model is provided in Section 3.1. In Section 3.2, Macaulay resultant expressions are introduced and applied to solve the CW2 relative Lambert problem. A comparison of the CW solver, CW2 solver, and an alternative solver based on the classic Lambert problem is presented in Section 3.3.

- In Chapter 4, the fundamentals of stereoscopic imaging are reviewed. A mathematical model for synthesizing stereoscopic measurements is established, and the limitations of typical stereoscopic triangulation approaches are discussed.

- In Chapter 5, a framework for tracking a single target from a space-based stereoscopic platform is presented. GMs and their applications to stereoscopic measurement uncertainty are discussed in Sections 5.1 and 5.2, respectively. In Section 5.3, using GM approximations to model relative range uncertainty at two measurement times, a relative Lambert problem is used to link two temporally-separated positional pdfs and produce a full-state pdf in relative position and velocity. Further pdf refinement is achieved recursively via processing angles-only measurements in the GMSRUKF. Simulations of the IROD process and single-target recursive estimation are presented and discussed in Section 5.5.

- In Chapter 6, the concepts developed in Chapter 5 are extended to multiple targets. The multitarget CPHD intensity filter is presented and thoroughly detailed. The necessary models for the intensity filters, including the measurement clutter model (Section 6.3.2), probability of detection model (Section 6.3.3), and target birth model (Section 6.4) are developed. In Section 6.6, the performance of the PHD and CPHD filters is investigated in the context of a simulated debris cloud tracking problem.

- In Chapter 7, simulation results are summarized and conclusions are compiled.

2. SATELLITE RELATIVE MOTION

For many multiple-satellite missions, determining the relative motion of a nearby satellite is more important and often more convenient than determining the inertial motion of one or more of the satellites. For instance, when docking to a spacecraft such as the International Space Station (ISS), the position and velocity *relative* to the approaching spacecraft must be known to extremely high accuracy to ensure a safe docking. On the other hand, a less accurate knowledge of the spacecraft's specific orbital position may be acceptable.

Far too many relative motion models have been documented in the literature to cite all in this thesis. One of the first satellite relative motion models to be introduced (and perhaps the first) is the Clohessy-Wiltshire (CW) model, and it remains the most widely used to date. Some notable models accommodate eccentric orbits [29], while others capture perturbations such as the nonspherical gravitational forces due to Earth's oblateness [15]. In this study, the standard CW model is considered as well as a newer model known as the second-order Clohessy-Wiltshire (CW2) model, which captures higher-order terms neglected in the CW model.

2.1. CLOHESSY-WILTSHIRE MODEL

The inertial motion of the inspector and target spacecraft are assumed to be unperturbed such that the motion may described using two-body dynamics as

$$\ddot{\mathbf{r}}_{\text{ins}} = -\frac{\mu \mathbf{r}_{\text{ins}}}{\mathrm{r}_{\text{ins}}^3} \qquad \text{and} \qquad \ddot{\mathbf{r}}_{\text{tgt}} = -\frac{\mu \mathbf{r}_{\text{tgt}}}{\mathrm{r}_{\text{tgt}}^3}\,, \tag{2.1}$$

where μ is the gravitational parameter of the central body, $\mathbf{r}$ is the inertial position of the satellite with respect to the two-body system center of mass (taken to be Earth's center), and the subscripts "ins" and "tgt" denote the inspector and target satellites,

respectively. The relative position of the target satellite with respect to the inspector is defined as

$$\delta\mathbf{r} \triangleq \mathbf{r}_{\text{tgt}} - \mathbf{r}_{\text{ins}} \,.$$

Differentiating twice with respect to time and substituting Equations (2.1) yields the differential acceleration

$$\delta\ddot{\mathbf{r}} = \ddot{\mathbf{r}}_{\text{tgt}} - \ddot{\mathbf{r}}_{\text{ins}} = \frac{\mu}{{\text{r}_{\text{ins}}}^3}\left[\mathbf{r}_{\text{ins}} - \frac{{\text{r}_{\text{ins}}}^3}{{\text{r}_{\text{tgt}}}^3}\mathbf{r}_{\text{tgt}}\right] \,. \tag{2.2}$$

Making the substitution $\mathbf{r}_{\text{tgt}} = \mathbf{r}_{\text{ins}} + \delta\mathbf{r}$, expanding, and neglecting terms on the order $\mathcal{O}(\|\delta\mathbf{r}\|^2)$ and higher yields

$$\delta\ddot{\mathbf{r}} = -\frac{\mu}{{\text{r}_{\text{ins}}}^3}\left(\delta\mathbf{r} - 3x\hat{R}\right) \,, \tag{2.3}$$

where $\hat{R}$ is the unit vector pointing radially in the direction of $\mathbf{r}_{\text{ins}}$, and x is the component of the relative position vector in the $\hat{R}$ direction [30]. Note that Equation (2.3) is the differential *inertially referenced* acceleration. It is convenient to express the relative motion of the target spacecraft in terms of the rotating Hill frame (see Figure 2.1), which is centered about the inspector spacecraft. To that end, the basic kinematic equation is used to express the relative acceleration of the target spacecraft as

$$\delta\ddot{\mathbf{r}}_R = -2\boldsymbol{\omega} \times \delta\dot{\mathbf{r}} - \boldsymbol{\omega} \times (\boldsymbol{\omega} \times \delta\mathbf{r}) - \dot{\boldsymbol{\omega}} \times \delta\mathbf{r} + \delta\ddot{\mathbf{r}} \,, \tag{2.4}$$

where $\boldsymbol{\omega}$ is the angular velocity of the rotating Hill frame with respect to the inertial frame.

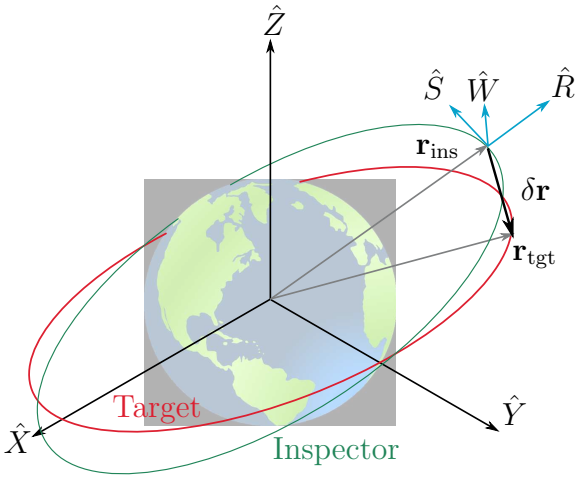

Figure 2.1. Inspector/Target orbit geometry. The Hill frame rotates with the inspector and is defined by the axes $\hat{R}$-$\hat{S}$-$\hat{W}$. The $\hat{R}$ axis (radial) extends the inspector's geocentric position vector. The $\hat{W}$ axis (cross-track) is normal to the orbital plane and points in the direction of the geocentric specific angular momentum vector. The $\hat{S}$ axis (along-track) completes the triad, and for circular orbits, is parallel to the inspector's inertial velocity vector.

Assuming that the inspector's orbit is nearly circular, the magnitude of the frame's angular velocity is constant and equal to the orbital mean motion, such that

$$\boldsymbol{\omega} = [0,\, 0,\, n]^T \qquad \text{and} \qquad \dot{\boldsymbol{\omega}} = \mathbf{0}\,, \tag{2.5}$$

where $n = \sqrt{\mu/({R_{\text{ins}}}^3)}$ and $R_{\text{ins}} = \|\mathbf{r}_{\text{ins}}\|$. With the substitution of Equations (2.3) and (2.5), Equation (2.4) can be written in component form as

$$\ddot{x} - 2n\dot{y} - 3n^2 x = 0 \tag{2.6a}$$

$$\ddot{y} + 2n\dot{x} = 0 \tag{2.6b}$$

$$\ddot{z} + n^2 z = 0\,, \tag{2.6c}$$

noting that $\delta\ddot{\mathbf{r}}_R = [\ddot{x},\, \ddot{y},\, \ddot{z}]^T$. The coordinates x, y, and z represent the Hill frame-referenced relative displacements of the target satellite in the radial $\hat{R}$, along-track $\hat{S}$, and cross-track $\hat{W}$ directions, respectively. Equations (2.6) are most commonly referred to as the Clohessy-Wiltshire (CW) equations, or in some literature, Hill's equations. The general closed-form solutions of the CW equations are

$$x(t) = \frac{\dot{x}_0}{n_0}\sin(\psi) - \left(3x_0 + \frac{2\dot{y}_0}{n_0}\right)\cos(\psi) + \left(4x_0 + \frac{2\dot{y}_0}{n_0}\right) \tag{2.7a}$$

$$y(t) = \left(6x_0 + \frac{4\dot{y}_0}{n_0}\right)\sin(\psi) + \frac{2\dot{x}_0}{n_0}\cos(\psi) - (6n_0x_0 + 3\dot{y}_0)t + \left(y_0 - \frac{2\dot{x}_0}{n_0}\right) \tag{2.7b}$$

$$z(t) = z_0\cos(\psi) + \frac{\dot{z}_0}{n_0}\sin(\psi)\,, \tag{2.7c}$$

where

$$\psi \triangleq n_0(t - t_0), \qquad C_\psi \triangleq \cos(\psi)\,, \qquad S_\psi \triangleq \sin(\psi)\,,$$

and n_0 is the mean motion of the inspector satellite evaluated at t_0, which is constant under the circular orbit assumption.

2.2. SECOND-ORDER CLOHESSY-WILTSHIRE MODEL

To obtain Equation (2.3), approximations are made by performing a first-order binomial expansion and dropping terms on the order of $\mathcal{O}(\|\delta\mathbf{r}\|^2)$ and higher. Alternatively, Equation (2.4) can be written as [18]

$$\delta\ddot{\mathbf{r}}_R \approx \boldsymbol{a}_K + \boldsymbol{a}_{J0}\,, \tag{2.8}$$

where $\boldsymbol{a}_K$ is a collection of the three kinematic terms in Equation (2.4) and $\boldsymbol{a}_{J0}$ is an alternative higher-order approximation of the differential acceleration due to spherical

gravity. The relative kinematic acceleration is written in matrix form as

$$\boldsymbol{a}_K = \begin{bmatrix} \boldsymbol{A}_{K\delta \mathrm{r}} & \boldsymbol{A}_{K\delta \dot{\mathrm{r}}} \end{bmatrix} \begin{bmatrix} \delta \mathbf{r} \\ \delta \dot{\mathbf{r}} \end{bmatrix}, \tag{2.9}$$

where

$$\boldsymbol{A}_{K\delta \mathrm{r}} \triangleq n_0^2 \begin{bmatrix} 1 & 0 & 0 \\ 0 & 1 & 0 \\ 0 & 0 & 0 \end{bmatrix} \qquad \text{and} \qquad \boldsymbol{A}_{K\delta \dot{\mathrm{r}}} \triangleq 2n_0 \begin{bmatrix} 0 & 1 & 0 \\ -1 & 0 & 0 \\ 0 & 0 & 0 \end{bmatrix}.$$

The new approximation for the inertial differential acceleration is derived from the difference in the two-body gravity gradient, written as

$$\boldsymbol{\nabla} F_{J0} = \mu \begin{bmatrix} \dfrac{(R_0 + x)}{\left[(R_0 + x)^2 + y^2 + z^2\right]^{3/2}} - \dfrac{1}{{R_0}^2} \\ \dfrac{y}{\left[(R_0 + x)^2 + y^2 + z^2\right]^{3/2}} \\ \dfrac{z}{\left[(R_0 + x)^2 + y^2 + z^2\right]^{3/2}} \end{bmatrix},$$

where R_0 is the orbital radius of the inspector spacecraft at t_0. Performing a Taylor series expansion about the inspector position (taken to be the origin of the Hill frame) and retaining only first- and second-order terms yields [18]

$$\boldsymbol{\nabla} F_{J0} \approx \boldsymbol{a}_{J0} = \boldsymbol{A}_{J0} \delta \mathbf{r} + \boldsymbol{A}_{J0}^{(2,\delta \mathrm{r})} \delta \mathbf{r}^{(2)}, \tag{2.10}$$

where

$$\boldsymbol{A}_{J0} \triangleq n_0^2 \begin{bmatrix} 2 & 0 & 0 \\ 0 & -1 & 0 \\ 0 & 0 & -1 \end{bmatrix} \qquad \text{and}$$

$$\boldsymbol{A}_{J0}^{(2,\delta \mathrm{r})} \triangleq \frac{3}{2}\frac{n_0^2}{R_0} \begin{bmatrix} -2 & 0 & 0 & 0 & 1 & 0 & 0 & 0 & 1 \\ 0 & 1 & 0 & 1 & 0 & 0 & 0 & 0 & 0 \\ 0 & 0 & 1 & 0 & 0 & 0 & 1 & 0 & 0 \end{bmatrix}.$$

The vector $\delta\mathbf{r}^{(2)}$ is the Kronecker product $\delta\mathbf{r} \otimes \delta\mathbf{r}$, which when applied between two column vectors is defined as

$$\mathbf{a} \otimes \mathbf{b} \triangleq \left[\mathrm{a}_1\mathbf{b}^T, \ldots, \mathrm{a}_m\mathbf{b}^T\right]^T,$$

where $\mathbf{a}$ is $m \times 1$. In other words,

$$\delta\mathbf{r}^{(2)} \triangleq \delta\mathbf{r} \otimes \delta\mathbf{r} = \left[x^2,\, xy,\, xz,\, yx,\, y^2,\, yz,\, zx,\, zy,\, z^2\right]^T. \tag{2.11}$$

Note that in Equation (2.11), $\delta\mathbf{r}^{(2)}$ contains three redundant monomials, namely xy, xz, and yz. Substituting Equations (2.9) and (2.10) into Equation (2.8) yields

$$\delta\ddot{\mathbf{r}} = \begin{bmatrix} \boldsymbol{A}_{K\delta\mathrm{r}} & \boldsymbol{A}_{K\delta\dot{\mathrm{r}}} \end{bmatrix} \begin{bmatrix} \delta\mathbf{r} \\ \\ \delta\dot{\mathbf{r}} \end{bmatrix} + \boldsymbol{A}_{J0}\delta\mathbf{r} + \boldsymbol{A}_{J0}^{(2,\delta\mathrm{r})}\delta\mathbf{r}^{(2)}. \tag{2.12}$$

The intent is to express Equation (2.12) in state space form such that a state transition matrix may be computed; however, there is an inconsistency between the vector arguments on the right hand side. At this point in the derivation, Reference [18]

rewrites Equation (2.12) in state space form as

$$\dot{\boldsymbol{x}}^{\otimes} = \bar{\boldsymbol{A}}\boldsymbol{x}^{\otimes}\,, \tag{2.13}$$

where $\boldsymbol{x}^{\otimes}$ is defined as

$$\boldsymbol{x}^{\otimes} \triangleq \left[\boldsymbol{x}^T,\, (\boldsymbol{x}\otimes\boldsymbol{x})^T\right]^T \qquad \text{and} \qquad \boldsymbol{x} \triangleq \left[\delta\mathbf{r}^T,\, \delta\dot{\mathbf{r}}^T\right]^T. \tag{2.14}$$

In other words,

$$\boldsymbol{x}^{\otimes} = \left[x,\, y,\, z,\, \dot{x},\, \dot{y},\, \dot{z},\, x^2,\, \ldots,\, x\dot{z},\, \ldots,\, \dot{z}x,\, \ldots,\, \dot{z}^2\right]^T.$$

Using the definition of Reference [18], $\boldsymbol{x}^{\otimes}$ is 42×1 and, similar to Equation (2.11), contains multiple redundant monomials, such as xy, xz, $x\dot{x}$, and so on. The inclusion of these redundant terms results in 42×42 system matrix $\bar{\boldsymbol{A}}$, which due to its size makes the analytical computation of the state transition matrix truly cumbersome.

Instead, the redundant monomials can be eliminated by defining

$$\bar{\boldsymbol{x}} = \left[x,\, y,\, z,\, \dot{x},\, \dot{y},\, \dot{z},\, x^2,\, \ldots,\, x\dot{z},\, y^2,\, \ldots,\, y\dot{z},\, z^2,\, \ldots,\, z\dot{z},\, \dot{x}^2,\, \ldots,\, \dot{x}\dot{z},\, \dot{y}^2,\, \dot{y}\dot{z},\, \dot{z}^2\right]^T,$$

which yields

$$\dot{\bar{\boldsymbol{x}}} = \bar{\boldsymbol{A}}\bar{\boldsymbol{x}}\,, \tag{2.15}$$

where the reduced 27×27 system matrix $\bar{\boldsymbol{A}}$ is given in Appendix 7.

The system defined by Equation (2.15) can be written in state transition matrix form as $\bar{\boldsymbol{x}}_k = \boldsymbol{\Phi}_{k-1}\bar{\boldsymbol{x}}_{k-1}$, where the state transition matrix $\boldsymbol{\Phi}_{k-1}(t)$ is found by

computing the inverse Laplace transform of the resolvent matrix, which is

$$\boldsymbol{\Phi}_{k-1}(s) = (s\boldsymbol{I} - \bar{\boldsymbol{A}})^{-1},$$

From the state transition matrix $\boldsymbol{\Phi}_{k-1}(t) = \mathcal{L}^{-1}\{\boldsymbol{\Phi}_{k-1}(s)\}$, the first three rows correspond to the time-varying relative position coordinates, which when expanded are

$$\begin{aligned}
x(t) = {} & \left[4 - 3C_\psi\right] x_0 + \left[\eta R_0 S_\psi\right] \dot{x}_0 + \left[2\eta R_0 \left(1 - C_\psi\right)\right] \dot{y}_0 \\
& + \left[\frac{3}{2}\eta n_0 \left(7 - 10C_\psi + 3C_{2\psi} + 12\psi S_\psi - 12\psi^2\right)\right] x_0^2 \\
& + \left[\frac{3}{2}\eta n_0 \left(1 - C_\psi\right)\right] y_0^2 + \left[\frac{1}{4}\eta n_0 \left(3 - 2C_\psi - C_{2\psi}\right)\right] z_0^2 \\
& + \left[\frac{1}{2}\eta^2 R_0 \left(-3 + 4C_\psi - C_{2\psi}\right)\right] \dot{x}_0^2 \\
& + \left[\frac{1}{2}\eta^2 R_0 \left(6 - 10C_\psi + 4C_{2\psi} + 12\psi S_\psi - 9\psi^2\right)\right] \dot{y}_0^2 \\
& + \left[\frac{1}{4}\eta^2 R_0 \left(3 - 4C_\psi + C_{2\psi}\right)\right] \dot{z}_0^2 \\
& + \left[6\eta n_0 \left(-S_\psi + \psi\right)\right] x_0 y_0 + \left[3\eta \left(4S_\psi - S_{2\psi} - 4\psi + 2\psi C_\psi\right)\right] x_0 \dot{x}_0 \\
& + \left[3\eta \left(4 - 6C_\psi + 2C_{2\psi} + 7\psi S_\psi - 6\psi^2\right)\right] x_0 \dot{y}_0 \\
& + \left[3\eta \left(-S_\psi + \psi\right)\right] y_0 \dot{y}_0 + \left[\frac{1}{2}\eta \left(2S_\psi - S_{2\psi}\right)\right] z_0 \dot{z}_0 \\
& + \left[\eta^2 R_0 \left(7S_\psi - 2S_{2\psi} - 6\psi + 3\psi C_\psi\right)\right] \dot{x}_0 \dot{y}_0
\end{aligned} \tag{2.16a}$$

$$
\begin{aligned}
y(t) = {} & \left[6\left(S_\psi - \psi\right)\right] x_0 + y_0 + \left[2\eta R_0\left(-1 + C_\psi\right)\right] \dot{x}_0 + \left[\eta R_0\left(4S_\psi - 3\psi\right)\right] \dot{y}_0 \\
& + \left[\frac{3}{4}\eta n_0\left(40S_\psi + 3S_{2\psi} - 22\psi - 24\psi C_\psi\right)\right] x_0^2 + \left[3\eta n_0\left(S_\psi - \psi\right)\right] y_0^2 \\
& + \left[\frac{1}{4}\eta n_0\left(4S_\psi + S_{2\psi} - 6\psi\right)\right] z_0^2 + \left[\frac{1}{4}\eta^2 R_0\left(8S_\psi - S_{2\psi} - 6\psi\right)\right] \dot{x}_0^2 \\
& + \left[\eta^2 R_0\left(10S_\psi + S_{2\psi} - 6\psi - 6\psi C_\psi\right)\right] \dot{y}_0^2 \\
& + \left[\frac{1}{4}\eta^2 R_0\left(8S_\psi - S_{2\psi} - 6\psi\right)\right] \dot{z}_0^2 + \left[3\eta n_0\left(1 - C_\psi\right)\right] x_0 y_0 \\
& + \left[\frac{3}{2}\eta\left(-5 + 4C_\psi + C_{2\psi} + 4\psi S_\psi\right)\right] x_0 \dot{x}_0 \\
& + \left[3\eta\left(12S_\psi + S_{2\psi} - 7\psi - 7\psi C_\psi\right)\right] x_0 \dot{y}_0 \\
& + \left[3\eta\left(-S_\psi + \psi\right)\right] y_0 \dot{x}_0 + \left[\frac{1}{2}\eta\left(-3 + 4C_\psi - C_{2\psi}\right)\right] z_0 \dot{z}_0 \\
& + \left[\eta^2 R_0\left(-3 + 2C_\psi + C_{2\psi} + 3\psi S_\psi\right)\right] \dot{x}_0 \dot{y}_0
\end{aligned} \tag{2.16b}
$$

$$
\begin{aligned}
z(t) = {} & \left[C_\psi\right] z_0 + \left[\eta R_0 S_\psi\right] \dot{z}_0 \\
& + \left[\frac{3}{2}\eta n_0\left(-3 + 2C_\psi + C_{2\psi} + 4\psi S_\psi\right)\right] x_0 z_0 \\
& + \left[\frac{3}{2}\eta\left(2S_\psi + S_{2\psi} - 4\psi C_\psi\right)\right] x_0 \dot{z}_0 \\
& + \left[\frac{1}{2}\eta\left(2S_\psi - S_{2\psi}\right)\right] z_0 \dot{x}_0 \\
& + \left[\eta\left(-3 + 2C_\psi + C_{2\psi} + 3\psi S_\psi\right)\right] z_0 \dot{y}_0 \\
& + \left[\frac{1}{2}\eta^2 R_0\left(3 - 4C_\psi + C_{2\psi}\right)\right] \dot{x}_0 \dot{z}_0 \\
& + \left[\eta^2 R_0\left(S_\psi + S_{2\psi} - 3\psi C_\psi\right)\right] \dot{y}_0 \dot{z}_0
\end{aligned} \tag{2.16c}
$$

where

$$
\psi \triangleq n_0(t - t_0)\,, \qquad \eta \triangleq \frac{1}{n_0 R_0}\,, \qquad C_{2\psi} \triangleq \cos(2\psi)\,, \quad \text{and} \quad S_{2\psi} \triangleq \sin(2\psi)\,.
$$

Equations (2.16) are referred to as the CW2 equations throughout the remainder of this thesis, as they capture second-order effects not included in the original

linear CW equations. In fact, setting the second-order terms (x_0^2, $x_0 y_0$, etc.) equal to zero produces the original linear CW solution. Reference [18] demonstrates that the CW2 equations more closely approximate the nonlinear two-body equations than the traditional CW equations, particularly when propagating over several orbits. For larger scale relative orbits (separations of kilometers for low Earth orbits), the CW2 equations' nonlinear terms can, in fact, dominate the along-track drift of the target satellite.

3. THE RELATIVE LAMBERT PROBLEM

In a well-known theorem of orbital mechanics, the unique conic (and thus velocity) of an orbiting body can be computed given two unique times and position vectors; this is the familiar Lambert problem [30–32]. Similarly, with relative dynamics, the relative velocity of a nearby spacecraft can be computed given its relative position vectors $\delta\mathbf{r}_0$ and $\delta\mathbf{r}_f$ at times t_0 and t_f, as illustrated in Figure 3.1.

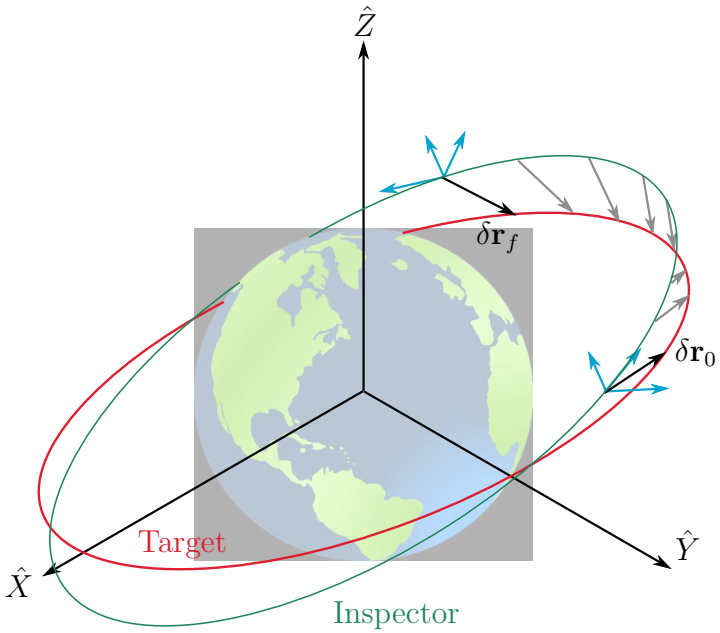

Figure 3.1. Relative motion of target spacecraft over time. Given two relative positions $\delta\mathbf{r}_0$ and $\delta\mathbf{r}_f$ and the time of flight $t_f - t_0$, the relative velocity can be solved, thus fully defining the relative orbit.

In this chapter, a brief review of the relative Lambert problem using the CW model is given, after which the CW2 relative Lambert problem is formulated and solved using Macaulay resultant expressions. Finally, a comparison of the CW solver, CW2 solver, and a classical Lambert-based solver is performed in a Monte Carlo

simulation, and the results are analyzed. Preliminary results are published in Reference [33]. The current work is a more comprehensive study with stronger results.

3.1. CW RELATIVE LAMBERT SOLUTION

The relative position and velocity are expressed in Cartesian coordinates in the rotating Hill frame as

$$\delta\mathbf{r} = [x,\, y,\, z]^T \qquad \text{and} \qquad \delta\dot{\mathbf{r}} = [\dot{x},\, \dot{y},\, \dot{z}]^T \,.$$

Defining the relative state vector to be $\boldsymbol{x}_k = [\delta\mathbf{r}_k^T,\, \delta\dot{\mathbf{r}}_k^T]^T$, Equations (2.7) may be written in terms of a state transition matrix as

$$\boldsymbol{x}_k = \boldsymbol{F}_{k-1}\boldsymbol{x}_{k-1} \,, \tag{3.1}$$

where the state transition matrix is

$$\boldsymbol{F}_{k-1} = \begin{bmatrix} \boldsymbol{\Phi}_{\text{rr}} & \boldsymbol{\Phi}_{\text{rv}} \\ \boldsymbol{\Phi}_{\text{vr}} & \boldsymbol{\Phi}_{\text{vv}} \end{bmatrix} \,, \tag{3.2}$$

with

$$\boldsymbol{\Phi}_{\text{rr}} = \begin{bmatrix} 4-3C_\psi & 0 & 0 \\ 6(S_\psi - \psi) & 1 & 0 \\ 0 & 0 & C_\psi \end{bmatrix} \,, \qquad \boldsymbol{\Phi}_{\text{rv}} = \begin{bmatrix} \frac{1}{n_0}S_\psi & \frac{2}{n_0}(1-C_\psi) & 0 \\ \frac{2}{n_0}(C_\psi - 1) & \frac{4}{n_0}S_\psi - \frac{3}{n_0}\psi & 0 \\ 0 & 0 & \frac{1}{n_0}S_\psi \end{bmatrix} \,,$$

$$\boldsymbol{\Phi}_{\text{vr}} = \begin{bmatrix} 3n_0 S_\psi & 0 & 0 \\ 6n_0(C_\psi - 1) & 0 & 0 \\ 0 & 0 & -n_0 S_\psi \end{bmatrix} \,, \quad \boldsymbol{\Phi}_{\text{vv}} = \begin{bmatrix} C_\psi & 2S_\psi & 0 \\ -2S_\psi & -3+4C_\psi & 0 \\ 0 & 0 & C_\psi \end{bmatrix} \,.$$

Using the CW model, if $\delta\mathbf{r}_0$, $\delta\mathbf{r}_f$, and the time of flight $(t_f - t_0)$ are known, it follows that

$$\delta\dot{\mathbf{r}}_0 = \mathbf{\Phi}_{\mathrm{rv}}^{-1}(\delta\mathbf{r}_f - \mathbf{\Phi}_{\mathrm{rr}}\delta\mathbf{r}_0)\,. \tag{3.3}$$

Note that the inverse $\mathbf{\Phi}_{\mathrm{rv}}^{-1}$ exists for all $n_0(t_f - t_0) = \psi \neq m\pi$, where $m = \{0, 1, 2, \ldots\}$. This phenomenon is due to the decoupled, periodic nature of the cross track motion (Eq. (2.7c)), as illustrated in Figure 3.2. Repeating Equation (2.7c) for convenience,

$$z(t) = z_0 \cos(\psi) + \frac{\dot{z}_0}{n_0}\sin(\psi)$$

it is straightforward to see that when $\psi = m\pi$, the z position is independent of the initial cross track velocity $\dot{z}_0$.

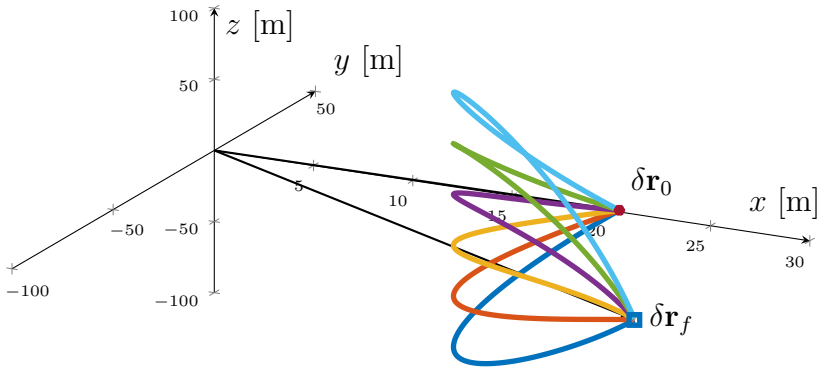

Figure 3.2. Due to the decoupled, periodic nature of the cross-track motion, an infinite number of relative velocities satisfy the relative Lambert problem for times of flight that are integer multiples of the orbital half period.

3.2. CW2 RELATIVE LAMBERT SOLUTION

The relative Lambert solution for the CW model is very simple due to the linear nature of the dynamics. In contrast, due to the nonlinear nature of the CW2 model, a relative velocity solution cannot be obtained in the same algebraic fashion as Equation (3.3). However, if the relative positions at t_0 and t_f are known, Equations (2.16) can be formulated as a multivariate root finding problem; that is, the problem becomes to find the relative velocity $\delta\dot{\mathbf{r}}_0 = [\dot{x}_0,\, \dot{y}_0,\, \dot{z}_0]^T$ that satisfies

$$x(\dot{x}_0,\, \dot{y}_0,\, \dot{z}_0) - x_f = 0\,, \tag{3.4a}$$

$$y(\dot{x}_0,\, \dot{y}_0,\, \dot{z}_0) - y_f = 0\,, \tag{3.4b}$$

$$\text{and} \quad z(\dot{x}_0,\, \dot{y}_0,\, \dot{z}_0) - z_f = 0\,. \tag{3.4c}$$

Equations (3.4) are simply the rewriting of Equations (2.16) with functional dependence on $\dot{x}_0$, $\dot{y}_0$, and $\dot{z}_0$ rather than the known t_f (note that $x_f = x(t_f)$, and so on). Equations (3.4) can be written as a set of multivariate polynomials in standard polynomial form as

$$f_1(\dot{x}_0, \dot{y}_0, \dot{z}_0) = a_1\dot{x}_0^2 \quad + a_2\dot{x}_0\dot{y}_0 + a_3\dot{x}_0 \quad + a_4\dot{y}_0^2 + a_5\dot{y}_0 + a_6\dot{z}_0^2 + a_7\dot{z}_0 + a_8 = 0 \tag{3.5a}$$

$$f_2(\dot{x}_0, \dot{y}_0, \dot{z}_0) = b_1\dot{x}_0^2 \quad + b_2\dot{x}_0\dot{y}_0 + b_3\dot{x}_0 \quad + b_4\dot{y}_0^2 + b_5\dot{y}_0 + b_6\dot{z}_0^2 + b_7\dot{z}_0 + b_8 = 0 \tag{3.5b}$$

$$f_3(\dot{x}_0, \dot{y}_0, \dot{z}_0) = c_1\dot{x}_0\dot{z}_0 + c_2\dot{x}_0 \quad + c_3\dot{y}_0\dot{z}_0 + c_4\dot{y}_0 + c_5\dot{z}_0 + c_6 \qquad = 0 \tag{3.5c}$$

where, from Equations (2.16), the coefficients in Equations (3.5) are given by

$$
\begin{aligned}
a_1 =& \frac{1}{2}\eta^2 R_0 \left(-3 + 4C_\psi - C_{2\psi}\right) \\
a_2 =& \eta^2 R_0 \left(7S_\psi - 2S_{2\psi} - 6\psi + 3\psi C_\psi\right) \\
a_3 =& \eta R_0 S_\psi + \left[3\eta \left(4S_\psi - S_{2\psi} - 4\psi + 2\psi C_\psi\right)\right] x_0 \\
a_4 =& \frac{1}{2}\eta^2 R_0 \left(6 - 10C_\psi + 4C_{2\psi} + 12\psi S_\psi - 9\psi^2\right) \\
a_5 =& 2\eta R_0 \left(1 - C_\psi\right) + \left[3\eta \left(4 - 6C_\psi + 2C_{2\psi} + 7\psi S_\psi - 6\psi^2\right)\right] x_0 + \left[3\eta \left(-S_\psi + \psi\right)\right] y_0 \\
a_6 =& \frac{1}{4}\eta^2 R_0 \left(3 - 4C_\psi + C_{2\psi}\right) \\
a_7 =& \left[\frac{1}{2}\eta \left(2S_\psi - S_{2\psi}\right)\right] z_0 \\
a_8 =& \left[4 - 3C_\psi\right] x_0 + \left[\frac{3}{2}\eta n_0 \left(7 - 10C_\psi + 3C_{2\psi} + 12\psi S_\psi - 12\psi^2\right)\right] x_0^2 \\
&+ \left[\frac{3}{2}\eta n_0 \left(1 - C_\psi\right)\right] y_0^2 + \left[\frac{1}{4}\eta n_0 \left(3 - 2C_\psi - C_{2\psi}\right)\right] z_0^2 \\
&+ \left[6\eta n_0 \left(-S_\psi + \psi\right)\right] x_0 y_0 - x_f \\
b_1 =& \frac{1}{4}\eta^2 R_0 \left(8S_\psi - S_{2\psi} - 6\psi\right) \\
b_2 =& \eta^2 R_0 \left(-3 + 2C_\psi + C_{2\psi} + 3\psi S_\psi\right) \\
b_3 =& 2\eta R_0 \left(-1 + C_\psi\right) + \left[\frac{3}{2}\eta \left(-5 + 4C_\psi + C_{2\psi} + 4\psi S_\psi\right)\right] x_0 + \left[3\eta \left(-S_\psi + \psi\right)\right] y_0 \\
b_4 =& \eta^2 R_0 \left(10S_\psi + S_{2\psi} - 6\psi - 6\psi C_\psi\right) \\
b_5 =& \eta R_0 \left(4S_\psi - 3\psi\right) + \left[3\eta \left(12S_\psi + S_{2\psi} - 7\psi - 7\psi C_\psi\right)\right] x_0 \\
b_6 =& \frac{1}{4}\eta^2 R_0 \left(8S_\psi - S_{2\psi} - 6\psi\right) \\
b_7 =& \left[\frac{1}{2}\eta \left(-3 + 4C_\psi - C_{2\psi}\right)\right] z_0 \\
b_8 =& \left[6\left(S_\psi - \psi\right)\right] x_0 + y_0 + \left[\frac{3}{4}\eta n_0 \left(40S_\psi + 3S_{2\psi} - 22\psi - 24\psi C_\psi\right)\right] x_0^2 \\
&+ \left[3\eta n_0 \left(S_\psi - \psi\right)\right] y_0^2 + \left[\frac{1}{4}\eta n_0 \left(4S_\psi + S_{2\psi} - 6\psi\right)\right] z_0^2 + \left[3\eta n_0 \left(1 - C_\psi\right)\right] x_0 y_0 - y_f
\end{aligned}
$$

$$
\begin{aligned}
c_1 &= \left[\frac{1}{2}\eta^2 R_0 \left(3 - 4C_\psi + C_{2\psi}\right)\right] \\
c_2 &= \left[\frac{1}{2}\eta \left(2S_\psi - S_{2\psi}\right)\right] z_0 \\
c_3 &= \left[\eta^2 R_0 \left(S_\psi + S_{2\psi} - 3\psi C_\psi\right)\right] \\
c_4 &= \left[\eta \left(-3 + 2C_\psi + C_{2\psi} + 3\psi S_\psi\right)\right] z_0 \\
c_5 &= \left[\eta R_0 S_\psi\right] + \left[\frac{3}{2}\eta \left(2S_\psi + S_{2\psi} - 4\psi C_\psi\right)\right] x_0 \\
c_6 &= \left[C_\psi\right] z_0 + \left[\frac{3}{2}\eta n_0 \left(-3 + 2C_\psi + C_{2\psi} + 4\psi S_\psi\right)\right] x_0 z_0 - z_f
\end{aligned} \tag{3.6}
$$

Note that the final relative position coordinates x_f, y_f and z_f are contained within the coefficients a_8, b_8, and c_6, respectively.

For simplicity and generality, the independent variables $\dot{x}_0$, $\dot{y}_0$, and $\dot{z}_0$ are represented by x_1, x_2, and x_3 throughout the remainder of this chapter and should not be confused with the time-varying relative position coordinates. In the new notation, Equations (3.5) are expressed as

$$f_1(x_1, x_2, x_3) = a_1 x_1^2 + a_2 x_1 x_2 + a_3 x_1 + a_4 x_2^2 + a_5 x_2 + a_6 x_3^2 + a_7 x_3 + a_8 = 0 \tag{3.7a}$$

$$f_2(x_1, x_2, x_3) = b_1 x_1^2 + b_2 x_1 x_2 + b_3 x_1 + b_4 x_2^2 + b_5 x_2 + b_6 x_3^2 + b_7 x_3 + b_8 = 0 \tag{3.7b}$$

$$f_3(x_1, x_2, x_3) = c_1 x_1 x_3 + c_2 x_1 + c_3 x_2 x_3 + c_4 x_2 + c_5 x_3 + c_6 = 0 \tag{3.7c}$$

Equations (3.7) can be represented geometrically as three intersecting quadrics, as shown for a particular set of coefficients in Figure 3.3. By Bezout's theorem, three quadric surfaces can intersect at infinitely many points or, at most, eight unique points [34].

3.2.1. Macaulay Resultant Expressions. In order to find all of the possible relative trajectories that pass through the relative positions $\delta\mathbf{r}_0$ and $\delta\mathbf{r}_f$ at times t_0 and t_f, the set of relative velocity components that satisfy the set of polynomials given in Equations (3.5) must be computed. All of the possible solutions can be found

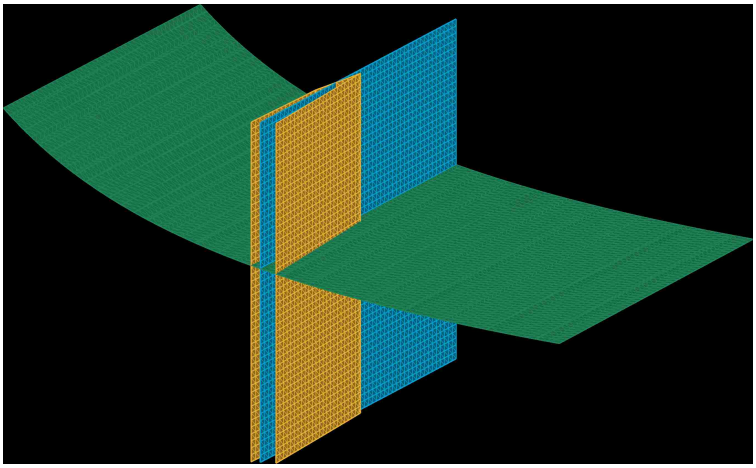

Figure 3.3. Geometric representation of f_1, f_2 and f_3 polynomial surfaces. The points at which all three surfaces intersect represent the velocity solutions to the CW2 relative Lambert problem.

non-iteratively[1] via the application of Macaulay resultants. For instance, consider a general system of n polynomial equations in n unknowns given by

$$\begin{aligned} f_1(x_1, x_2, ..., x_n) &= 0 \\ f_2(x_1, x_2, ..., x_n) &= 0 \\ &\vdots \\ f_n(x_1, x_2, ..., x_n) &= 0 \end{aligned} \tag{3.8}$$

with degrees d_1, d_2, ..., d_n, respectively. A polynomial's degree is equal to the degree of its highest-degree monomial. For example, the polynomial

$$f(x_1, x_2) = x_1^2 x_2^2 + x_2^3$$

is degree-four because the combined powers of monomial $x_1^2 x_2^2$ is four.

[1]Here, "non-iteratively" means that solutions are not computed and corrected iteratively as is common in other numerical root-finding methods. However, the solution process, as is demonstrated later, involves an intermediate eigenvalue problem, which is most readily solved by an iterative method.

Multipolynomial resultants can be used to eliminate the variables

$$x_2,\, x_3,\, \ldots,\, x_n$$

from Equations (3.8) by projecting the algebraic set into a lower dimension [35]. In other words, a new univariate polynomial may be formed, and its roots correspond to the roots of the original multivariate system. Furthermore, this univariate polynomial, formally known as the resultant, is systematically constructed using the coefficients of the original polynomials. Nearly all methods of computing resultants represent the resultant in terms of matrices and determinants. One of these formulations, known as the Macaulay resultant, expresses $R(x_1)$, that is the resultant obtained by eliminating $x_2,\, \ldots,\, x_n$ from the equations, as a ratio of determinants of two matrices $\boldsymbol{M}$ and $\boldsymbol{D}$ as [36]

$$R\left(x_1\right) = \frac{\det\left(\boldsymbol{M}\right)}{\det\left(\boldsymbol{D}\right)}\,. \tag{3.9}$$

The entries of $\boldsymbol{M}$ and $\boldsymbol{D}$ are polynomials in x_1, and if $\boldsymbol{D}$ is nonsingular, the roots of the polynomial $\det\left(\boldsymbol{M}\right)$ correspond exactly to the roots of x_1 in the original system [37]. For most applications, it is impractical to compute the determinant of $\boldsymbol{M}$. Fortunately, the roots of the polynomial set can be found while avoiding this calculation. Reference [35] shows how resultant expressions can be expressed as matrix polynomials, in which the root-finding problem reduces to an eigenvalue problem. Nonetheless, in the examples that follow, the determinant of $\boldsymbol{M}$ is computed and shown for illustrative purposes.

Herein, a unique method for constructing multipolynomial resultants for the common problem of n polynomial equations with n unknowns is presented. Given the multivariate polynomials $f_1,\, f_2,\, \ldots,\, f_n$, the resultant transforms the nonlinear system

of Equations (3.8) into a linear system as given in Equation (3.10) such that [35]

$$\boldsymbol{M}(x_1)\left[1,\, x_2,\, \ldots,\, x_n,\, \ldots,\, x_2^d,\, x_3^d,\, \ldots,\, x_n^d\right]^T = \begin{bmatrix} 0 \\ 0 \\ \vdots \\ 0 \end{bmatrix}. \tag{3.10}$$

Note that in Equation (3.10), the organization of the power products varies depending on the choice of the variable projection and the structure of the polynomials themselves.

If $f_1,\, f_2, \ldots,\, f_n$ simultaneously vanish at some point in the projective space, then the kernel of $\boldsymbol{M}(x_1)$ contains some nontrivial vector [38]. Recall that a resultant is simply a polynomial in the coefficients of the original system. Therefore, as shown in Equation (3.10), if x_1 is known, the remaining roots $x_2,\, x_3,\, \ldots,\, x_n$ simply correspond to the kernel of $\boldsymbol{M}(x_1)$. With this, the root finding process consists of three main steps: 1) constructing $\boldsymbol{M}$, 2) computing x_1, and 3) solving for the remaining coordinates' roots. The matrix $\boldsymbol{M}$ is constructed using the coefficients of the original set of polynomials. Once $\boldsymbol{M}$ is formed, it is expanded into a matrix polynomial. The matrix polynomial's coefficient matrices are used in a generalized eigenvalue problem to compute all of the possible roots in x_1. Once x_1 is found, the remaining roots are found by computing the kernel of $\boldsymbol{M}(x_1)$. This entire process, including the construction of $\boldsymbol{M}$, the formation of the matrix polynomial, the computation of x_1 using eigendecomposition, and the computation of the remaining coordinates' roots is discussed in greater detail in the following sections.

3.2.2. Solution of Relative Lambert Problem Using Resultants. In order to compute the initial relative velocity $\delta\dot{\mathbf{r}}_0$, the roots of the multivariate, inhomogeneous, nonlinear set of polynomials given in Equations (3.7) must be found. These roots can be computed systematically through the use of Macaulay resultant

expressions. Recall that the resultant can be expressed as the ratio of two determinants (Eq. 3.9). The entries of $\boldsymbol{M}$ and $\boldsymbol{D}$ are polynomials in x_1, and if $\boldsymbol{D}$ is nonsingular, the roots of the polynomial $\det(\boldsymbol{M})$ correspond exactly to the roots of x_1 in the original system [37]. Once the numerator matrix $\boldsymbol{M}$ is constructed, it can be written as a matrix polynomial in x_1, and the solution(s) $\alpha_1 = x_1$ can be computed using a simple eigendecomposition. Once a solution set α_1 is computed, the remaining coordinate solution sets, α_2, α_3, $\ldots$, α_n can be computed using the relation shown in Equation (3.10).

Because the intent is to express $\boldsymbol{M}$ as a univariate matrix polynomial, one variable is chosen to be the sole functional dependence of $\boldsymbol{M}$. This same variable is then treated as constant in the original polynomial set and is absorbed into the coefficients. Rewriting Equations (3.7) and absorbing x_3 into the coefficients,

$$f_1(x_1, x_2) = A_1 x_1^2 + A_2 x_1 x_2 + A_3 x_1 + A_4 x_2^2 + A_5 x_2 + A_6 = 0 \tag{3.11a}$$

$$f_2(x_1, x_2) = B_1 x_1^2 + B_2 x_1 x_2 + B_3 x_1 + B_4 x_2^2 + B_5 x_2 + B_6 = 0 \tag{3.11b}$$

$$f_3(x_1, x_2) = C_1 x_1 + C_2 x_2 \quad + C_3 \qquad\qquad = 0 \tag{3.11c}$$

where

$$\begin{aligned}
A_1 &= a_1 & A_2 &= a_2 & A_3 &= a_3 \\
A_4 &= a_4 & A_5 &= a_5 & A_6 &= a_6 x_3^2 + a_7 x_3 + a_8 \\
B_1 &= b_1 & B_2 &= b_2 & B_3 &= b_3 \\
B_4 &= b_4 & B_5 &= b_5 & B_6 &= b_6 x_3^2 + b_7 x_3 + b_8 \\
C_1 &= c_1 x_3 + c_2 & C_2 &= c_3 x_3 + c_4 & C_3 &= c_5 x_3 + c_6
\end{aligned}$$

Note that Equations (3.11) could be written in three ways by choosing to absorb either x_1, x_2, or x_3. However, the choice of x_3 results in a lower polynomial degree (degree-

one) of Equation (3.11c), and greatly simplifies the resultant expression. For example, the selection of x_1 results in a polynomial $f_3(x_2, x_3)$ that contains the monomial x_2x_3 and is, therefore, degree-two.

3.2.2.1. Homogenization. Equations (3.11) are inhomogeneous, meaning that the monomials of each polynomial do not all have equal degree. For example, the first two monomials of Equation (3.11a), x_1^2 and x_1x_2, are of degree-two, whereas the following monomial x_1 is degree-one. In order to form the resultant expression, the polynomials must first be homogenized. To homogenize, an extra variable w is added to even the monomial degrees:

$$f_1(x_1, x_2, w) = A_1x_1^2 + A_2x_1x_2 + A_3x_1w + A_4x_2^2 + A_5x_2w + A_6w^2 = 0 \qquad (3.12a)$$

$$f_2(x_1, x_2, w) = B_1x_1^2 + B_2x_1x_2 + B_3x_1w + B_4x_2^2 + B_5x_2w + B_6w^2 = 0 \qquad (3.12b)$$

$$f_3(x_1, x_2, w) = C_1x_1 + C_2x_2 \quad + C_3w \qquad = 0 \qquad (3.12c)$$

To maintain the equivalency of the polynomials after homogenization, the specialization of variables is chosen such that $w = 1$. This specialization is important in the later steps of the algorithm.

3.2.2.2. Matrix size. To construct the resultant matrix $\boldsymbol{M}$ for the system of polynomials $f_1,\ f_2, \ldots,\ f_n$, the total degree of the system must be determined. The total degree, d of a given set of polynomials is computed as

$$d = 1 + \sum_{i=1}^{m} (d_i - 1) \ ,$$

where m is the number of equations and d_i is the degree of the i^{th} equation. From this, the size of $\boldsymbol{M}$ can be computed as

$$\text{size}(\boldsymbol{M}) = \begin{pmatrix} n+d \\ n \end{pmatrix} \ ,$$

where n is the number of variables in the set *before* homogenization. Equations (3.12) are of degree $d_1 = 2$, $d_2 = 2$, and $d_3 = 1$. The resulting total degree is computed as

$$d = 1 + (2 - 1) + (2 - 1) + (1 - 1) = 3\,.$$

With this, the size of the square numerator matrix is computed as

$$\text{size}(\boldsymbol{M}) = \begin{pmatrix} 2+3 \\ \\ 2 \end{pmatrix} = 10\,.$$

3.2.2.3. Construction of M. The numerator matrix $\boldsymbol{M}$ is constructed with entries that are polynomials in x_3. The columns of $\boldsymbol{M}$ correspond to all the possible monomials of degree d arranged in lexicographical order. Thus, the column labels of $\boldsymbol{M}$ are all of the degree-three monomials in x_1, x_2, and w, given as

$$\left\{x_1^3,\, x_1^2x_2,\, x_1^2w,\, x_1x_2^2,\, x_1x_2w,\, x_1w^2,\, x_2^3,\, x_2^2w,\, x_2w^2,\, w^3\right\}\,.$$

The row labels correspond to the homogeneous polynomials multiplied by the system variables, specifically,

$$\left\{x_1f_1,\, x_2f_1,\, wf_1,\, x_1f_2,\, x_1x_2f_3,\, x_1wf_3,\, x_2f_2,\, wf_2,\, x_2wf_3,\, w^2f_3\right\}\,.$$

With this, the application Equation (3.10) is written as

$$\boldsymbol{M}(x_3)\left[x_1^3,\, x_1^2x_2,\, x_1^2w,\, x_1x_2^2,\, x_1x_2w,\, x_1w^2,\, x_2^3,\, x_2^2w,\, x_2w^2,\, w^3\right]^T = \boldsymbol{0}\,. \tag{3.13}$$

For a more in-depth discussion on the construction of $\boldsymbol{M}$, including a set of explicit rules for the formation of row labels, the reader is directed to Reference [39]. The

resulting $\boldsymbol{M}$ matrix for the CW2 relative Lambert problem is

$$\boldsymbol{M}(x_3) = \begin{array}{c} \\ x_1 f_1 \\ x_2 f_1 \\ w f_1 \\ x_1 f_2 \\ x_1 x_2 f_3 \\ x_1 w f_3 \\ x_2 f_2 \\ w f_2 \\ x_2 w f_3 \\ w^2 f_3 \end{array} \begin{array}{c} \begin{array}{cccccccccc} x_1^3 & x_1^2 x_2 & x_1^2 w & x_1 x_2^2 & x_1 x_2 w & x_1 w^2 & x_2^3 & x_2^2 w & x_2 w^2 & w^3 \end{array} \\ \begin{bmatrix} A_1 & A_2 & A_3 & A_4 & A_5 & A_6 & \cdot & \cdot & \cdot & \cdot \\ \cdot & A_1 & \cdot & A_2 & A_3 & \cdot & A_4 & A_5 & A_6 & \cdot \\ \cdot & \cdot & A_1 & \cdot & A_2 & A_3 & \cdot & A_4 & A_5 & A_6 \\ B_1 & B_2 & B_3 & B_4 & B_5 & B_6 & \cdot & \cdot & \cdot & \cdot \\ \cdot & C_1 & \cdot & C_2 & C_3 & \cdot & \cdot & \cdot & \cdot & \cdot \\ \cdot & \cdot & C_1 & \cdot & C_2 & C_3 & \cdot & \cdot & \cdot & \cdot \\ \cdot & B_1 & \cdot & B_2 & B_3 & \cdot & B_4 & B_5 & B_6 & \cdot \\ \cdot & \cdot & B_1 & \cdot & B_2 & B_3 & \cdot & B_4 & B_5 & B_6 \\ \cdot & \cdot & \cdot & \cdot & C_1 & \cdot & \cdot & C_2 & C_3 & \cdot \\ \cdot & \cdot & \cdot & \cdot & \cdot & C_1 & \cdot & \cdot & C_2 & C_3 \end{bmatrix} \end{array} \tag{3.14}$$

where the dots correspond to entries that are zero, and the row/column labels are provided for reference.

3.2.2.4. Construction of D. In Macaulay's original formulation, the determinant of the denominator matrix $\boldsymbol{D}$ was formed to factor out extraneous factors in the resultant. However, if $\boldsymbol{D}$ is nonsingular, the roots of the determinant of $\boldsymbol{M}$ correspond to the roots of the original system exactly. If $\boldsymbol{D}$ is singular, $\boldsymbol{M}$ must be replaced with its largest non-vanishing minor [35]. Therefore, although the denominator is not directly used in the computation of the polynomial roots, it still must be constructed to check its singularity. For this problem, $\boldsymbol{D}$ is constructed as

$$\boldsymbol{D} = \begin{bmatrix} A_1 & A_4 \\ B_1 & B_4 \end{bmatrix}.$$

It can be shown that the determinant of $\boldsymbol{D}$ in this problem is only zero when $t = 0$. Note that $t = 0$ is a degenerate case of Equations (2.16), and can only result in

infinite velocities (when $\delta\mathbf{r}_0 \neq \delta\mathbf{r}_f$) or zero velocities (when $\delta\mathbf{r}_0 = \delta\mathbf{r}_f$). Again, a more detailed discussion on the construction of $\boldsymbol{D}$ can be found in Reference [39].

3.2.2.5. Matrix polynomial. Recalling that the A, B, and C coefficients are functions of x_3, the $\boldsymbol{M}$ matrix from Equation (3.14) can be expanded into a matrix polynomial expression as

$$\boldsymbol{M}(x_3) = \boldsymbol{M_0} + \boldsymbol{M_1} x_3 + \boldsymbol{M_2} x_3^2 \,, \tag{3.15}$$

where

$$\boldsymbol{M_0} = \begin{bmatrix} a_1 & a_2 & a_3 & a_4 & a_5 & a_8 & \cdot & \cdot & \cdot & \cdot \\ \cdot & a_1 & \cdot & a_2 & a_3 & \cdot & a_4 & a_5 & a_8 & \cdot \\ \cdot & \cdot & a_1 & \cdot & a_2 & a_3 & \cdot & a_4 & a_5 & a_8 \\ b_1 & b_2 & b_3 & b_4 & b_5 & b_8 & \cdot & \cdot & \cdot & \cdot \\ \cdot & c_2 & \cdot & c_4 & c_6 & \cdot & \cdot & \cdot & \cdot & \cdot \\ \cdot & \cdot & c_2 & \cdot & c_4 & c_6 & \cdot & \cdot & \cdot & \cdot \\ \cdot & b_1 & \cdot & b_2 & b_3 & \cdot & b_4 & b_5 & b_8 & \cdot \\ \cdot & \cdot & b_1 & \cdot & b_2 & b_3 & \cdot & b_4 & b_5 & b_8 \\ \cdot & \cdot & \cdot & \cdot & c_2 & \cdot & \cdot & c_4 & c_6 & \cdot \\ \cdot & \cdot & \cdot & \cdot & \cdot & c_2 & \cdot & \cdot & c_4 & c_6 \end{bmatrix} ,$$

$$\boldsymbol{M_1} = \begin{bmatrix} \cdot & \cdot & \cdot & \cdot & \cdot & a_7 & \cdot & \cdot & \cdot & \cdot \\ \cdot & \cdot & \cdot & \cdot & \cdot & \cdot & \cdot & \cdot & a_7 & \cdot \\ \cdot & \cdot & \cdot & \cdot & \cdot & \cdot & \cdot & \cdot & \cdot & a_7 \\ \cdot & \cdot & \cdot & \cdot & \cdot & b_7 & \cdot & \cdot & \cdot & \cdot \\ \cdot & c_1 & \cdot & c_3 & c_5 & \cdot & \cdot & \cdot & \cdot & \cdot \\ \cdot & \cdot & c_1 & \cdot & c_3 & c_5 & \cdot & \cdot & \cdot & \cdot \\ \cdot & \cdot & \cdot & \cdot & \cdot & \cdot & \cdot & \cdot & b_7 & \cdot \\ \cdot & \cdot & \cdot & \cdot & \cdot & \cdot & \cdot & \cdot & \cdot & b_7 \\ \cdot & \cdot & \cdot & \cdot & c_1 & \cdot & \cdot & c_3 & c_5 & \cdot \\ \cdot & \cdot & \cdot & \cdot & \cdot & c_1 & \cdot & \cdot & c_3 & c_5 \end{bmatrix}, \quad \boldsymbol{M_2} = \begin{bmatrix} & a_6 & \cdot & \cdot & \cdot & \cdot \\ & \cdot & \cdot & \cdot & a_6 & \cdot \\ & \cdot & \cdot & \cdot & \cdot & a_6 \\ & b_6 & \cdot & \cdot & \cdot & \cdot \\ \mathbf{0}_{10\times5} & \cdot & \cdot & \cdot & \cdot & \cdot \\ & \cdot & \cdot & \cdot & \cdot & \cdot \\ & \cdot & \cdot & \cdot & b_6 & \cdot \\ & \cdot & \cdot & \cdot & \cdot & b_6 \\ & \cdot & \cdot & \cdot & \cdot & \cdot \\ & \cdot & \cdot & \cdot & \cdot & \cdot \end{bmatrix} \tag{3.16}$$

Note that the elements of $\boldsymbol{M_0}$, $\boldsymbol{M_1}$, and $\boldsymbol{M_2}$ are simply the coefficients of the original polynomials (Eqs. 3.5) and are constant for some given initial position, final position, and elapsed time. Because Equation (3.15) is univariate, the roots of its determinant can be computed using eigendecomposition. Given the matrix polynomial, $\boldsymbol{M}(x_3)$, the roots of the resultant polynomial (given by the determinant of $\boldsymbol{M}$) are the eigenvalues of the generalized system [35]

$$\boldsymbol{A}x_3 = \boldsymbol{B}\,, \tag{3.17}$$

where

$$\boldsymbol{A} = \begin{bmatrix} \boldsymbol{I_m} & \mathbf{0} \\ \mathbf{0} & \boldsymbol{M_2} \end{bmatrix}, \quad \boldsymbol{B} = \begin{bmatrix} \mathbf{0} & \boldsymbol{I_m} \\ -\boldsymbol{M_0} & -\boldsymbol{M_1} \end{bmatrix},$$

and $\boldsymbol{I_m}$ is the identity matrix of size equal to that of $\boldsymbol{M}$.

Because x_3 corresponds to the z-component of velocity, only real and finite eigenvalues obtained from the solution of the generalized eigenvalue problem in Equa-

tion (3.17) are of interest. After discarding the infinite and imaginary eigenvalues, the remaining values α_3 correspond to the possible and valid solutions in x_3 (i.e. $\dot{z}_0$). For each valid simple eigenvalue $\alpha_3 = x_3$, the remaining states can be found by computing the kernel of $\boldsymbol{M}(\alpha_3)$; that is, computing the nontrivial vector $\mathbf{v}$ such that

$$\boldsymbol{M}(\alpha_3)\,\mathbf{v} = \mathbf{0} \tag{3.18}$$

Depending on the linear algebra routines used, the kernel vector $\mathbf{v}$ may be a scalar multiple of the solution [35]. In that case, the relationship of Equation (3.13) and the specialization of $w = 1$ can be used to back out the scale factor β:

$$\begin{pmatrix} x_1^3 & x_1^2x_2 & x_1^2 & x_1x_2^2 & x_1x_2 & x_1 & x_2^3 & x_2^2 & x_2 & 1 \end{pmatrix}^T = \beta \begin{pmatrix} v_1 & v_2 & \dots & v_{10} \end{pmatrix}^T \tag{3.19}$$

For this problem, $\beta = \dfrac{1}{v_{10}}$, so the remaining two velocity terms are computed as

$$\dot{x}_0 = \alpha_1 = \frac{v_6}{v_{10}} \qquad \text{and} \qquad \dot{y}_0 = \alpha_2 = \frac{v_9}{v_{10}} \tag{3.20}$$

Because the specialization of variables was chosen such that $w = 1$, α_1 and α_2 correspond to the sixth kernel element v_6 and ninth kernel element v_9, respectively, as is clearly shown in Equation (3.19). The computation of these coordinate solutions completes the CW2 relative Lambert solver algorithm, which is summarized in Algorithm 1.

Algorithm 1: CW2 Relative Lambert Solver

Given $\delta\mathbf{r}_0, \delta\mathbf{r}_f, t_f - t_0$, compute coefficients $a_1, \ldots, a_8, b_1, \ldots, b_8, c_1, \ldots, c_6$ (Eq. 3.6)

Construct $\boldsymbol{M_0}, \boldsymbol{M_1}, \boldsymbol{M_2}$ using coefficients computed in previous step. (Eq. 3.16)

Solve the generalized eigenvalue problem to find all possible $\dot{z}_0$ solutions. (Eq. 3.17)

for each valid $\dot{z}_0$ solution **do**

Compute the kernel, $\mathbf{v}$, of $\boldsymbol{M}(\dot{z}_0)$. (Eq. 3.18)

Compute $\dot{x}_0$ and $\dot{y}_0$ from $\mathbf{v}$. (Eq. 3.20)

end for

3.2.3. Numerical Example. Consider the following relative positions measured at $t_0 = 0$ and $t_f = 10,000$ [s], respectively:

$$\delta\mathbf{r}_0 = [1,\, -3,\, 15]^T \text{ [m]} \qquad \delta\mathbf{r}_f = [-1305.18,\, -3830.05,\, -3002.31]^T \text{ [m]}$$

The matrices $\boldsymbol{M_0}$, $\boldsymbol{M_1}$, and $\boldsymbol{M_2}$ are built to form $\boldsymbol{A}$ and $\boldsymbol{B}$. Using the $\boldsymbol{A}$ and $\boldsymbol{B}$ matrices, the solutions in $\dot{z}_0$ (or x_3) are computed through the generalized eigenvalue problem. Recall that the eigenvalues correspond exactly to the roots of the resultant, $R(\dot{z}_0)$, as shown in Figure 3.4.

As illustrated in Figure 3.4, there exist two possible initial relative (cross-track) velocities $\dot{z}_0 = 2.3197\,[\text{m/s}]$ and $\dot{z}_0 = 3.5000\,[\text{m/s}]$ that satisfy the initial conditions. Mathematically, the values $x_3 = 0.0023197$ and $x_3 = 0.0035000$ cause $\boldsymbol{M}(x_3)$ to be singular; that is, $\det\boldsymbol{M}(x_3) = 0$. From each of the two possible solutions in $\dot{z}_0$, the

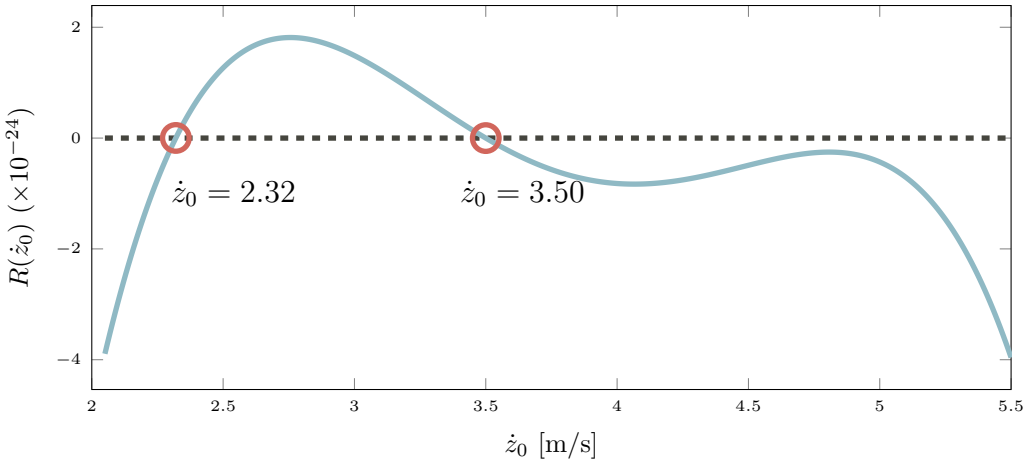

Figure 3.4. The resultant polynomial roots correspond to the possible $\dot{z}_0$ solutions.

solutions in the remaining coordinates are found by computing the kernel of $\boldsymbol{M}(\dot{z}_0)$.

$$\boldsymbol{M}(0.0023197)\mathbf{v} = \mathbf{0} \rightarrow \mathbf{v} = \begin{bmatrix} -3.21137 \\ -0.07331 \\ 2.17667 \\ -0.00167 \\ 0.04969 \\ -1.47536 \\ -0.00004 \\ 0.00113 \\ -0.03368 \\ 1.00000 \end{bmatrix}, \quad \boldsymbol{M}(0.0035000)\mathbf{v} = \mathbf{0} \rightarrow \mathbf{v} \begin{bmatrix} 0.00000 \\ 0.00000 \\ 0.00000 \\ 0.00000 \\ 0.00000 \\ 0.00150 \\ 0.00000 \\ 0.00000 \\ -0.00001 \\ 1.00000 \end{bmatrix},$$

where it is noted that the distance unit of the elements in the kernel vectors is kilometers. Because the tenth element is 1.0, the scale factor is consequently $\beta = 1.0$ and the $\dot{x}_0$ and $\dot{y}_0$ solutions correspond exactly to the sixth and ninth kernel elements,

respectively. Thus, it follows that the two possible relative velocity solutions are

$$\delta\dot{\mathbf{r}}_0 = \begin{bmatrix} -1475.355491135100 & -33.680914305322 & 2.319738379749 \end{bmatrix}^T \text{ [m/s]}$$

and

$$\delta\dot{\mathbf{r}}_0 = \begin{bmatrix} 1.500001264432 & -0.010000624179 & 3.500007679171 \end{bmatrix}^T \text{ [m/s]}\,.$$

It should be noted that, in this example, the relative Lambert routine finds multiple solutions, as compared to the traditional linear CW equations, which can produce, at most, one solution. Furthermore, in this example, the relative Lambert routine finds *only* two solutions—no extraneous roots are computed. In other words, no real-valued solutions are computed that do not actually satisfy the CW2 equations. By substituting these values into f_1, f_2 and f_3, it can be shown that these solutions do in fact solve the system of equations. However, even though large relative velocity solutions may satisfy the CW2 equations, when propagated forward in time, the corresponding relative ranges quickly grow too large to satisfy the underlying assumptions of the CW and CW2 models.

3.3. COMPARISON OF METHODS

Two alternative methods of solving the relative Lambert problem are considered and applied to a targeting scenario in order to benchmark the accuracy of the CW2 relative Lambert solver developed in this work. The first alternative method involves mapping relative position vectors into the inertial space, solving the Lambert problem using Battin's method [32], and finally mapping the velocity solutions that are obtained as outputs of the traditional Lambert (TL) solver back into the relative space. Because Battin's method is iterative, a maximum iteration limit is set at 1,000. The second alternative method utilizes standard linear CW dynamics and requires only simple matrix operations, as demonstrated in Equation (3.3).

A rendezvous scheme is simulated as follows. As illustrated in Figure 3.5, the inspector satellite occupies a geosynchronous orbit, with known inertial position and velocity $\mathbf{r}_0$ and $\dot{\mathbf{r}}_0$. This orbit is treated as the reference from which the Hill frame

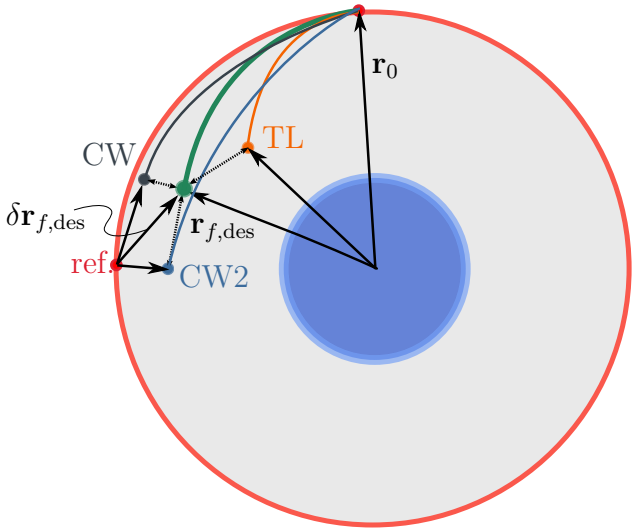

Figure 3.5. Trajectories of solutions given by Clohessy-Wiltshire, second order Clohessy-Wiltshire, and traditional Lambert solvers. The miss-distances are represented by the dashed lines.

is constructed. An external guidance algorithm provides an input in the form of a desired relative position (referenced from the original orbit) $\delta\mathbf{r}_{f,\text{des}}$ at time t_f. Each of the three methods is then used to calculate nominal velocities $\dot{\hat{\mathbf{r}}}_{0,\text{TL}}$, $\delta\dot{\hat{\mathbf{r}}}_{0,\text{CW2}}$, and $\dot{\hat{\mathbf{r}}}_{0,\text{CW}}$ at t_0 to achieve the desired rendezvous. The solutions obtained from the CW- and CW2-based methods are then mapped into the inertial frame to be propagated using the true dynamics (taken to be two-body motion). After all three solutions are propagated using two-body dynamics to time t_f, the resulting final positions are compared to the inertially-mapped desired position. Because the TL-based approach

is slightly more complicated than the other two methods, a block diagram of the method, including the error calculation, is provided in Figure 3.6.

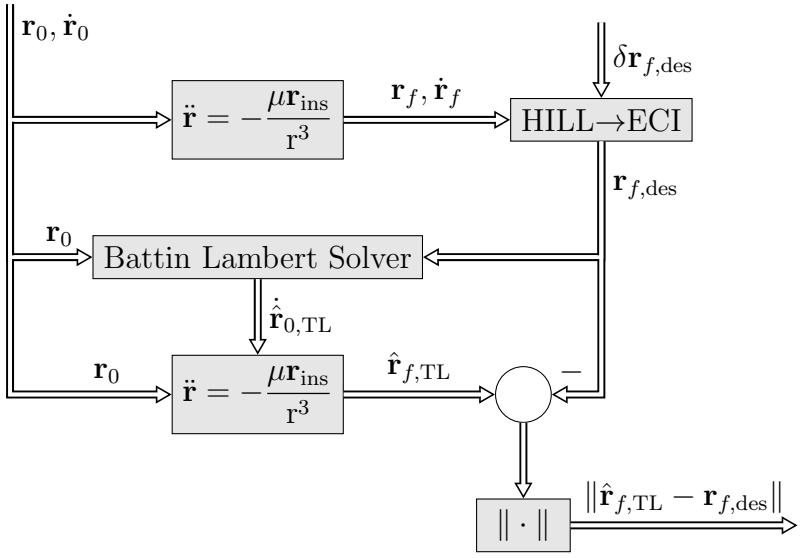

Figure 3.6. Flow chart of traditional Lambert approach to relative Lambert problem.

In order to properly compare the accuracy of the three solutions, $\hat{\dot{\mathbf{r}}}_{0,\text{TL}}$, $\delta\hat{\dot{\mathbf{r}}}_{0,\text{CW2}}$, and $\delta\hat{\dot{\mathbf{r}}}_{0,\text{CW}}$, the following rules are enforced:

- The two relative velocity solutions from the CW and CW2 solvers are converted to inertially referenced velocities. All three inertial solutions are then propagated in terms of the inertial frame using two-body dynamics to time t_f.
- The final positions are compared in the inertial frame to the desired position $\mathbf{r}_{f,\text{des}}$.
- The accuracy of the method is scored based on the magnitude of the final miss-distance, defined by $\|\hat{\mathbf{r}}_f - \mathbf{r}_{f,\text{des}}\|$.

The methods are compared by varying the desired relative position $\delta\mathbf{r}_{f,\text{des}}$ and computing the miss-distance for each solution. Due to the high dimensionality of the problem, that is, the four dimensions over which the input set can vary, the analysis is performed using an arbitrarily selected fixed time of flight of four hours and a constant desired cross-track component of $z_{f,\text{des}} = 0.5\,[\text{km}]$. The radial and along-track components of $\delta\mathbf{r}_{f,\text{des}}$ are varied between -10 and $10\,[\text{km}]$ and -20 and $20\,[\text{km}]$, respectively. For each value of $x_{f,\text{des}}$ and $y_{f,\text{des}}$, the final relative position is constructed, and each of the relative Lambert solver routines is used to compute the initial velocity, from which, using the above described procedure, the miss-distance is computed. The miss-distance for each method is shown in Figures 3.7a-3.7c.

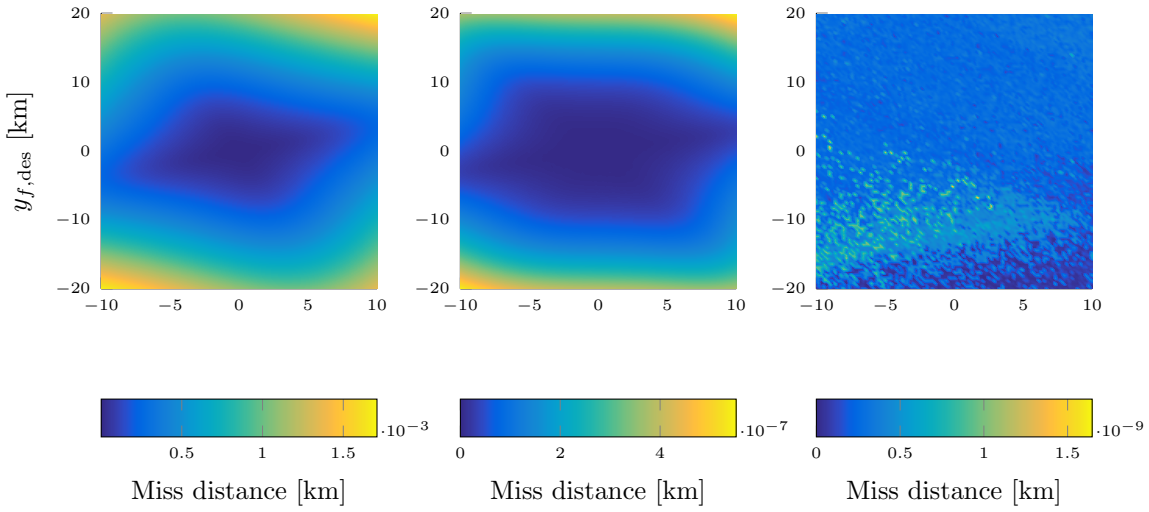

(a) CW miss-distance. (b) CW2 miss-distance. (c) TL solver miss-distance.

Figure 3.7. Miss distances of Lambert solvers with constant t_f and $z_{f,\text{des}}$.

As shown, under the assumption of two-body motion, the TL solver provides the most accurate rendezvous solutions, with miss-distances on the order of microns. The next best solutions are provided by the CW2 relative Lambert solver, which produces solutions 10,000 times more accurate than the CW solver. With both the

CW and CW2 solvers, distant target positions result in lower accuracy solutions, as the large magnitude of these relative position vectors impugn the integrity of the underlying dynamic assumptions.

Performing this same type of analysis uniformly over the full input space (i.e. varying t_f and $z_{f,\text{des}}$ in addition to $x_{f,\text{des}}$ and $y_{f,\text{des}}$) is infeasible due to the high dimensionality. Therefore, in an effort to characterize the performance of the three methods over the variables t_f, $x_{f,\text{des}}$, $y_{f,\text{des}}$, and $z_{f,\text{des}}$, a Monte Carlo simulation is employed. 10,000 simulations are run with randomly generated target positions ($\delta\mathbf{r}_{f,\text{des}}$) and travel times ($t_f$) uniformly distributed over $x_{f,\text{des}} \in [-10, 10]\,[\text{km}]$, $y_{f,\text{des}} \in [-20, 20]\,[\text{km}]$, $z_{f,\text{des}} \in [-5, 5]\,[\text{km}]$, and $t_f \in [5, 20]\,[\text{hr}]$. The miss-distances are shown in a histogram for each of the three methods in Figure 3.8. Although most of the data is embedded in the first bins of these plots, the abscissa scales of each plot capture the magnitude of the worst outlier cases. Again, these higher error cases are likely the product of trajectories that abuse the assumptions of relative motion.

In order to compare the three methods in the absence of outliers, the worst 5% of runs for each method are discarded, and the histograms of the lowest 95% miss-distance solutions are shown in Figure 3.9. As shown in Figure 3.9c, the CW solver generally produces solutions that pass within 10 [m] of the desired target with a median miss-distance of 4.1 [m]. The CW2 and traditional solvers surpass the CW method, as demonstrated in Figures 3.9a and 3.9b, achieving miss-distances on the order of centimeters and lower. A closer look at these histograms reveals that most of the miss-distances associated with the solutions generated by the CW2 solver fall under 1 [mm], with a median miss-distance of 0.95 [mm]. The best solutions are provided by the TL solver with a median miss-distance of 1.3 [μm].

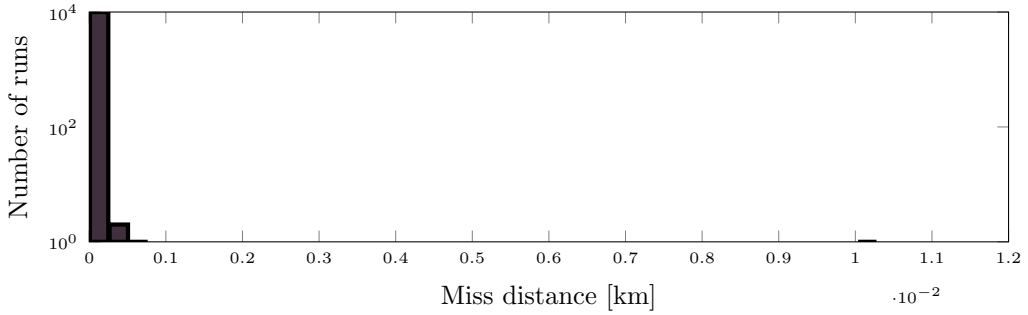

(a) TL solver miss-distance histogram.

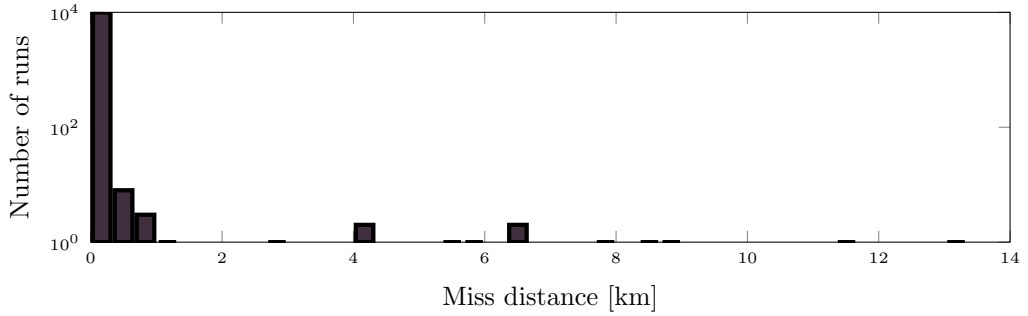

(b) CW2 relative Lambert solver miss-distance histogram.

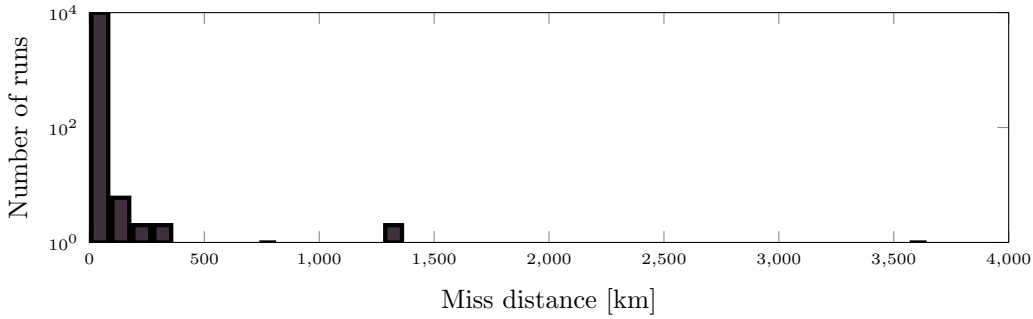

(c) CW relative Lambert solver miss-distance histogram.

Figure 3.8. Miss distance histograms for the three Lambert solver methods.

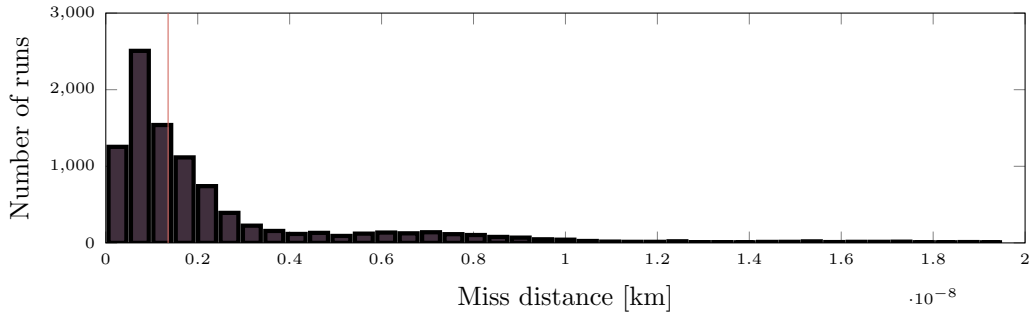

(a) TL solver miss-distance histogram. First 95% of points are shown.

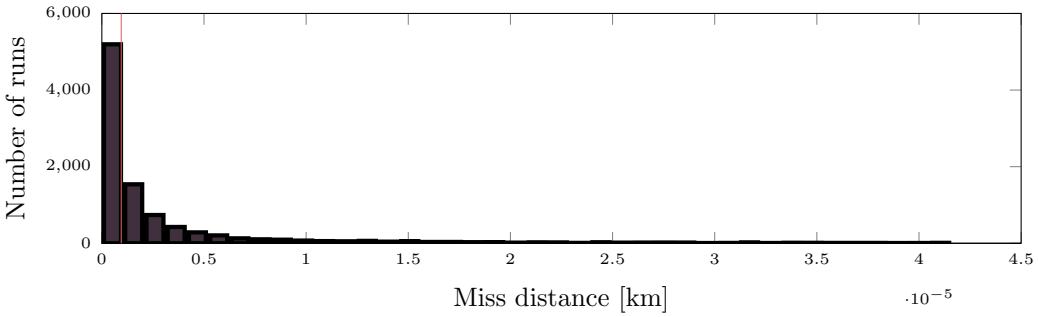

(b) CW2 relative Lambert solver miss-distance histogram. First 95% of points are shown.

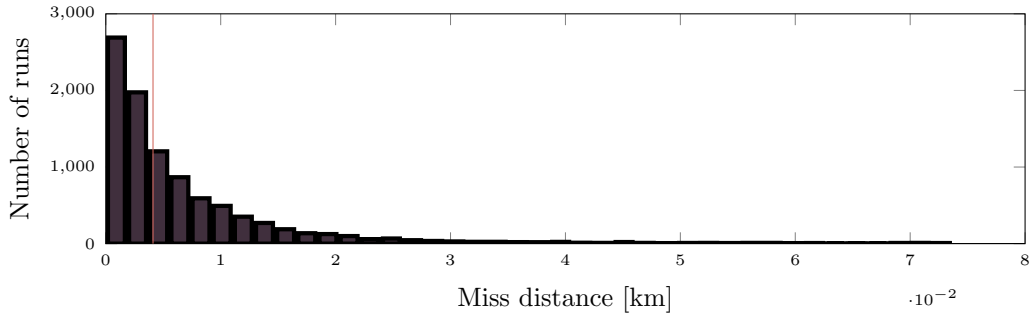

(c) CW relative Lambert solver miss-distance histogram. First 95% of points are shown.

Figure 3.9. Histograms of the best 95% miss-distance solutions. The median miss-distance values are shown in red.

What then, is the source of the error seen in the worst 5% of the CW, CW2, and TL solutions? The answer is clear from Figure 3.10, which sorts the complete set of miss-distances in terms of $\psi = n_0(t_f - t_0)$. As discussed in Chapter 3, the

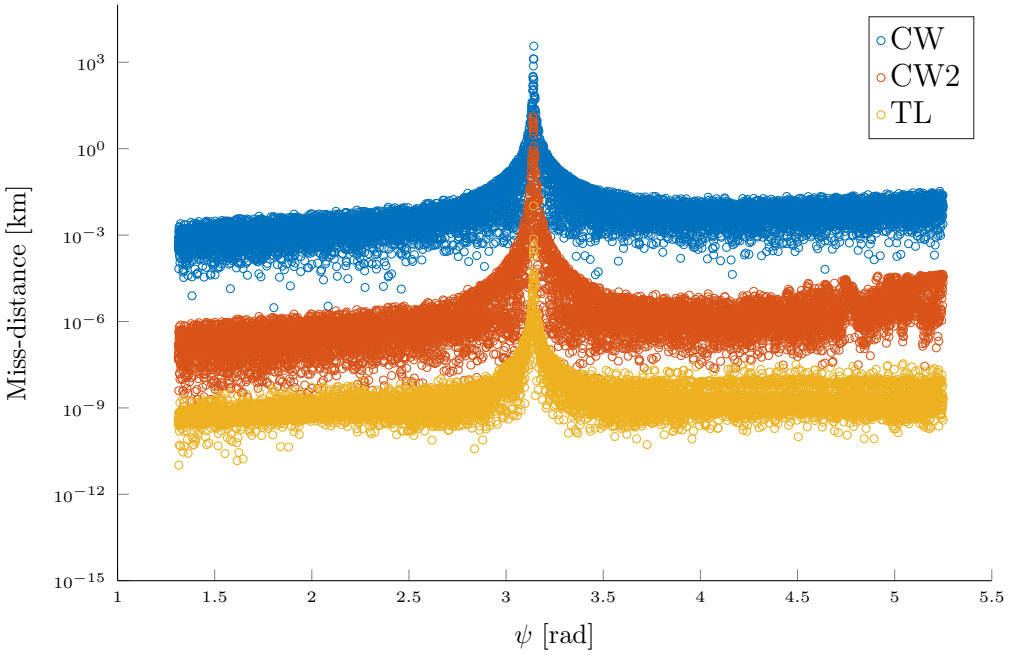

Figure 3.10. The complete set of miss-distances, arranged by $\psi = n_0(t_f - t_0)$.

CW and CW2 Lambert solvers suffer numerical issues at times of flight close to integer multiples of the reference orbital half-period. This is clearly demonstrated in Figure 3.10, where spikes in the miss-distance are seen near $\psi = \pi$, which directly corresponds to a time of flight equal to the orbital half-period. Interestingly, although the Battin method is capable of computing solutions at these times of flight [30], a significant degradation in accuracy is clearly observed around $\psi = \pi$ as well.

Altogether, the CW2 relative Lambert solver provides solutions that are several orders of magnitude better than the CW relative Lambert solver. Because the TL solver is based upon the full two-body dynamics, and the CW2 solver is based upon

approximations of the full two-body dynamics, higher-accuracy solutions are consistently found using the TL solver in comparison to the CW2 approach. However, in addition to required inputs of $\delta\mathbf{r}_0$, $\delta\mathbf{r}_f$, and $t_f - t_0$, the CW2 solver only requires knowledge of the reference orbital mean motion, as opposed to the TL solver, which additionally requires full state knowledge (inertial position and velocity) of the reference orbit. In many proximity operations involving relative targeting, accurate inertial orbital knowledge may be unavailable. In such situations, the CW2 relative Lambert solver provides targeting solutions with sub-centimeter miss-distances when 1) the reference orbit is circular, 2) the magnitude of the relative positions and velocities are not "too large" (i.e. they do not nullify the small deviation assumptions of the CW2 model), and 3) the times of flight are not close to integer multiples of the reference orbital half-period.

4. STEREOSCOPIC IMAGING

Stereoscopic imaging is widely used in terrestrial robotics applications. Only recently, however, has it been proposed as a mechanism for small satellite proximity operations [26, 27, 40]. Advantages of stereoscopic imaging for space-based imaging, in comparison to the previously mentioned relative sensing alternatives, include its passive sensing nature and the availability of inexpensive low-power commercial-off-the-shelf stereo cameras for small satellite applications.

When capturing stereoscopic images, a variety of image processing algorithms can be implemented for the purpose of object identification through edge and/or corner detection and feature extraction between a stereoscopic image pair. These algorithms include Canny edges [41], Harris corners [42], and speeded up robust features (SURF) [43], to name a few. Because a detailed analysis of these algorithms is beyond the scope of this thesis, it is assumed that the image processing system provides the projected object centroid's pixel coordinates $\boldsymbol{\epsilon}$, as shown in Figure 4.1. In most cases, the centroid will be offset from the object's center of mass and thus

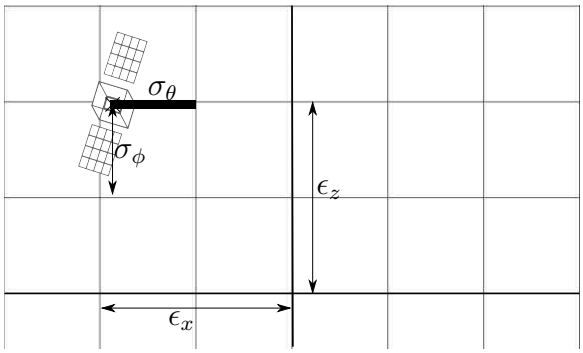

Figure 4.1. Centroid image coordinates and angle measurement deviations shown in image frame.

will not obey the point-mass equations of motion. However, for small targets, or for instances when the ratio of this offset to the relative range is very small, the errors induced by this difference are negligible. In proximity operations where the relative range is comparable to the size of target spacecraft (for example, docking missions), a more sophisticated knowledge of the target satellite's geometry, mass properties, and attitude is usually needed.

The geometry of a stereoscopic imager is shown in Figure 4.2. Given a set of

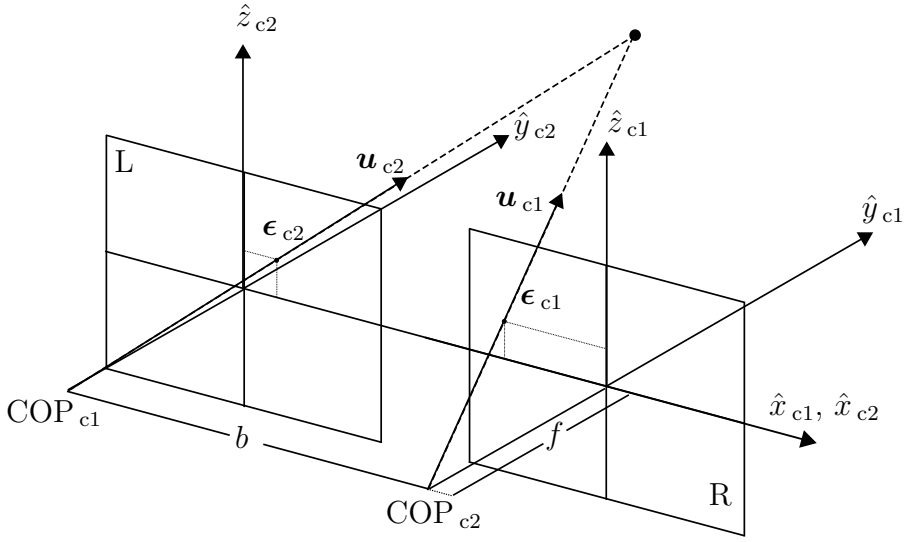

Figure 4.2. The stereoscopic LOS geometry. $\hat{x}_{c1}$-$\hat{y}_{c1}$-$\hat{z}_{c1}$ and $\hat{x}_{c2}$-$\hat{y}_{c2}$-$\hat{z}_{c2}$ define the Camera 1 frame and Camera 2 frame, respectively. Adapted from Ref. [27].

pixel coordinates and the effective optical focal length f, a camera frame-referenced line of sight (LOS) unit vector $\boldsymbol{u}$ is computed as

$$\boldsymbol{u} = \begin{bmatrix} u_x \\ u_y \\ u_z \end{bmatrix} = \frac{1}{\sqrt{(\epsilon_x)^2 + f^2 + (\epsilon_z)^2}} \begin{bmatrix} \epsilon_x \\ f \\ \epsilon_z \end{bmatrix} . \tag{4.1}$$

From an LOS unit vector, azimuth and elevation angles are extracted as

$$\theta = \arctan\left(u_x/u_y\right) \qquad \text{and} \qquad \phi = \arcsin\left(u_z\right) .$$

With a single camera, the azimuth and elevation angles do not provide enough information to resolve the three-dimensional position vector, as the range component is unknown. With the inclusion of a second camera and the knowledge of its placement with respect to the first camera, depth information can be determined. The system's measurement model is augmented by a second set of bearings to yield

$$\boldsymbol{y} = \left[\theta_{\,\mathrm{c1}},\, \phi_{\,\mathrm{c1}},\, \theta_{\,\mathrm{c2}},\, \phi_{\,\mathrm{c2}}\right]^T + \boldsymbol{\nu}_k \,.$$

The "cn" subscript denotes the camera's image frame in which the angles are expressed, as illustrated in Figure 4.2.

The placement of Camera 2 is quantified by the baseline b, which is the distance between the two cameras' centers of projection (COPs) from which the LOS vectors originate. The angular measurements are taken to be corrupted by zero-mean white noise $\boldsymbol{\nu}_k$ with covariance $\boldsymbol{R}_k$; that is

$$E\{\boldsymbol{\nu}_k\} = 0 \qquad \text{and} \qquad E\{\boldsymbol{\nu}_k {\boldsymbol{\nu}_k}^T\} = \boldsymbol{R}_k = \mathrm{diag}\{\sigma_\theta^2,\, \sigma_\phi^2,\, \sigma_\theta^2,\, \sigma_\phi^2\} \,,$$

where σ_θ and σ_ϕ are the measurement noise standard deviations in the azimuth and elevation angles, respectively. Note that, for convenience, the cameras are assumed to have the same noise characteristics, but this assumption is easily relaxed. For instance, the inspector satellite could be equipped with both narrow-field and wide-field cameras.

Using the angle measurements and the known location and orientation of each camera, standard triangulation schemes can be used to compute the range and thus

fully resolve the nearby space object's relative position. However, due to the imperfection of angular measurements, traditional stereoscopic measurement schemes rely on the minimization of the Euclidean distance between the two camera-originated skew LOS vectors to produce an approximate relative position measurement. The minimization process is nonlinear in nature [44] and the inner product between two unbiased LOS vectors is in fact biased [45]. The assumption of zero-mean Gaussian noise in position is therefore invalidated, and a better quantification of relative position uncertainty is sought. To illustrate, an arbitrary relative position is chosen, and 1,000 stereoscopic azimuth and elevation angles are generated and corrupted with zero-mean white noise. The corrupted angular measurements are then used to best recreate the relative position vector using the standard triangularization method. The recreated relative position vectors are shown in coordinate form in Figure 4.3. As shown, the resulting distributions are clearly non-Gaussian and biased, and thus,

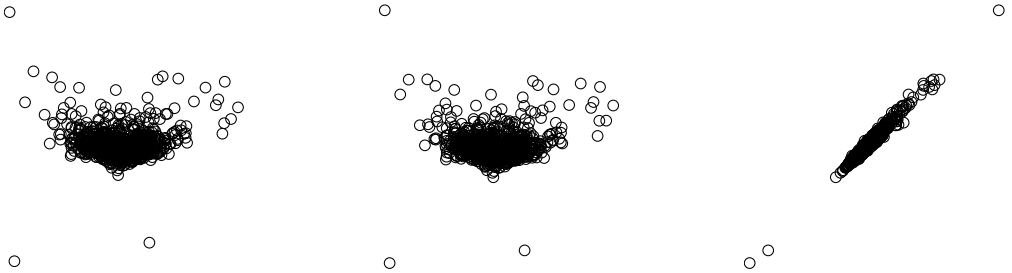

(a) x-y view (b) x-z view (c) y-z view

Figure 4.3. Typical non-Gaussian distribution of triangulated positions generated from Gaussian-distributed angular measurements.

when using stereoscopically triangulated measurements, the assumption of zero-mean Gaussian distributed noise cannot be made.

The aforementioned issues can be mitigated by skipping the triangularization step and directly processing incoming angles data. To initialize the navigation

process, however, a pdf must be formed that includes the missing relative range information. A new approach, which was first introduced by the author in Reference [46], is taken, in which the uncertainty in one camera's LOS is used to bound possible ranges along the other camera's LOS, over which uniform uncertainty is assumed. By assuming uniform relative range uncertainty over a statistically bounded relative position space, initial relative orbit determination (IROD) is performed conservatively, thereby improving the odds that all plausible true states are contained within the pdf, even in the event of poor initial measurements.

5. SINGLE TARGET TRACKING

In this chapter, the applications of modern ground-based angles-only orbit determination techniques to the relative orbit determination problem are investigated. In Reference [47], the range along ground-based line of sight (LOS) measurements is bounded by orbital range constraints. By generating candidate positions within the bounded LOS segment for multiple measurements, candidate orbits are postulated by applying a Lambert solver for each possible point combination. Reference [8] presents a similar approach in which the orbiting body's admissible region is constructed to determine bounds on range and range-rate relative to the observer. Gaussian mixture approximations are then applied to the admissible region in order to generate an initial pdf associated with uniform ambiguity within the admissible region.

A hybrid approach motivated by the work of References [47] and [8] is considered and applied to initial relative orbit determination (IROD). Stereoscopic measurements of a target and their associated geometry are used to bound potential relative range values along a single LOS originating from one of the inspector spacecraft's cameras. A Gaussian mixture (GM) is used to approximate the relative range uncertainty under the assumption of a uniform distribution in relative range. After GMs are constructed at two measurement times, a relative Lambert solver, which makes use of CW2 dynamics, connects all Gaussian component combinations to formulate a full state initial pdf in relative position and velocity. After IROD is completed, the initial pdf is then further refined through processing subsequent angles-only measurement data in a Bayesian framework. For brevity and simplicity, uncertainties in the inspector's attitude and camera alignment and the uncertainty in the target's center of mass are not considered in this work. Preliminary results are published in Reference [48]. The current work is a more comprehensive study.

5.1. GAUSSIAN MIXTURE MODELS

In order to quantify the assumed uniform relative range uncertainty associated with a stereoscopic measurement, a uniform pdf can be approximated by a GM. Previous works have shown that a large class of pdfs, including uniform pdfs, can be modeled by a GM [49, 50]. The uniform distribution, which is given by

$$p(x) = \begin{cases} \dfrac{1}{b-a} & , \quad a \leq x \leq b \\ 0 & , \quad \text{otherwise} \end{cases}$$

can be approximated by a GM pdf of the form [49]

$$q(x) = \sum_{\ell=1}^{L} w^{(\ell)} p_g(x\,;\, m^{(\ell)}, P^{(\ell)})\,, \tag{5.1}$$

where L is the total number of components and $w^{(\ell)}$, $m^{(\ell)}$, and $P^{(\ell)}$ are the discrete probability, mean, and covariance, respectively, of the ℓ^{th} Gaussian component, and $p_g(x\,;\, a, A)$ represents a Gaussian pdf for the random variable x with mean a and covariance A, such that

$$p_g(x\,;\, a, A) = |2\pi A|^{-1/2} \exp\left\{ -\frac{1}{2}(x-a)^T A^{-1}(x-a) \right\}\,.$$

To find the optimal set of weights, means, and covariances in Equation (5.1) that best approximate the true distribution, the difference between the true and approximate distributions is taken as the L_2 norm via

$$L_2[p||q] = \int (p(x) - q(x))^2 dx\,.$$

To make the optimization problem tractable, Reference [8] assumes that the weights are equal, the components are homoscedastic, and the means are evenly distributed

across the support of $p(x)$, which reduces the L_2 distance to

$$L_2[p||q] = \frac{1}{b-a} + \frac{w^2}{2\sqrt{\pi}\sigma} \sum_{i=1}^{L} \sum_{j=1}^{L} \exp\left\{-M_{i,j}^2\right\} - \frac{w}{b-a} \sum_{\ell=1}^{L} \left[\operatorname{erf}\left\{B_\ell\right\} - \operatorname{erf}\left\{A_\ell\right\}\right] ,$$

where

$$A_\ell \triangleq \left(\frac{a - m^{(\ell)}}{\sqrt{2}\sigma}\right) , \qquad B_\ell \triangleq \left(\frac{b - m^{(\ell)}}{\sqrt{2}\sigma}\right) , \qquad \text{and} \qquad M_{i,j}^2 \triangleq \left(\frac{m^{(i)} - m^{(j)}}{2\sigma}\right)^2$$

and requires optimization only over the common standard deviation parameter, $\sigma = \sqrt{P^{(\ell)}}$. The aforementioned optimization consists of finding the roots of the L_2 derivative with respect to σ, given as

$$\begin{aligned} \frac{dL_2[p||q]}{d\sigma} = & \frac{w^2}{2\sqrt{\pi}\sigma^2} \sum_{i=1}^{L} \sum_{j=1}^{L} \left[2M_{i,j}^2 - 1\right] \exp\left\{-M_{i,j}^2\right\} \\ & - \frac{2w}{(b-a)\sqrt{\pi}\sigma} \sum_{\ell=1}^{L} \left[A_\ell \exp\left\{-A_\ell^2\right\} - B_\ell \exp\left\{-B_\ell^2\right\}\right] = 0 . \end{aligned}$$

5.1.1. Library of Solutions. Reference [8] demonstrates that by performing the optimization for the case of $a = 0$ and $b = 1$, a generalized library of solutions can be produced, which can then be easily scaled to any arbitrary uniform distribution. For the case of $a = 0$ and $b = 1$, the optimal standard deviation (i.e. the σ value that yields a zero derivative), is denoted as $\tilde{\sigma}$. It follows that the component weights and means can be calculated as

$$\tilde{w}^{(\ell)} = \tilde{w} = \frac{1}{L} \qquad \text{and} \qquad \tilde{m}^{(\ell)} = \frac{\ell}{L+1} \;\; \forall \;\; \ell \in \{1, 2, \ldots, L\} .$$

Here, the "˜" notation denotes values obtained from the generalized case of $a = 0$ and $b = 1$. The prominent advantage in generating a general library is that it needs to be computed only once, as the obtained values are directly scalable to any approximation.

To extend the library to an arbitrary uniform distribution, the generalized parameters are scaled as follows:

$$w = \tilde{w}\,, \qquad m^{(\ell)} = a + (b-a)\tilde{m}^{(\ell)}\,, \qquad \sigma = (b-a)\tilde{\sigma}\,.$$

It is intuitive that increasing the number of components L used will result in a closer approximation to the true uniform distribution (Figure 5.1). Because computational cost also increases with L, an appropriate value must be chosen, especially when considering current satellite flight-hardware processing and memory limitations. To control the accuracy/computational cost reciprocity, the acceptable maximum deviation parameter, $\sigma_{\max}$ is specified. The precomputed general library is then searched to find L, such that $\tilde{\sigma}(b-a) \leq \sigma_{\max}$. This method ensures that no superfluous computations are made for the given mission requirements.

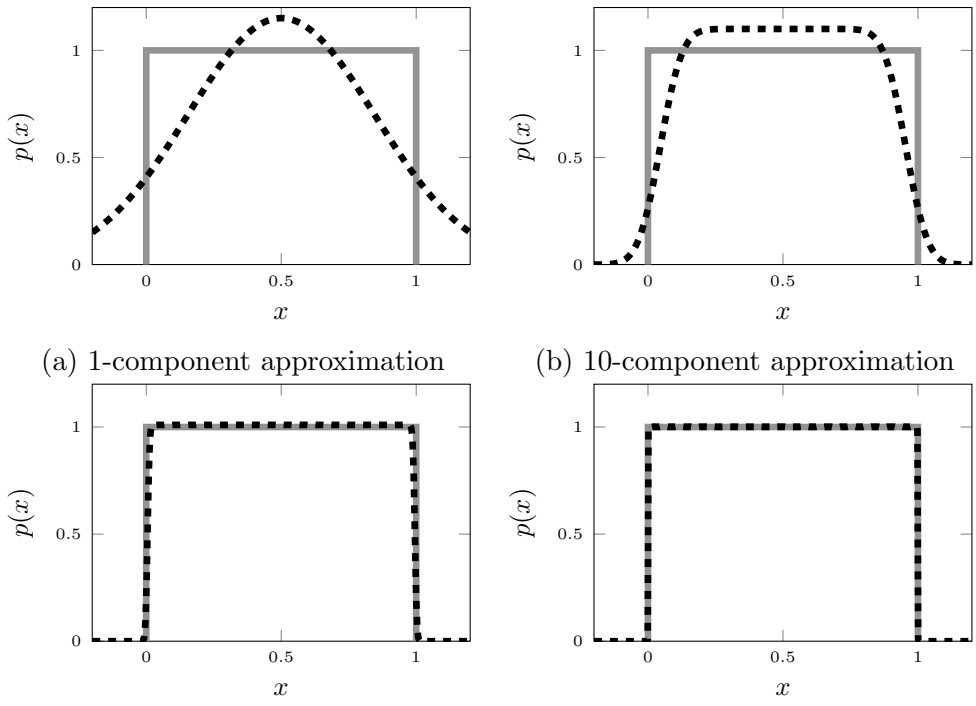

(a) 1-component approximation (b) 10-component approximation

(c) 100-component approximation (d) 1000-component approximation

Figure 5.1. GM approximation of a uniform pdf for different numbers of components. The uniform pdf is given by the solid line and the GM pdf is given by the dashed line.

5.2. GM APPROXIMATION OF STEREOSCOPIC MEASUREMENT UNCERTAINTY

The uncertainty in one camera's LOS can be used to bound possible ranges along the other camera's LOS, over which equal uncertainty is assumed. To establish the range boundaries, a rectangular-based pyramid is formed about Camera 2's LOS vector that represents the uncertainty of the measurement. The pyramid is constructed using user-specified half-angles that are equal to some multiple of the angular measurement standard deviations, σ_θ and σ_ϕ. For example, the half angles can be chosen as $3\sigma_\theta$ and $3\sigma_\phi$, as is done later in Section 5.5.

For a given stereo measurement, the range constraints along Camera 1's LOS are obtained by finding the two points of intersection between Camera 1's LOS and the uncertainty pyramid, as shown in Figure 5.2. These points, $\rho_{\min}$ and $\rho_{\max}$, represent

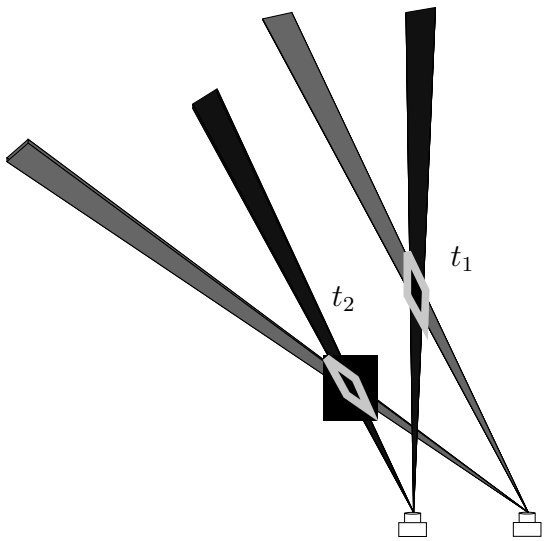

Figure 5.2. Uncertainty bounding of bearings-only measurements.

the minimum and maximum possible ranges along $\boldsymbol{u}_{c1}$ in which the imaged target's position is hypothesized, as shown in Figure 5.3. Equal uncertainty in the range

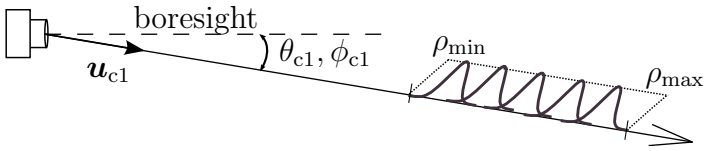

Figure 5.3. Gaussian mixture approximating uniform uncertainty $\in \rho_{\min} \leq \rho \leq \rho_{\max}$.

component is assumed over these bounds, such that

$$p(\rho) = \begin{cases} \dfrac{1}{\rho_{\max} - \rho_{\min}} & , \quad \rho_{\min} \leq \rho \leq \rho_{\max} \\ 0 & , \quad \text{otherwise} \end{cases}$$

Specification of $\rho_{\min}$ and $\rho_{\max}$, along with the accuracy parameter, $\sigma_{\rho,\max}$, provides the required information to determine a Gaussian mixture approximation of $p(\rho)$ using the previously described method. Note that $\sigma_{\rho,\max}$ is analogous to $\sigma_{\max}$, as described in Section 5.1, and is used to control the resolution of the GM approximation. The range pdf is modeled by

$$p(\rho) = \sum_{\ell=1}^{L} w_{\rho}^{(\ell)} p_g(\rho\,;\, m_{\rho}^{(\ell)}, {\sigma_{\rho}^{(\ell)}}^2)\,, \tag{5.2}$$

where

$$w_{\rho}^{(\ell)} = \frac{1}{L}\,, \qquad m_{\rho}^{(\ell)} = \rho_{\min} + \frac{(\rho_{\max} - \rho_{\min})\,\ell}{L+1}\,, \qquad \text{and} \qquad \sigma_{\rho}^{(\ell)} = \left((\rho_{\max} - \rho_{\min})\,\tilde{\sigma}_{\rho}\right)\,.$$

The position of the nearby spacecraft with respect to Camera 1 can be expressed in spherical coordinates as

$$\boldsymbol{z}_k = \left[\rho,\, \theta_{\,c1},\, \phi_{\,c1}\right]^T.$$

The relative position pdf $p(\boldsymbol{z}_k)$ is obtained by extending Equation (5.2) to include the Gaussian uncertainty in the azimuth and elevation angles, resulting in

$$p(\boldsymbol{z}_k) = \sum_{\ell=1}^{L} w_z^{(\ell)} p_g(\boldsymbol{z}_k\,;\, \boldsymbol{m}_z^{(\ell)}, \boldsymbol{S}_z^{(\ell)} \boldsymbol{S}_z^{(\ell)^T})\,, \tag{5.3}$$

where

$$w_z^{(\ell)} = w_\rho^{(\ell)}\,, \qquad \boldsymbol{m}_z^{(\ell)} = \left[m_\rho^{(\ell)},\, \theta_{\,\mathrm{c1}},\, \phi_{\,\mathrm{c1}}\right]^T, \qquad \text{and} \qquad \boldsymbol{S}_z^{(\ell)} = \mathrm{diag}\{\sigma_\rho^{(\ell)},\, \sigma_\theta,\, \sigma_\phi\}$$

In other words, the pdf $p(\boldsymbol{z}_k)$ is approximated by the sum of the pdfs of linearly spaced range means $m_\rho^{(\ell)}$, each with uncertainty in the range, azimuth angle, and elevation angle. The resulting pdf is approximately uniform in range and Gaussian in azimuth and elevation.

5.3. LINKAGE

Equation (5.3) gives the probability distribution of the random position variable $\boldsymbol{z}_k$ in three spherical coordinates relative to the camera frame. To construct the full six-dimensional pdf, both the relative position and relative velocity in Cartesian coordinates are needed. The purpose of the linkage process is to transform two three-dimensional position pdfs, which are constructed at times t_1 and t_2 in spherical coordinates, to a six-dimensional pdf in Cartesian coordinates. This new pdf is formed by "linking" the two initial pdfs via the relative Lambert solver (Chapter 3).

5.3.1. State Linking. In order to transform a set of spherical coordinate position vectors at t_1 and t_2 to a full Cartesian state $\boldsymbol{x}_1$, the nonlinear function $\boldsymbol{g}(\bar{\boldsymbol{z}})$ is defined as

$$\boldsymbol{x}_k = \boldsymbol{g}(\bar{\boldsymbol{z}}) = \begin{bmatrix} \delta\mathbf{r}_k(\bar{\boldsymbol{z}}) \\ \delta\dot{\mathbf{r}}_k(\bar{\boldsymbol{z}}) \end{bmatrix}, \qquad \text{where} \quad \bar{\boldsymbol{z}} = \begin{bmatrix} \boldsymbol{z}_k \\ \boldsymbol{z}_{k+1} \end{bmatrix}.$$

The relative position $\delta\mathbf{r}_k$ describes the position of the nearby spacecraft with respect to the origin of the Hill frame at t_k and requires mapping from spherical to Cartesian coordinates and the addition of the cameras' positions. For convenience, the camera orientations are chosen such that they align with the Hill frame. Note that the linkage process can be performed between any two times t_k and t_{k+1}. However, for ease of exposition, the process is presented in terms of t_1 and t_2. At times t_1 and t_2, the Cartesian positions are computed from the spherical coordinates and camera positions as

$$\delta\mathbf{r}_1(\bar{\boldsymbol{z}}) = \rho_1 \begin{bmatrix} \sin\phi_1 \cos\theta_1 \\ \sin\phi_1 \sin\theta_1 \\ \cos\phi_1 \end{bmatrix} + \boldsymbol{d}_{\,\mathrm{c1},1} \qquad \text{and} \qquad \delta\mathbf{r}_2(\bar{\boldsymbol{z}}) = \rho_2 \begin{bmatrix} \sin\phi_2 \cos\theta_2 \\ \sin\phi_2 \sin\theta_2 \\ \cos\phi_2 \end{bmatrix} + \boldsymbol{d}_{\,\mathrm{c1},2}\,.$$

Here, $\boldsymbol{d}_{\,\mathrm{c1},k}$ is the position of Camera 1's COP with respect to the Hill frame origin at time t_k. Recall that the intent is to formulate an initial pdf in relative positions *and* relative velocity, and thus, the relative Lambert solver is applied to compute the velocity at time t_1. In functional form,

$$\delta\dot{\mathbf{r}}_1(\bar{\boldsymbol{z}}) = \text{RelativeLambert}\left(\delta\mathbf{r}_1, \delta\mathbf{r}_2, t_2 - t_1\right)\,. \tag{5.4}$$

Note that both the CW and CW2 relative Lambert solvers of Chapter 3 may be readily used in Equation (5.4). The traditional Lambert approach, as also described in Chapter 3, additionally requires accurate knowledge of the chief's inertial position and velocity, and therefore is not considered in this development. Thus far, this section has presented a *deterministic* mapping from a dual set of camera-referenced spherical coordinates to a Hill-referenced relative position and velocity. The formulation of the

full state pdf in relative position and velocity requires that the uncertainty of the stereoscopic measurements be mapped through this process.

5.3.2. Uncertainty Mapping. Recall that $p(\boldsymbol{z}_1)$ and $p(\boldsymbol{z}_2)$ are known and are taken to be independent, such that the joint pdf is given by the product of the pdfs via $p(\bar{\boldsymbol{z}}) = p(\boldsymbol{z}_1)p(\boldsymbol{z}_2)$. The multiplication of these pdfs, which are modeled by GMs, is obtained by computing the joint distribution between every permutation of GM component pairs between t_1 and t_2. Because there are L_1 components in $p(\boldsymbol{z}_1)$ and L_2 components in $p(\boldsymbol{z}_2)$, $p(\bar{\boldsymbol{z}})$ contains $L_1 \cdot L_2$ components. The resulting pdf $p(\bar{\boldsymbol{z}})$ is then mapped to the desired state variable space via the mapping $\boldsymbol{g}(\cdot)$ to obtain $p(\boldsymbol{x}_1)$.

The relative position distribution at time t_1 is directly known (in spherical coordinates) from $p(\boldsymbol{z}_1)$, but the relative velocity distribution at time t_1 is not directly known. In order to determine the relative velocity distribution at time t_1, each component of the GM representation of $p(\bar{\boldsymbol{z}})$ is mapped through $\boldsymbol{g}(\cdot)$. This is equivalent to mapping each pair of components from the GMs of $p(\boldsymbol{z}_1)$ and $p(\boldsymbol{z}_2)$, which represent the relative position distributions at times t_1 and t_2, respectively. To perform this component-wise mapping, an unscented transformation is employed [51]. The initial mean, uncertainty, and discrete probability of a given pair of relative positions can be represented by the combination of the relative position component means, covariance square-root factor matrices, and weights at t_1 and t_2; that is

$$\boldsymbol{m}_{\bar{z}} = \begin{bmatrix} \boldsymbol{m}_{z,1} \\ \boldsymbol{m}_{z,2} \end{bmatrix}, \qquad \boldsymbol{S}_{\bar{z}} = \begin{bmatrix} \boldsymbol{S}_{z,1} & \boldsymbol{0}_{3\times 3} \\ \boldsymbol{0}_{3\times 3} & \boldsymbol{S}_{z,2} \end{bmatrix}, \qquad \text{and} \qquad w_{\bar{z}} = w_{z,1} w_{z,2}\,,$$

where $\boldsymbol{0}_{3\times 3}$ denotes the 3×3 zero matrix. First, given the state dimension $n = 6$, the $n \times 1$ mean vector $\boldsymbol{m}_{\bar{z}}$, and the $n \times n$ square-root factor $\boldsymbol{S}_{\bar{\boldsymbol{z}}}$, $2n$ sigma points $\boldsymbol{\mathcal{Z}}$ are

chosen as [52]

$$\boldsymbol{\mathcal{Z}} = \left[\begin{array}{ccc} \boldsymbol{m}_{\bar{z}} & \cdots & \boldsymbol{m}_{\bar{z}} \end{array} \right] + \left[\begin{array}{cc} -\sqrt{n}\boldsymbol{S}_{\bar{z}} & \sqrt{n}\boldsymbol{S}_{\bar{z}} \end{array} \right] . \tag{5.5}$$

The transformed sigma points are then calculated as

$$\mathcal{X}^{(i)} = \boldsymbol{g}\left(\mathcal{Z}^{(i)}\right) , \tag{5.6}$$

where $\mathcal{Z}^{(i)}$ denotes the i^{th} column of $\boldsymbol{\mathcal{Z}}$. The transformed full Cartesian state mean and covariance square-root factors can then be calculated as

$$\boldsymbol{m}_x = \frac{1}{2n} \sum_{i=1}^{2n} \mathcal{X}^{(i)} , \tag{5.7}$$

$$\boldsymbol{S}_x \leftarrow \text{qr}\left\{\boldsymbol{A}\right\}, \qquad \boldsymbol{A} = \frac{1}{\sqrt{2n}} \left[\begin{array}{c|c|c|c} \mathcal{X}^{(1)} - \boldsymbol{m}_x & \mathcal{X}^{(2)} - \boldsymbol{m}_x & \cdots & \mathcal{X}^{(2n)} - \boldsymbol{m}_x \end{array} \right] , \tag{5.8}$$

where "qr{ }" represents the application of a QR decomposition [53], returning only $\boldsymbol{R}$, where $\boldsymbol{A} = \boldsymbol{QR}$. This transformation is repeated for every combination of the components of $p(\boldsymbol{z}_1)$ and $p(\boldsymbol{z}_2)$ (see Eq. 5.3), as illustrated in Figure 5.4. Each linkage generates a new Gaussian component, resulting in $L_1 \cdot L_2$ total components. These components are then summed in the same fashion of Equation (5.1) to complete the full initial state pdf approximation at t_1; that is,

$$q(\boldsymbol{x}_1) = \sum_{\ell=1}^{L_1} \sum_{j=1}^{L_2} w_x^{(\ell,j)} p_g(\boldsymbol{x}\,;\, \boldsymbol{m}_x^{(\ell,j)}, \boldsymbol{S}_x^{(\ell,j)} \boldsymbol{S}_x^{(\ell,j)^T}) , \tag{5.9}$$

where

$$w_x^{(\ell,j)} = w_z^{(\ell)} w_z^{(j)} , \tag{5.10}$$

and $\boldsymbol{m}_x^{(\ell,j)}$ and $\boldsymbol{S}_x^{(\ell,j)}$ are found by the application of Equations (5.7) and (5.8) for every (ℓ,j) component link. The complete algorithm is summarized in Algorithm 2.

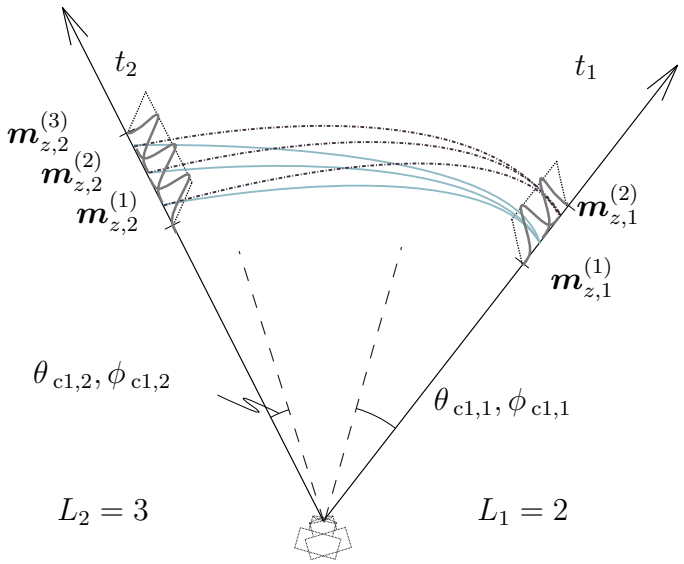

Figure 5.4. Gaussian mixture linkage between t_1 and t_2.

Algorithm 2: Gaussian Mixture Construction (IROD)

Compute $p(\boldsymbol{z}_1)$ for t_1 and $\theta_{\text{c1,1}}, \phi_{\text{c1,1}}$ (Eq. 5.3)

Compute $p(\boldsymbol{z}_2)$ for t_2 and $\theta_{\text{c1,2}}, \phi_{\text{c1,2}}$ (Eq. 5.3)

for $\ell = 1, ...L_1$ **do**

  for $j = 1, ..., L_2$ **do**

    Construct $\boldsymbol{m}_{\tilde{z}}^{(\ell,j)}$ from:

      ℓ^{th} mean of $p(\boldsymbol{z}_1)$ at t_1

      j^{th} mean of $p(\boldsymbol{z}_2)$ at t_2

    Construct $\boldsymbol{S}_{\tilde{z}}^{(\ell,j)}$ from:

      ℓ^{th} covariance of $p(\boldsymbol{z}_1)$ at t_1

      j^{th} covariance of $p(\boldsymbol{z}_2)$ at t_2

    Compute $\boldsymbol{\mathcal{Z}}$ (Eq. 5.5)

    for $i = 1, ..., 2n$ **do**

      Compute $\mathcal{X}^{(i)}$ (Eq. 5.6)

    end for

    Compute $w_x^{(\ell,j)}$ (Eq. 5.10)

    Compute $\boldsymbol{m}_x^{(\ell,j)}$ (Eq. 5.7)

    Compute $\boldsymbol{S}_x^{(\ell,j)}$ (Eq. 5.8)

  end for

end for

Output $q(\boldsymbol{x}_1)$ (Eq. 5.9)

5.4. RECURSIVE STATE ESTIMATION

To predict the state of the spacecraft at future times, standard Bayesian filtering techniques are employed [54]. The systems used for propagation and measurement prediction are nonlinear and are given by

$$\boldsymbol{x}_k = \boldsymbol{f}(\boldsymbol{x}_{k-1}) \qquad \text{and} \qquad \boldsymbol{y}_k = \boldsymbol{h}(\boldsymbol{x}_k) + \boldsymbol{\nu}_k \,,$$

where $\boldsymbol{f}(\cdot)$ is the application of the CW2 equations (Eqs. 2.16), $\boldsymbol{\nu}_k$ is zero-mean Gaussian white noise with $E\{\boldsymbol{\nu}_k^T \boldsymbol{\nu}_k\} = \boldsymbol{R}_k$, and

$$\boldsymbol{h}(\boldsymbol{x}_k) = \begin{bmatrix} \arctan\left(u_{\,\mathrm{c1},k,x} / u_{\,\mathrm{c1},k,y}\right) \\ \arcsin\left(u_{\,\mathrm{c1},k,z}\right) \\ \arctan\left(u_{\,\mathrm{c2},k,x} / u_{\,\mathrm{c2},k,y}\right) \\ \arcsin\left(u_{\,\mathrm{c2},k,z}\right) \end{bmatrix}, \qquad \text{where} \qquad \boldsymbol{u}_{\,\mathrm{cn},k} = \frac{\delta\mathbf{r}_k - \boldsymbol{d}_{\,\mathrm{cn},k}}{\|\delta\mathbf{r}_k - \boldsymbol{d}_{\,\mathrm{cn},k}\|} \,, \quad (5.11)$$

noting that $\delta\mathbf{r}_k$ is the relative position portion of the state vector $\boldsymbol{x}_k$.

Bayesian estimation can be broken into two fundamental steps: prediction and correction. In the prediction step, the posterior pdf of the state $\boldsymbol{x}_{k-1}$, given the dynamic model, is integrated to find the predicted distribution at t_k via the Chapman-Kolmogorov equation [54], given as

$$p(\boldsymbol{x}_k|\boldsymbol{Y}^{k-1}) = \int p(\boldsymbol{x}_k|\boldsymbol{x}_{k-1}) p(\boldsymbol{x}_{k-1}|\boldsymbol{Y}^{k-1}) d\boldsymbol{x}_{k-1}, \quad (5.12)$$

where $\boldsymbol{Y}^{k-1}$ is the set of all prior measurements up to and including $\boldsymbol{y}_{k-1}$. The corrector step updates the predicted (prior) distribution with the new measurement $\boldsymbol{y}_k$ via Bayes rule [54], given as

$$p(\boldsymbol{x}_k|\boldsymbol{Y}^k) = \frac{p(\boldsymbol{y}_k|\boldsymbol{x}_k) p(\boldsymbol{x}_k|\boldsymbol{Y}^{k-1})}{\int p(\boldsymbol{y}_k|\boldsymbol{x}_k) p(\boldsymbol{x}_k|\boldsymbol{Y}^{k-1}) d\boldsymbol{x}_k} \,. \quad (5.13)$$

In general, direct computation of the multidimensional integrals in Equations (5.12) and (5.13) is infeasible except for special cases, such as linear Gaussian systems [55]. In most other cases, approximate forms must be used. For a comprehensive list of these approximate forms, the reader is directed to References [55] and [54].

The approximate method considered in this thesis is the Gaussian mixture square-root unscented Kalman filter (GMSRUKF) [55]. The GMSRUKF is simply the square-root unscented Kalman filter (SRUKF) algorithm implemented in parallel for each Gaussian component, with an additional weight update after each measurement update. It is noted that the Gaussian mixture square-root extended Kalman filter would likely perform similarly to the GMSRUKF in this application. However, the GMSRUKF is chosen here to maintain consistency with the nonlinear approximation approaches employed in the linkage process (Section 5.3).

The initial state is taken to be random with pdf $p(\boldsymbol{x}_1)$, which is constructed using the GM approach and linkage process that is detailed in Section 5.3 and outlined in Algorithm 2. This initial pdf is described by $q(\boldsymbol{x}_{k-1})$, as given in Equation (5.9), or through a simple rewriting as

$$p(\boldsymbol{x}_1) = \sum_{\ell=1}^{L} w_{x,1}^{(\ell)} p_g(\boldsymbol{x}_1 \,;\, \boldsymbol{m}_{x,1}^{(\ell)}, \boldsymbol{S}_{x,1}^{(\ell)} \boldsymbol{S}_{x,1}^{(\ell)^T}) \,.$$

5.4.1. Predictor. At time t_{k-1}, the posterior pdf is given as a GM of the form

$$p(\boldsymbol{x}_{k-1} \,|\, \boldsymbol{Y}^{k-1}) = \sum_{\ell=1}^{L} w_{x,k-1}^{(\ell)} p_g(\boldsymbol{x}_{k-1} \,;\, \boldsymbol{m}_{x,k-1}^{(\ell)}, \boldsymbol{S}_{x,k-1}^{(\ell)} \boldsymbol{S}_{x,k-1}^{(\ell)^T}) \,.$$

In order to process incoming measurement data at time t_k, the posterior pdf must be propagated forward in time via the predictor step to obtain the predicted (or prior) pdf $p(\boldsymbol{x}_k|\boldsymbol{Y}^{k-1})$. In the predictor step, the weights, means, and covariance square-root

factors are propagated using the unscented Kalman filter (UKF) in square-root form as presented in [52]. The use of square-root factors in place of traditional covariance matrix propagation has been shown to improve both computational stability and cost. The SRUKF algorithm (Eqs. 5.14-5.24) is applied to *each* Gaussian component ℓ. For compactness, the (ℓ) superscript is omitted in the remainder of this section.

First, sigma points are generated on the basis of the mean and the covariance square-root factor as

$$\boldsymbol{\mathcal{X}}_{k-1} = \begin{bmatrix} \boldsymbol{m}_{x,k-1} & \cdots & \boldsymbol{m}_{x,k-1} \end{bmatrix} + \begin{bmatrix} -\sqrt{n}\boldsymbol{S}_{x,k-1} & \sqrt{n}\boldsymbol{S}_{x,k-1} \end{bmatrix} . \tag{5.14}$$

The sigma points are generated using the $2n$ method, such that the resulting size of $\boldsymbol{\mathcal{X}}_{k-1}$ is 6×12. Each i^{th} column of $\boldsymbol{\mathcal{X}}_{k-1}$ represents an individual sigma point, all of which are propagated using the CW2 equations and averaged to obtain the predicted state estimate at time t_k; that is,

$$\mathcal{X}^{(i)}_{k|k-1} = \boldsymbol{f}\left(\mathcal{X}^{(i)}_{k-1}\right) \qquad \text{and} \qquad \boldsymbol{m}_{x,k|k-1} = \frac{1}{2n}\sum_{i=1}^{2n} \mathcal{X}^{(i)}_{k|k-1} . \tag{5.15}$$

The state error covariance information can be extracted from the propagated sigma points. The covariance square-root factor is computed using a QR decomposition of the compound matrix containing the propagated sigma points as

$$\boldsymbol{S}_{x,k|k-1} \leftarrow \text{qr}\left\{ \frac{1}{\sqrt{2n}} \left[\mathcal{X}^{(1)}_{k|k-1} - \boldsymbol{m}_{x,k|k-1} \,\middle|\, \mathcal{X}^{(2)}_{k|k-1} - \boldsymbol{m}_{x,k|k-1} \,\middle|\, \cdots \,\middle|\, \mathcal{X}^{(2n)}_{k|k-1} - \boldsymbol{m}_{x,k|k-1} \right] \right\} , \tag{5.16}$$

which can be written in short form as

$$\boldsymbol{S}_{x,k|k-1} \leftarrow \text{qr}\left\{ \frac{1}{\sqrt{2n}} \left[\boldsymbol{\mathcal{X}}_{k|k-1} - \boldsymbol{m}_{x,k|k-1} \right] \right\} . \tag{5.17}$$

As previously mentioned, Equations (5.14)-(5.17) are applied to each Gaussian component ℓ. Throughout the propagation step, the weights of every Gaussian component are held constant, such that

$$w_{x,k|k-1} = w_{x,k-1}\,.$$

The resulting pdf is a GM of the form

$$p(\boldsymbol{x}_k \mid \boldsymbol{Y}^{k-1}) = \sum_{\ell=1}^{L} w_{x,k|k-1}^{(\ell)} p_g(\boldsymbol{x}_k\,;\, \boldsymbol{m}_{x,k|k-1}^{(\ell)}, \boldsymbol{S}_{x,k|k-1}^{(\ell)} \boldsymbol{S}_{x,k|k-1}^{(\ell)\,T})\,.$$

5.4.2. Corrector. At time t_k, measurements are received in the form of azimuth and elevation angles from both cameras. The agreement of the measurement data with the prior estimate is determined by comparing the predicted measurement $\boldsymbol{m}_{y,k|k-1}$ of each of the L total GM components with the received measurement $\boldsymbol{y}_k$. For every component ℓ, posterior sigma points are generated by propagating the sigma points $\boldsymbol{\mathcal{X}}_{k|k-1}$ through the true nonlinear function

$$\mathcal{Y}_k^{(i)} = \boldsymbol{h}\left(\mathcal{X}_{k|k-1}^{(i)}\right)\,, \tag{5.18}$$

where the definition of $\boldsymbol{h}(\cdot)$ is given in Equation (5.11). The expected measurement is then computed in the same fashion as Equation (5.15) as

$$\boldsymbol{m}_{y,k} = \frac{1}{2n}\sum_{i=1}^{2n} \mathcal{Y}_k^{(i)}\,. \tag{5.19}$$

The observation error covariance is a function of both the prediction/observation agreement and the known sensor noise characteristics, which is represented by the covariance matrix $\boldsymbol{R}_k$. The observation error covariance matrix is computed in

square-root form as

$$\boldsymbol{S}_{y,k} \leftarrow \mathrm{qr}\left\{\left[\frac{1}{\sqrt{2n}}\left(\boldsymbol{\mathcal{Y}}_k - \boldsymbol{m}_{y,k}\right) \quad \sqrt{\boldsymbol{R}_k}\right]\right\}, \tag{5.20}$$

where $\sqrt{\boldsymbol{R}_k}$ represents the square-root factor of $\boldsymbol{R}_k$ such that $\sqrt{\boldsymbol{R}_k}\sqrt{\boldsymbol{R}_k}^T = \boldsymbol{R}_k$. The cross covariance $\boldsymbol{P}_{x,y,k}$ is then found and used to compute the Kalman gain $\boldsymbol{K}_k$ as

$$\boldsymbol{P}_{x,y,k} = \frac{1}{2n}\sum_{i=1}^{2n}\left[\mathcal{X}_{k|k-1}^{(i)} - \boldsymbol{m}_{x,k|k-1}\right]\left[\mathcal{Y}_k^{(i)} - \boldsymbol{m}_{y,k}\right]^T \tag{5.21}$$

$$\boldsymbol{K}_k = \left(\boldsymbol{P}_{x,y,k}{\boldsymbol{S}_{y,k}}^{-T}\right){\boldsymbol{S}_{y,k}}^{-1}. \tag{5.22}$$

Note that the "$^{-T}$" operation represents the transpose of the inverse of a matrix. The *a posteriori* state estimate is simply computed in the same fashion as a standard Kalman filter as

$$\boldsymbol{m}_{x,k} = \boldsymbol{m}_{x,k|k-1} + \boldsymbol{K}_k\left(\boldsymbol{y}_k - \boldsymbol{m}_{y,k}\right). \tag{5.23}$$

The final step in computing the measurement-updated state noise covariance square-root factor is the application of the Cholesky downdate of $\boldsymbol{S}_{x,k|k-1}$ by the update factors $\boldsymbol{U}$, given as

$$\boldsymbol{U} = \boldsymbol{K}_k\boldsymbol{S}_{y,k} \qquad \text{and} \qquad \boldsymbol{S}_{x,k} \leftarrow \mathrm{cholupdate}\left\{\boldsymbol{S}_{x,k|k-1}, \boldsymbol{U}, -1\right\}. \tag{5.24}$$

The Cholesky downdate effectively finds the square-root factor of $\boldsymbol{S}_{x,k|k-1}{\boldsymbol{S}_{x,k|k-1}}^T - \boldsymbol{U}\boldsymbol{U}^T$. Several software routines are available for performing Cholesky factor updates (or downdates), including MATLAB's `cholupdate` and LINPACK's `schdd` routines.

Equations (5.18)-(5.24) are applied to every Gaussian component. The final step of the measurement update is recomputing the weights of the updated Gaussian components based on their agreement with the measurement data. The updated

weight of component ℓ is computed as [49]

$$w_{x,k}^{(\ell)} = \beta_k^{(\ell)} w_{x,k|k-1}^{(\ell)} / \textstyle\sum_{j=1}^{L} \beta_k^{(j)} w_{x,k|k-1}^{(j)} \,,$$

where the weight gain $\beta_k^{(\ell)}$ is computed on the basis of $\boldsymbol{y}_k$ as

$$\beta_k^{(\ell)} = p_g(\boldsymbol{y}_k \,;\, \boldsymbol{m}_{y,k}^{(\ell)}, \boldsymbol{S}_{y,k}^{(\ell)} \boldsymbol{S}_{y,k}^{(\ell)\,T}) \,.$$

The conditional pdf of $\boldsymbol{x}_k$, given all of the measurement information up to and including t_k, is then given by the Gaussian sum

$$p(\boldsymbol{x}_k \,|\, \boldsymbol{Y}^k) = \sum_{\ell=1}^{L} w_{x,k}^{(\ell)} p_g(\boldsymbol{x}_k \,;\, \boldsymbol{m}_{x,k}^{(\ell)}, \boldsymbol{S}_{x,k}^{(\ell)} \boldsymbol{S}_{x,k}^{(\ell)\,T}) \,.$$

As with any GM filter, it is usually advantageous to prune low-probability components from the mixture to reduce computational cost. A straightforward approach to pruning is to choose some threshold level c and remove any component ℓ where $w_x^{(\ell)} < c$. If any components are pruned, the weights of the mixture must be normalized to satisfy $\sum_{\ell=1}^{L} w_x^{(\ell)} = 1$ so that the integral of the pdf over its support is equal to one. A block diagram representation of the complete IROD and filter algorithm is shown in Figure 5.5.

5.5. SIMULATION

The IROD algorithm and accompanying GMSRUKF are simulated for a typical sensor suite and low Earth orbit two-satellite formation. The inspector spacecraft is equipped with two identical cameras with 20° horizontal and vertical fields of view. The angular measurements are corrupted with white noise with standard deviations of $\sigma_\theta = \sigma_\phi = 67\,[\text{arcsec}]$, which corresponds to a 1-pixel error in a 1080×1080 pixel focal plane array. Assuming that the inspector maintains a fixed attitude with respect

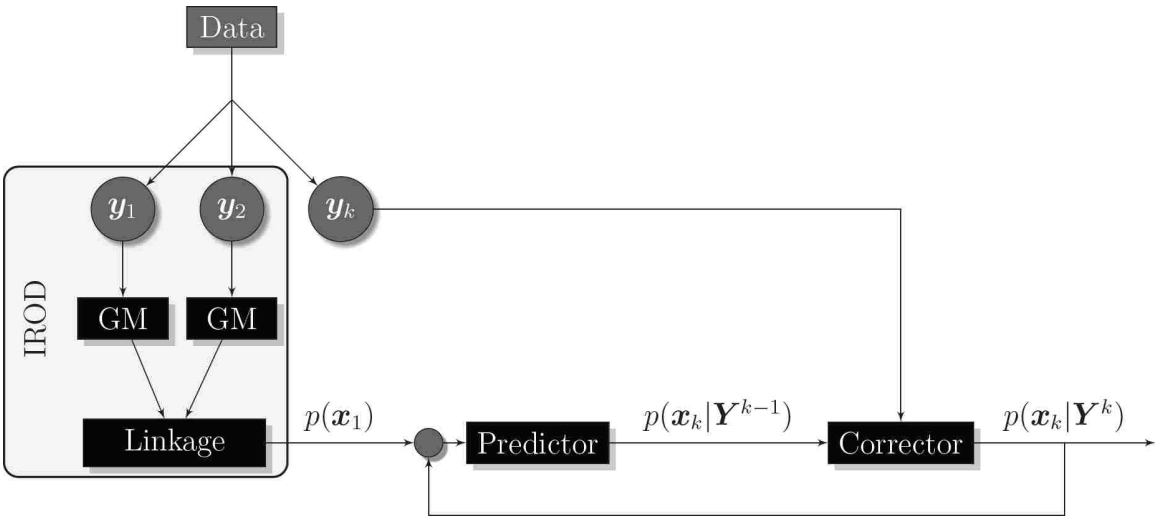

Figure 5.5. Block representation of the GM pdf construction and refinement algorithm.

to the Hill frame, the cameras are modeled at constant positions, taken as

$$\boldsymbol{d}_{\mathrm{c1},k} = \boldsymbol{d}_{\mathrm{c1}} = [1,\, 0,\, 0]^T \text{ [m]} \qquad \text{and} \qquad \boldsymbol{d}_{\mathrm{c2},k} = \boldsymbol{d}_{\mathrm{c2}} = [-1,\, 0,\, 0]^T \text{ [m]}\,,$$

consistent with a scale corresponding to a microsatellite. The inspector spacecraft is simulated in a circular orbit of 400 [km] altitude with inclination $i = 30°$, argument of periapsis $\overline{\omega} = 20°$, right ascension of the ascending node $\Omega = 50°$, and mean anomaly $M = 210°$. The target satellite is initialized at epoch t_0 with the relative position and velocity

$$\delta\mathbf{r}_0 = [0, 150, -15]^T \text{ [m]} \qquad \text{and} \qquad \delta\dot{\mathbf{r}}_0 = [-0.01414,\, 0.00005,\, 0.01000]^{\mathrm{T}} \text{ [m/s]}\,.$$

The inspector and target satellites' true inertial motions are propagated with two-body dynamics for six hours, and the relative trajectory is shown in Figure 5.6.

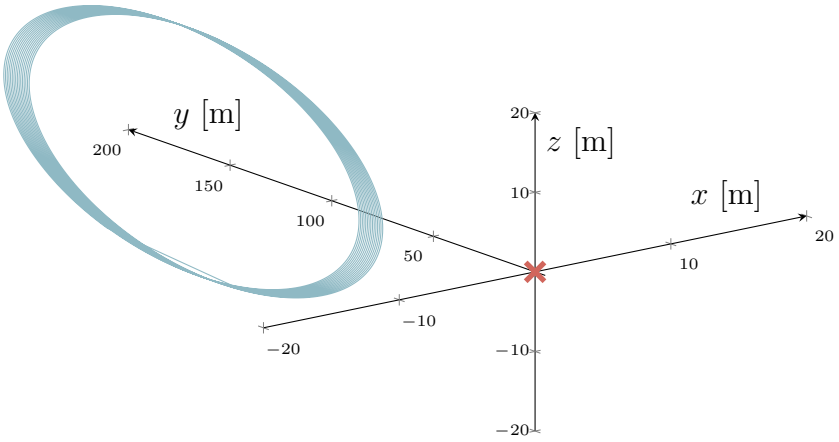

Figure 5.6. True relative motion of target in Hill frame using two-body dynamics. The inspector position is denoted by the cross marker.

In the simulated linkage process, ten minutes is used between the first and second measurements, with the first measurement taken approximately one hour after the epoch, such that $t_1 = 3350\,[\mathrm{s}]$ and $t_2 = 3950\,[\mathrm{s}]$. When computing the GM approximation to the uniform range uncertainty, the tolerance $\sigma_{\rho,\max}$ is used to control the resolution of the GM approximation. For this test case, this tolerance is taken to be $\sigma_{\rho,\max} = 1\,[\mathrm{m}]$. The components generated at t_1 and t_2 are then processed via the linkage algorithm (see Section 5.3) to produce the Cartesian pdf in position and velocity (Figure 5.7). In general, for the linkage and Gaussian mixture construction, a larger spacing between measurements, that is, a larger $(t_2 - t_1)$, produces an IROD solution that is more tightly concentrated about the true solution; that is, it has less uncertainty. One exception to this trend occurs when the linkage time is close to an integer multiple of the inspector's orbital half-period. This phenomenon is discussed further later in this section.

Measurements are processed at $1\,[\mathrm{Hz}]$ and are occluded when the target is in shadow or when the Sun is in either of the cameras' fields of view. At each step, the first and second central moments of the posterior pdf are computed to give a conditional mean and covariance matrix. From the conditional covariance,

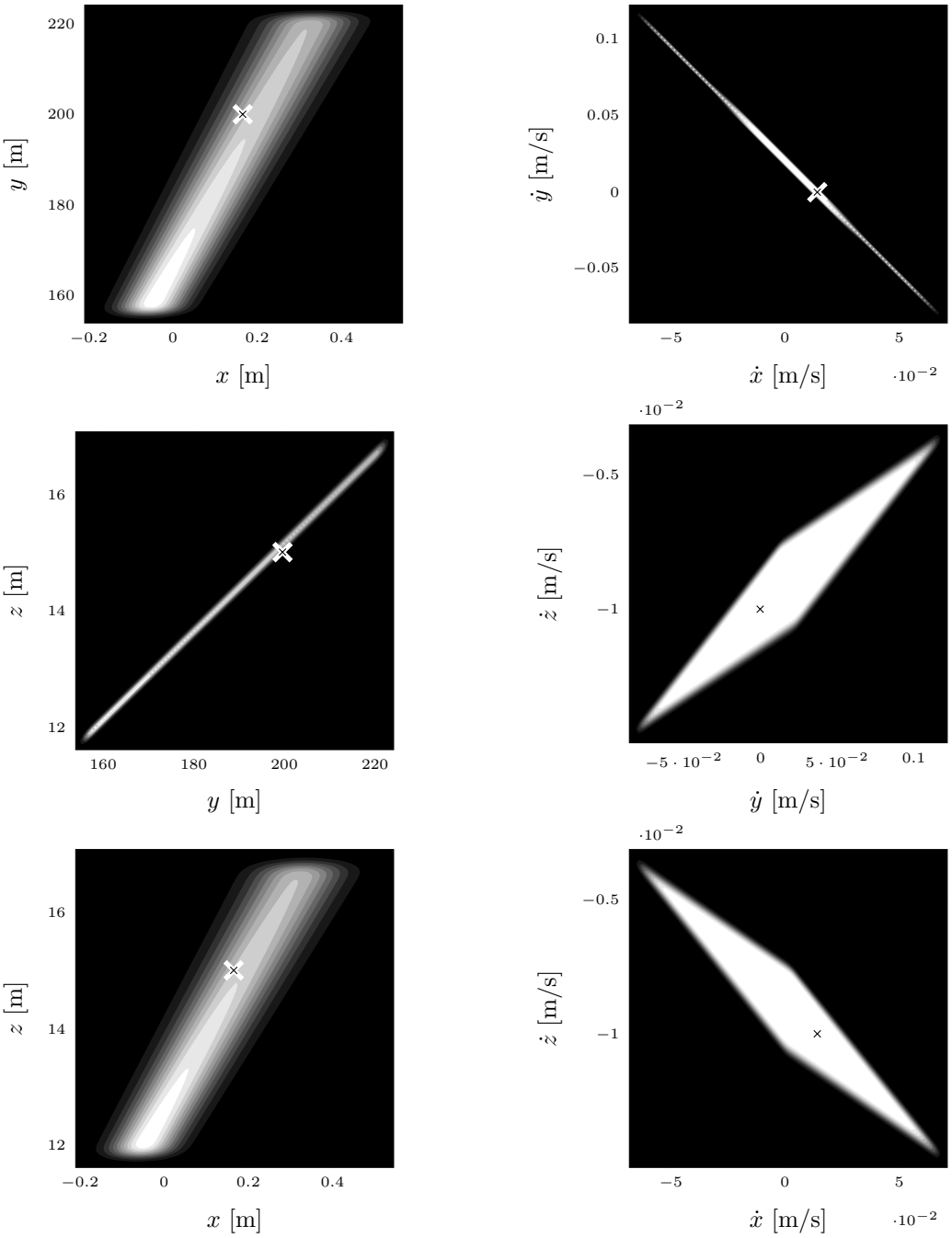

Figure 5.7. Position and velocity pdfs at $t_1 = 3350\,[\mathrm{s}]$. The truth is denoted by the cross markers.

the position root sum square (RSS) and velocity RSS are extracted. These RSS values for each measurement are collected over 1000 Monte Carlo runs with different random measurement data and a constant truth model. In addition to the relative position and velocity RSS, the relative position and velocity tracking errors and their averages (over the 1000 runs) are computed. Figures 5.8a and 5.8b illustrate 100 time histories of the position and velocity RSS, where the 100 runs are randomly selected from the set of 1000 Monte Carlo runs. Similarly, the position and velocity

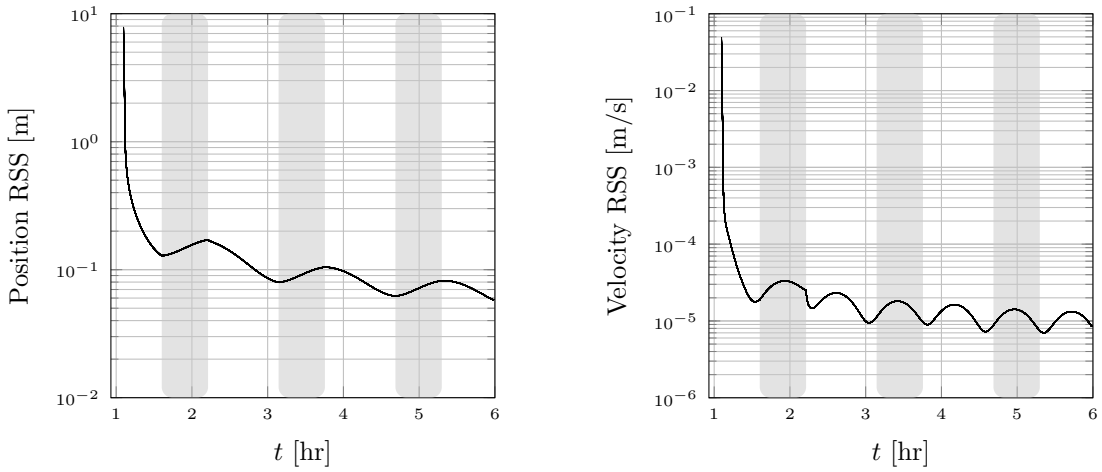

(a) Position RSS.

(b) Velocity RSS.

Figure 5.8. Overlaid position and velocity RSS over 100 runs of same orbit. Although indistinguishable to the naked eye, the RSS values vary slightly from run to run.

tracking errors (for the 100 runs) are illustrated in Figure 5.9, and the average tracking error (using all 1000 runs) is shown on top of the individual tracking errors. As evident in Figures 5.8-5.9, the estimation error and uncertainty decrease drastically during the first hour of measurements. After the first hour, the solution accuracy is continuously improved, but is more heavily dominated by the periodic nature of the dynamics, as suggested by the sinusoidal behavior of the RSS and tracking errors. In the worst-case run of the 1000 Monte Carlo runs, the filter achieves relative position

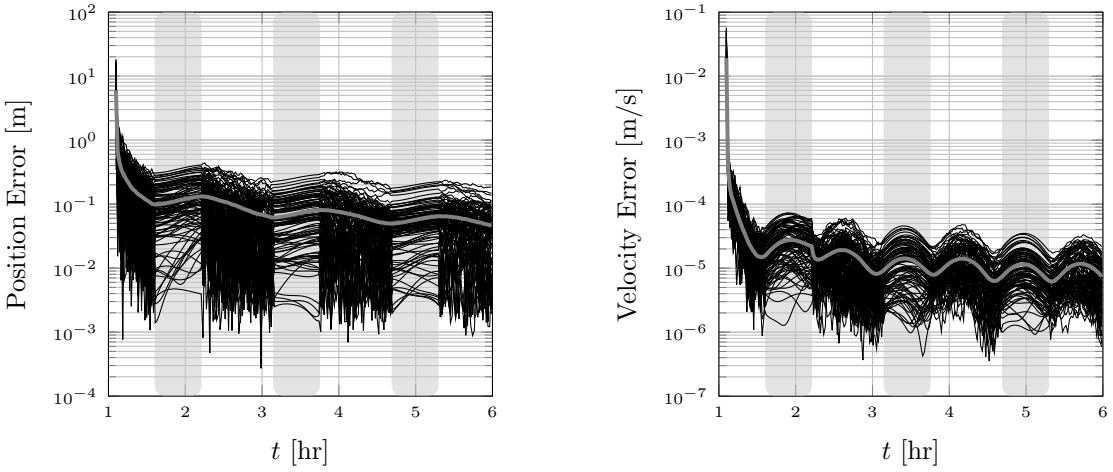

(a) Position error.

(b) Velocity error.

Figure 5.9. Overlaid position and velocity error over 100 runs of same orbit. The gray line denotes the average error.

and velocity tracking errors as low as 10 [cm] and 10 [μm/s], respectively. In the best case, accuracies of 1 [mm] and 1 [μm/s] are realized.

Additionally, the relationship between the camera baseline distance to the algorithm performance is investigated. The camera baseline is varied from 1 [m] to 8 [m], and the position RSS is averaged over 25 measurement sets for each baseline value (Figure 5.10a). As shown, a linear decrease in RSS is observed with increased baseline separations. For example, in general, doubling the camera separation results in estimates that are twice as accurate.

In real-world mission operations, some parameters, such as the initial separation distance between the target and inspector, cannot easily be controlled, whereas the time allowed between processing the first and second angular measurements can be chosen by the mission designer. In order to better understand the relationship between the initial GM approximation and these parameters, namely the initial along-track separation y_0 and linkage time $(t_2 - t_1)$, pdfs are generated for a survey of initial conditions. The initial along-track separation is varied from $15 \leq y_0 \leq 150$ [m] and

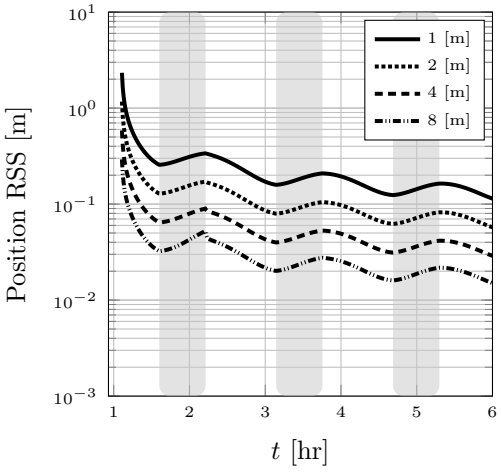

(a) Average position RSS as a function of camera baseline.

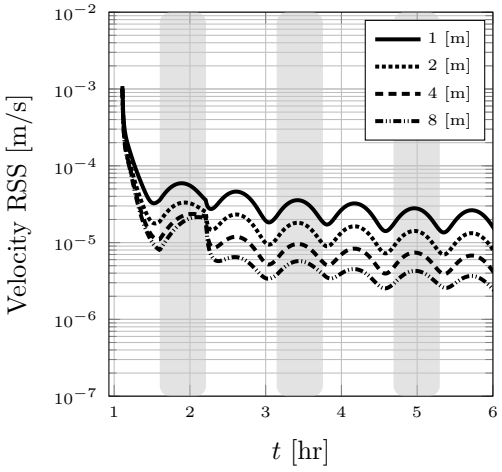

(b) Average velocity RSS as a function of camera baseline.

Figure 5.10. Camera baseline study: average position and velocity uncertainty.

the linkage time from $1 \leq (t_2 - t_1) \leq 90\,[\text{min}]$. In this study, the first measurements are taken at the epoch t_0, such that $\delta\mathbf{r}_1 = \delta\mathbf{r}_0$ and $\delta\dot{\mathbf{r}}_1 = \delta\dot{\mathbf{r}}_0$. For each combination, three metrics are used to assess the approximation: the total number of Gaussian components generated (Figure 5.11), the position and velocity RSS (Figure 5.13), which is computed from the conditional covariance, and the Shannon entropy of the position and velocity pdfs (Figure 5.14), which is defined for a general pdf as

$$H_s \triangleq -\int p(\boldsymbol{x}) \log p(\boldsymbol{x}) d\boldsymbol{x}\,. \tag{5.25}$$

In this particular study, the LOS measurements are left uncorrupted in order to maintain consistency between the runs.

As shown in Figure 5.11, the driving factor of the component generation is the orbital geometry, namely $y(t_2)$. The number of components generated increases as $y(t_2)$ grows because as the relative range approaches very large values, the LOS vectors become equivalent. As the LOS vectors approach equivalence, the distance

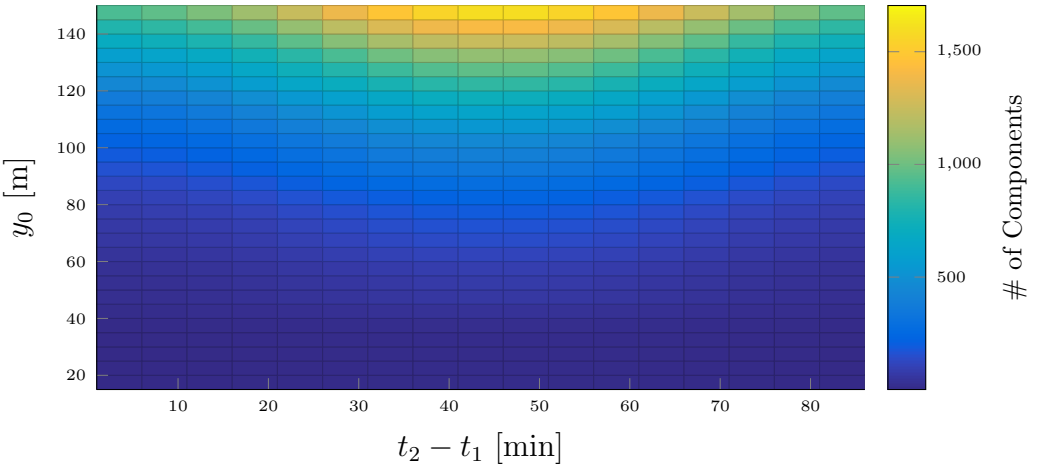

Figure 5.11. Number of initial components generated as a function of linkage Δt and along-track separation.

between $\rho_{\min}$ and $\rho_{\max}$ grows larger, requiring more components to achieve the same GM resolution of $\sigma_{\rho,\max}$, as illustrated in Figure 5.12.

The dependence of uncertainty on initial along-track separation and linkage time is explored by first examining the effects on the relative position and velocity pdfs' second moments, which are captured by the RSS extracted from the conditional covariances. As shown in Figure 5.13a, the relative position RSS is dominated by the initial along-track separation, exhibiting a nearly linear dependence of y_0.

The relative velocity RSS (Figure 5.13b) behaves much differently, exhibiting two trends not seen in the relative position RSS. First, the relative velocity RSS grows exponentially with linkage times close to the reference orbit's half-period. These travel times correspond to near-180° transfers, where an infinite number of initial relative velocity solutions satisfy the given relative position vectors and elapsed time.

A similar phenomenon is observed in the traditional Lambert problem, as well as in a relative motion cylindrical coordinate formulation given in Reference [56]. Second, with the exception of these RSS values near the half-period, a general trend of decreasing relative velocity RSS with increasing travel times is shown. This second

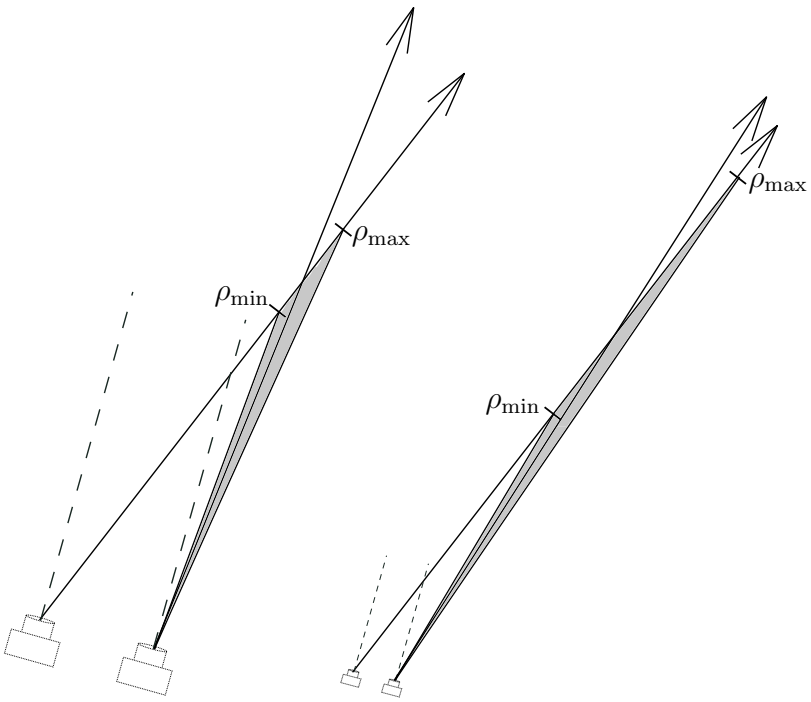

Figure 5.12. For very large initial relative ranges, the LOS vectors approach equivalence, requiring more components in the construction.

trend suggests that measurements taken farther apart result in higher confidences in the IROD solution; that is, less uncertainty in the initial estimate.

Because the pdfs generated from the IROD are non-Gaussian, the Shannon entropy of each of the linkage solutions is computed to analyze the uncertainty information not previously represented in the RSS analysis. Similar to what is shown in the relative position RSS analysis, the relative position entropy exhibits no apparent dependence to linkage time (Figure 5.14a).

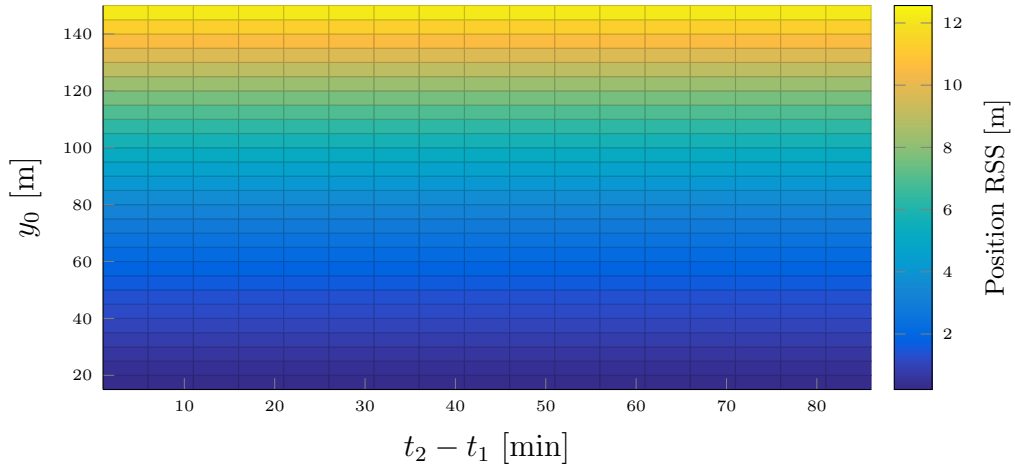

(a) RSS of initial position pdf.

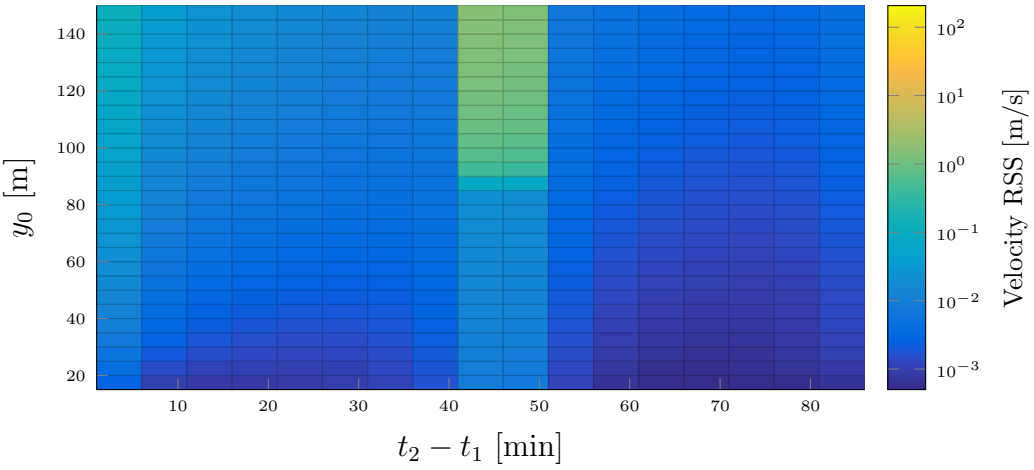

(b) RSS of initial velocity pdf.

Figure 5.13. RSS of initial pdf as a function of linkage Δt and along-track separation.

However, contrary to the approximately-linear dependence of the relative position RSS to the initial along-track separation, the relationship exhibited between the relative position pdf entropy and y_0 is logarithmic. The difference between these two trends implies that the relative position pdf's higher-order moments and correlations quickly become more dominant as the initial along-track separation is increased. The initial velocity entropy response map shown in Figure 5.14b is a powerful result of the linkage analysis, as it captures the majority of the linkage trends described thus far.

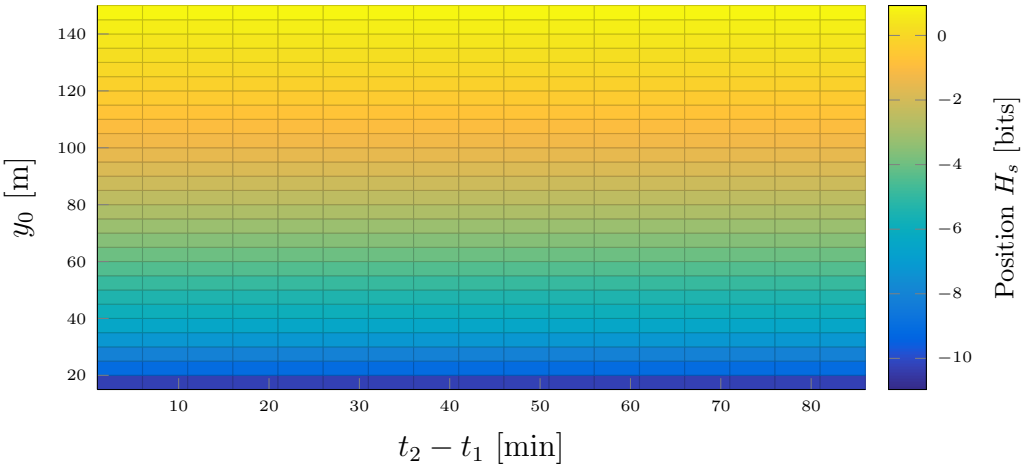

(a) Shannon entropy of position pdf.

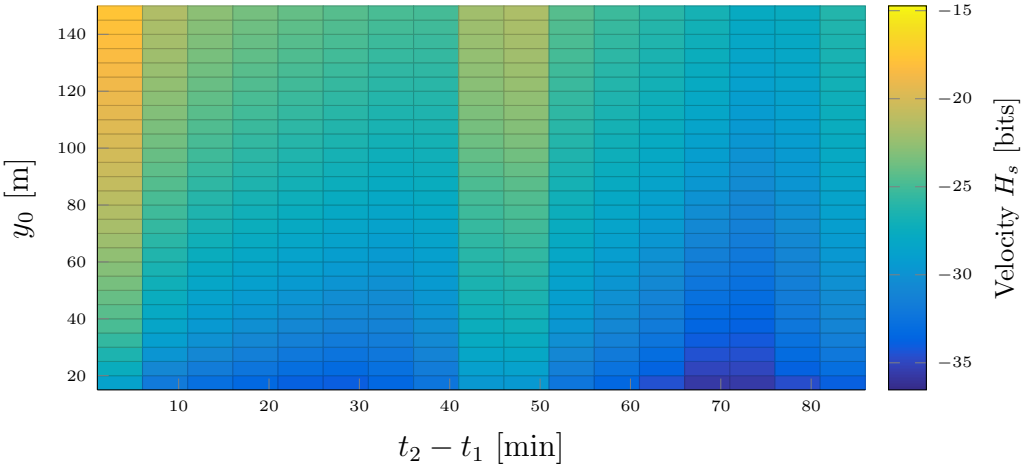

(b) Shannon entropy of velocity pdf.

Figure 5.14. Shannon entropy, H_s, of initial pdf as a function of linkage Δt and along-track separation.

This response exhibits a similar logarithmic dependence to initial along-track separation as in Figure 5.14a, a general decrease in relative velocity uncertainty with longer linkage times, as observed in Figure 5.13b, as well as a sharp increase in uncertainty at linkage times near the half-period. Because it captures multiple trends, from an operational standpoint, Figure 5.14b can serve as an effective tool for selecting more effective measurements in the IROD process.

6. MULTITARGET TRACKING

The growing population of space objects in Earth orbit and, in particular, the subset of objects belonging to densely populated constellations, furthers the demand for the development and deployment of more sophisticated tracking algorithms. Examples of these dense constellations include debris clouds from satellite breakups or collisions [57], as well as controlled satellite swarms, which have been recently proposed as a means to provide broadband Internet across the globe [3], among numerous other applications. The ability to track and catalog these objects from the ground using optical-telescopes and/or RADAR is a well-studied problem [5–8]. Many of the approaches to the ground-based multitarget tracking problem involve some form of hypothesis formulation and data association [58]. These techniques, such as multiple hypothesis tracking (MHT), suffer from time-exponential computational complexity increases due to the required data association and consequently rely on heuristic reduction methods to achieve tractability [59].

Newer methods, based on moment approximations of the multitarget Bayes filter, have shown promise as more computationally tractable and statistically-consistent approaches to ground-based multitarget tracking [60, 61], as they mitigate the need for explicit data association. Two such methods, referred to as the probability hypothesis density (PHD) and cardinalized probability hypothesis density (CPHD) filters, approximate the full multitarget Bayes filter by propagating the posterior intensity function, which is the first-order moment of the full multitarget pdf. The CPHD filter additionally propagates the posterior target cardinality probability mass function (pmf) [62]. Although the inclusion of cardinality statistics increases the complexity of the filter, it has been shown to dramatically improve cardinality estimates *and* state estimates [63].

In this chapter, the CPHD filter is employed to serve as a means to track multiple targets in close proximity of an inspector satellite. The ability to autonomously track multiple targets in neighboring orbits using angles from video data could enable a new class of proximity operations in which cooperation between vehicles is not possible, or simply serve as a means to monitor the surrounding area in an effort to mitigate collision risks.

This chapter considers an inspector satellite system with a stereo imaging sensor that provides angular measurements of multiple nearby targets from two different optical viewpoints. These stereo measurements, when available, are processed in a CPHD filter to recursively and statistically estimate the number of nearby targets, as well as their relative positions and velocities with respect to the inspector satellite. The primary purpose of this work is to establish the fundamental modeling considerations and challenges unique to angles-only space-based relative multitarget tracking. Special consideration is given to the birth model, which is responsible for incorporating previously untracked targets into the multitarget intensity when they appear. The performance of the presented framework is evaluated in a simulation of a chaotic debris cloud tracking problem. Preliminary results are published in Reference [64]. The current work is a more comprehensive study with stronger results.

In an effort to prevent detraction from the multitarget focus of this chapter, simplifications are made with respect to the presented single target tracking framework. First, the linear CW dynamics are used in place of the higher-order CW2 dynamics. Naturally, the CW relative Lambert solution (Section 3.1) is used in place of the CW2 relative Lambert solution (Section 3.2). Lastly, only planar motion is considered to simplify the analysis. With this, the general system is given as

$$\boldsymbol{x}_k = \boldsymbol{F}_{k-1}\boldsymbol{x}_{k-1} + \boldsymbol{w}_{k-1} \qquad \text{and} \qquad \boldsymbol{y}_k = \boldsymbol{h}(\boldsymbol{x}_k) + \boldsymbol{\nu}_k \,,$$

where $\boldsymbol{F}_{k-1}$ and $\boldsymbol{h}(\cdot)$ are planar simplifications of Equations (3.2) and (5.11), respectively. The process noise $\boldsymbol{w}_{k-1}$ and measurement noise $\boldsymbol{\nu}_k$ are taken to be Gaussian and white with $\boldsymbol{Q}_{k-1} = E\{\boldsymbol{w}_{k-1}\boldsymbol{w}_{k-1}^T\}$ and $\boldsymbol{R}_k = E\{\boldsymbol{\nu}_k\boldsymbol{\nu}_k^T\}$.

6.1. THE CARDINALIZED PROBABILITY HYPOTHESIS DENSITY FILTER

At time t_k, there are $N(k)$ targets with states $\boldsymbol{x}_{k,1}, \boldsymbol{x}_{k,2}, \ldots, \boldsymbol{x}_{k,N(k)}$. The multitarget state $\boldsymbol{X}_k \in \mathcal{X}$ is composed of all of the target states, in no specified order, such that

$$\boldsymbol{X}_k = \left\{\boldsymbol{x}_{k,1}, \boldsymbol{x}_{k,2}, \ldots, \boldsymbol{x}_{k,N(k)}\right\} .$$

The multitarget state $\boldsymbol{X}_k$ is taken as a random finite set (RFS) and is expressed in the multitarget domain $\mathcal{X}$ (note to be confused with sigma points $\boldsymbol{\mathcal{X}}$). Reference [65] defines the RFS as a random variable that takes values as unordered finite sets, wherein the number of constituent points is random and the points themselves are random. Propagation of the multitarget pdf, which is expressed in the multitarget space $\mathcal{F}(\mathcal{X})$, is generally intractable [66]. Tractable recursions can be achieved by propagating the first-moment approximation of the multitarget pdf, which is known as the intensity or PHD and exists in the single-target space.

In some situations, such as when the number of targets is large, the PHD filter can produce poor estimates of target cardinality (number of targets) [63]. This is due to the fundamental assumption of the PHD filter: the target cardinality is a Poisson random variable. Recall that for a Poisson distribution, the variance is equal to the mean, as illustrated in Figure 6.1. It is clear from Figure 6.1 that as the estimated number of targets becomes large, so too does the variance of the estimate. Thus, for many applications, including multitarget satellite relative navigation, in which accurate target number knowledge is critical to spatial awareness, the errors induced

by the Poisson approximation of the cardinality distribution may be unacceptable, especially when the number of targets is high. In such situations, the CPHD filter often offers significant improvements in performance over the PHD filter by jointly propagating the target intensity $v_{k|k}$ and target cardinality distribution $p_{k|k}$.

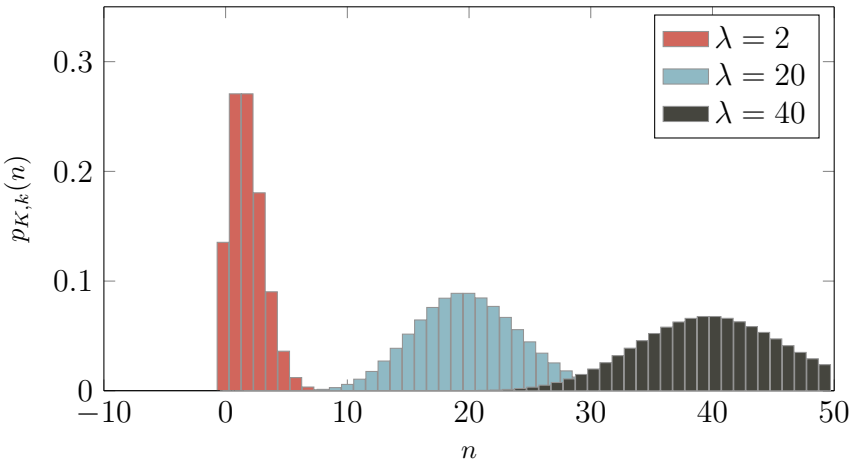

Figure 6.1. Due to the PHD filter's Poisson approximation of target cardinality, higher target numbers result in higher cardinality variance.

The CPHD filter is similar to the PHD filter in that it propagates the posterior intensity function at time t_{k-1} to time t_k as [63]

$$v_{k|k-1}(\boldsymbol{x}) = \int p_{S,k}(\boldsymbol{\xi}) f_{k|k-1}(\boldsymbol{x}|\boldsymbol{\xi}) v_{k-1}(\boldsymbol{\xi}) d\boldsymbol{\xi} + \gamma_k(\boldsymbol{x}) \,,$$

where $f_{k|k-1}(\cdot|\boldsymbol{\xi})$ is the single-target transition density at time t_k conditioned on previous state $\boldsymbol{\xi}$, $p_{S,k}(\boldsymbol{\xi})$ is the state-dependent probability of target survival, and $\gamma_k(\boldsymbol{x})$ is the intensity of spontaneous births at time t_k. A key difference between the PHD filter and the CPHD filter is that the CPHD filter additionally propagates the discrete

cardinality distribution as [63]

$$p_{k|k-1}(n) = \sum_{j=0}^{n} p_{\Gamma,k}(n-j)\Pi_{k|k-1}[v_{k-1}, p_{k-1}](j)\,, \tag{6.1}$$

where $p_{\Gamma,k}(\cdot)$ is the cardinality pmf of target births, and

$$\Pi_{k|k-1}[v,p](j) = \sum_{\ell=j}^{\infty} C_j^{\ell} \frac{\langle p_{S,k}, v\rangle^j \left\langle 1 - p_{S,k}, v\right\rangle^{\ell-j}}{\langle 1, v\rangle^{\ell}}\,. \tag{6.2}$$

Here, C_j^{ℓ} denotes the binomial coefficient, which is defined as

$$C_j^{\ell} \triangleq \frac{\ell!}{j!(\ell-j)!}\,.$$

The operator $\langle\cdot,\cdot\rangle$ denotes the inner product, which is defined between α and β as

$$\langle \alpha, \beta\rangle \triangleq \int \alpha(x)\beta(x)dx \qquad \text{and} \qquad \langle \alpha, \beta\rangle \triangleq \sum_{\ell=0}^{\infty} \alpha(\ell)\beta(\ell)$$

in the cases that α and β are scalar real-valued functions or real-valued sequences, respectively.

Recall the general form of a discrete binomial distribution,

$$b(x; n, p) = \binom{n}{x} p^x (1-p)^{n-x} \tag{6.3}$$

which gives the probability that from n trials there will be exactly x successes, given that the individual trial probability of success is p. Equation (6.2) is of the same form; the summation argument is simply the probability that exactly j of ℓ targets survive given the probability of survival $p_{S,k}$ conditioned upon the intensity v. Note that because the multitarget state has no specific ordering, the ℓ choose j different ways in which targets can survive or die is accounted for by the binomial coefficient that appears in Equation (6.2).

The cardinality distribution is represented by a pmf over the variable n. The variable n represents a discrete cardinality hypothesis; that is,

$$p_{k|k-1}(n) = \Pr(N(k) = n)\,.$$

Note that the target cardinality distribution (Eq. (6.1)) is technically infinitely tailed. In practice, however, the pmf can be reasonably truncated at some chosen limit $n_{\max}$ without noticeable loss of information. In essence, the cardinality pmf is propagated according to the target birth cardinality pmf $p_{\Gamma,k}$ and existing target survival probability $\Pi_{k|k-1}$.

At time t_k, a new measurement set $\tilde{\boldsymbol{Y}}_k$ is made available. For reasons discussed later in this chapter, the measurements corresponding to birth targets are denoted as $\boldsymbol{Y}_{\text{birth},k}$ and are handled separately. All other measurements, including both non-

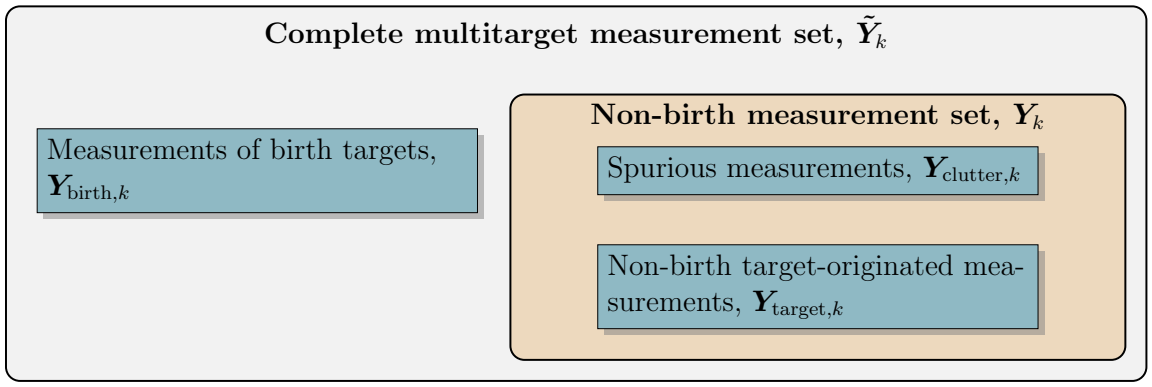

Figure 6.2. Block representation of the multitarget measurement structure.

birth target-originated measurements and clutter, belong to the unordered set $\boldsymbol{Y}_k$, as illustrated in Figure 6.2. When the (non-birth) multitarget measurement $\boldsymbol{Y}_k$ is received, the cardinality distribution and intensity function are updated according

to [67]

$$p_k(n) = \frac{\Upsilon_k^0[v_{k|k-1}, \boldsymbol{Y}_k](n) p_{k|k-1}(n)}{\left\langle \Upsilon_k^0[v_{k|k-1}, \boldsymbol{Y}_k], p_{k|k-1} \right\rangle} \qquad \text{and} \tag{6.4}$$

$$v_k(\boldsymbol{x}) = \frac{\left\langle \Upsilon_k^1[v_{k|k-1}, \boldsymbol{Y}_k], p_{k|k-1} \right\rangle}{\left\langle \Upsilon_k^0[v_{k|k-1}, \boldsymbol{Y}_k], p_{k|k-1} \right\rangle} [1 - p_{D,k}(\boldsymbol{x})] v_{k|k-1}(\boldsymbol{x}) \tag{6.5}$$

$$+ \sum_{\boldsymbol{y} \in \boldsymbol{Y}_k} \frac{\left\langle \Upsilon_k^1[v_{k|k-1}, \boldsymbol{Y}_k \backslash \{\boldsymbol{y}\}], p_{k|k-1} \right\rangle}{\left\langle \Upsilon_k^0[v_{k|k-1}, \boldsymbol{Y}_k], p_{k|k-1} \right\rangle} \psi_{k,y}(\boldsymbol{x}) v_{k|k-1}(\boldsymbol{x}) \,, \quad \text{where} \tag{6.6}$$

$$\Upsilon_k^u[v, \boldsymbol{Y}](n) \triangleq \sum_{j=0}^{\min(|\boldsymbol{Y}|, n)} (|\boldsymbol{Y}| - j)! p_{K,k}(|\boldsymbol{Y}| - j) P_{j+u}^n \frac{\langle 1 - p_{D,k}, v \rangle^{n-(j+u)}}{\langle 1, v \rangle^n} e_j \left(\Xi(v, \boldsymbol{Y}) \right) \,, \tag{6.7}$$

$$\psi_{k,y}(\boldsymbol{x}) \triangleq \frac{\langle 1, \kappa_k \rangle}{\kappa_k(\boldsymbol{y})} g_k(\boldsymbol{y}|\boldsymbol{x}) p_{D,k}(\boldsymbol{x}) \,, \qquad \text{and} \tag{6.8}$$

$$\Xi(v, \boldsymbol{Y}) \triangleq \{ \langle v, \psi_{k,y} \rangle : \boldsymbol{y} \in \boldsymbol{Y} \} \,. \tag{6.9}$$

The distribution $\Upsilon_k^u[v, \boldsymbol{Y}](n)$ describes the likelihood of the multitarget observation $\boldsymbol{Y}$ given that there are n targets. The function $g_k(\cdot|\boldsymbol{x})$ is the single-target measurement likelihood at time t_k given current state $\boldsymbol{x}$, $p_{D,k}(\boldsymbol{x})$ is the state-dependent probability of target detection at time t_k given current state $\boldsymbol{x}$, $\kappa_k(\cdot)$ is the intensity of clutter measurements at time t_k, and $p_{K,k}(\cdot)$ is the cardinality distribution of clutter at time t_k. The term $\boldsymbol{Y}_k \setminus \{\boldsymbol{y}\}$ denotes the set subtraction of $\{\boldsymbol{y}\}$ from $\boldsymbol{Y}_k$, and P_j^n represents the permutation coefficient, defined as

$$P_j^n \triangleq \begin{cases} \dfrac{n!}{(n-j)!} & , \quad n \geq j \\ 0 & , \quad n < j \end{cases} \,.$$

The j^{th}-order elementary symmetric function $e_j(\cdot)$ is defined as

$$e_j(\boldsymbol{\mathcal{Z}}) \triangleq \sum_{\boldsymbol{S} \subseteq \boldsymbol{\mathcal{Z}}, |\boldsymbol{S}| = j} \left(\prod_{\zeta \in \boldsymbol{S}} \zeta \right) \tag{6.10}$$

for a real finite set $\boldsymbol{\mathcal{Z}}$. An efficient method for the calculation of Equation (6.10) is described in Reference [63]. The elementary symmetric polynomials can be alternatively defined in n variables $X_1, \ldots, X_n$ as

$$\begin{aligned}
e_0(X_1, X_2, \ldots, X_n) &= 1 \\
e_1(X_1, X_2, \ldots, X_n) &= \sum_{1 \le j \le n} X_j \\
e_2(X_1, X_2, \ldots, X_n) &= \sum_{1 \le j < k \le n} X_j X_k \\
e_3(X_1, X_2, \ldots, X_n) &= \sum_{1 \le j < k < l \le n} X_j X_k X_l \\
&\vdots \\
e_n(X_1, X_2, \ldots, X_n) &= X_1 X_2 \ldots X_n
\end{aligned}$$

In order to better understand the form of the elementary symmetric function, consider the simple example of receiving three measurements $\boldsymbol{Y} = \{\boldsymbol{y}_1, \boldsymbol{y}_2, \boldsymbol{y}_3\}$. From Equation (6.9), it follows that

$$\Xi(v, \boldsymbol{Y}) = \{< v, \psi_{k,y_1} >, < v, \psi_{k,y_2} >, < v, \psi_{k,y_3} >\} \, .$$

Thus, in this example, there are four possible elementary functions, given by

$$\begin{aligned}
e_0(\Xi(v, \boldsymbol{Y})) &= 1 \, , \\
e_1(\Xi(v, \boldsymbol{Y})) &= < v, \psi_{k,y_1} > + < v, \psi_{k,y_2} > + < v, \psi_{k,y_3} > , \\
e_2(\Xi(v, \boldsymbol{Y})) &= < v, \psi_{k,y_1} >< v, \psi_{k,y_2} > + < v, \psi_{k,y_1} >< v, \psi_{k,y_3} > \\
&\qquad + < v, \psi_{k,y_2} >< v, \psi_{k,y_3} > , \qquad \text{and} \\
e_3(\Xi(v, \boldsymbol{Y})) &= < v, \psi_{k,y_1} >< v, \psi_{k,y_2} >< v, \psi_{k,y_3} > \, .
\end{aligned}$$

Equation (6.7) is certainly nonintuitive, and so a more thorough examination of its various terms is provided in Table 6.1. The CPHD recursion admits both

sequential Monte Carlo [66] and GM [63] implementations, the latter of which is discussed in this thesis.

Table 6.1. Explanation of $\Upsilon_k^u[v, \boldsymbol{Y}](n)$, the likelihood of the multitarget observation $\boldsymbol{Y}$ given that there are n targets.

Term	Description
j	hypothesis of the number of non-clutter measurements
$\lvert\boldsymbol{Y}\rvert$	number of measurements received
$(\lvert\boldsymbol{Y}\rvert - j)!$	number of ways that clutter measurements can be ordered
$p_{K,k}(\lvert\boldsymbol{Y}\rvert - j)$	probability that $\lvert\boldsymbol{Y}\rvert - j$ of the measurements are clutter
P_{j+u}^n	number of ways $j+u$ targets can be selected from n targets, where order matters
$\dfrac{\langle 1 - p_{D,k}, v\rangle^{n-(j+u)}}{\langle 1, v\rangle^n}$	probability that $n-(j+u)$ targets are not detected
$\psi_{k,y}(\boldsymbol{x})$	conditional probability distribution of $\boldsymbol{x}$ given a measurement and the known detection and clutter distributions
$\Xi(v, \boldsymbol{Y})$	set of duplicate intensities conditioned upon each different measurement
$e_j\left(\Xi(v, \boldsymbol{Y})\right)$	summation of all possible j-wise products of conditional intensities

6.2. THE GAUSSIAN MIXTURE EXTENDED KALMAN CPHD

In the case of linear Gaussian dynamics and measurements, the CPHD recursion admits a closed-form solution when the posterior intensity is modeled by a GM. The closed-form recursion for linear Gaussian models can be extended to accommodate nonlinear dynamics and measurements via linearization of the transition density and measurement likelihood functions in the same fashion as the single-target

extended Kalman filter (EKF) [49, 68]. Because only linear dynamics are considered in this work, local linearizations are needed in the measurement update, only.

It is assumed that the posterior intensity at t_{k-1} is given in the form of a GM as

$$v_{k-1}(\boldsymbol{x}) = \sum_{i=1}^{J_{k-1}} w_{k-1}^{(i)} p_g(\boldsymbol{x}\,;\, \boldsymbol{m}_{k-1}^{(i)}, \boldsymbol{P}_{k-1}^{(i)})\,,$$

where J_{k-1} is the total number of Gaussian components at t_{k-1}, and $\boldsymbol{m}_{k-1}^{(i)}$, $\boldsymbol{P}_{k-1}^{(i)}$, and $w_{k-1}^{(i)}$ are the mean, covariance, and weight, respectively, of the i^{th} component. Recall that for single-target GM filtering, the property $\sum_{i=1}^{J_{k-1}} w_{k-1}^{(i)} = 1$ is enforced to ensure that the pdf integrates to one. No such requirement exists for multitarget filtering; in fact, the sum of the weights can be used to estimate the number of targets as $\hat{N}(k) \approx \sum_{i=1}^{J_{k-1}} w_{k-1}^{(i)}$.

It follows from [63] that the predicted target cardinality and intensity at t_k are given as

$$p_{k|k-1}(n) = \sum_{j=0}^{n} p_{\Gamma,k}(n-j) \sum_{\ell=j}^{\infty} C_j^{\ell} p_{k-1}(\ell) p_{S,k}^{j} (1-p_{S,k})^{\ell-j} \tag{6.11}$$

$$\text{and} \qquad v_{k|k-1}(\boldsymbol{x}) = v_{S,k|k-1}(\boldsymbol{x}) + \gamma_k(\boldsymbol{x})\,. \tag{6.12}$$

The first term in Equation (6.11) accounts for the change in cardinality due to spontaneous births, and the remaining terms account for the existing targets' survival probability. Recall that the pmf is infinitely tailed. In practice, the pmf must be truncated after an appropriate number of bins $n_{\max}$ such that

$$p_{k|k-1}(n) = \sum_{j=0}^{n} p_{\Gamma,k}(n-j) \sum_{\ell=j}^{n_{\max}} C_j^{\ell} p_{k-1}(\ell) p_{S,k}^{j} (1-p_{S,k})^{\ell-j}\,. \tag{6.13}$$

The predicted intensity $v_{k|k-1}(\boldsymbol{x})$ is given by the summation of the predicted intensity of surviving targets $v_{S,k|k-1}(\boldsymbol{x})$ and the intensity of new target births $\gamma_k(\boldsymbol{x})$. When the target dynamics (Eq. (3.2)) are linear Gaussian; that is, when

$$f_{k|k-1}(\boldsymbol{x}|\boldsymbol{\xi}) = p_g(\boldsymbol{x}\,;\, \boldsymbol{F}_{k-1}\boldsymbol{\xi}, \boldsymbol{Q}_{k-1})\,, \tag{6.14}$$

the intensity of existing targets can be propagated to t_k as

$$v_{S,k|k-1}(\boldsymbol{x}) = \sum_{j=1}^{J_{k-1}} w_{k|k-1}^{(j)} p_g(\boldsymbol{x}\,;\, \boldsymbol{m}_{S,k|k-1}^{(j)}, \boldsymbol{P}_{S,k|k-1}^{(j)})\,, \tag{6.15}$$

where

$$w_{k|k-1}^{(j)} = p_{S,k} w_{k-1}^{(j)} \tag{6.16}$$

$$\boldsymbol{m}_{S,k|k-1}^{(j)} = \boldsymbol{F}_{k-1}\boldsymbol{m}_{k-1}^{(j)} \tag{6.17}$$

$$\boldsymbol{P}_{S,k|k-1}^{(j)} = \boldsymbol{F}_{k-1}\boldsymbol{P}_{k-1}^{(j)}\boldsymbol{F}_{k-1}^{T} + \boldsymbol{Q}_{k-1}\,, \tag{6.18}$$

$\boldsymbol{F}_{k-1}$ is the state transition matrix (Eq. 3.1), and $\boldsymbol{Q}_{k-1}$ is the process noise covariance matrix. Note that in Equation (6.16), the target probability of survival is taken to be constant. With this, the predicted intensity of surviving targets $v_{S,k|k-1}$ and the superposition of the intensity of new target births γ_k form the predicted intensity

$$v_{k|k-1}(\boldsymbol{x}) = \sum_{j=1}^{J_{k|k-1}} p_g(\boldsymbol{x}\,;\, \boldsymbol{m}_{k|k-1}^{(j)}, \boldsymbol{P}_{k|k-1}^{(j)})\,. \tag{6.19}$$

At time t_k, the predicted target cardinality and intensity are updated with the available measurement data $\boldsymbol{Y}_k$ as [63]

$$p_k(n) = \frac{\Psi_k^0[w_{k|k-1}, \boldsymbol{Y}_k](n) p_{k|k-1}(n)}{\left\langle \Psi_k^0[w_{k|k-1}, \boldsymbol{Y}_k], p_{k|k-1} \right\rangle} \tag{6.20}$$

$$v_k(\boldsymbol{x}) = \frac{\left\langle \Psi_k^1[w_{k|k-1}, \boldsymbol{Y}_k], p_{k|k-1} \right\rangle}{\left\langle \Psi_k^0[w_{k|k-1}, \boldsymbol{Y}_k], p_{k|k-1} \right\rangle} (1 - p_{D,k}(\boldsymbol{x})) v_{k|k-1}(\boldsymbol{x}) \tag{6.21}$$

$$+ \sum_{\boldsymbol{y} \in \boldsymbol{Y}_k} \sum_{j=1}^{J_{k|k-1}} w_k^{(j)}(\boldsymbol{y}) p_g(\boldsymbol{x}\,;\, \boldsymbol{m}_k^{(j)}(\boldsymbol{y}), \boldsymbol{P}_k^{(j)}) \tag{6.22}$$

$$\Psi_k^u[w, \boldsymbol{Y}](n) = \sum_{j=0}^{\min(|\boldsymbol{Y}|, n)} (|\boldsymbol{Y}| - j)! p_{K,k}(|\boldsymbol{Y}| - j) P_{j+u}^n \frac{\langle 1 - p_{D,k}, v \rangle^{n-(j+u)}}{\langle 1, v \rangle^n} e_j\left(\Lambda(w, \boldsymbol{Y})\right) , \tag{6.23}$$

$$\Lambda_k(w, \boldsymbol{Z}) = \left\{ \frac{\langle 1, \kappa_k \rangle}{\kappa_k(\boldsymbol{y})} \left[\sum_{j=1}^{J_{k|k-1}} p_{D,k}(\boldsymbol{x}) w_{k|k-1}^{(j)} q_k^{(j)}(\boldsymbol{y}) \right] : \boldsymbol{y} \in \boldsymbol{Y} \right\} , \tag{6.24}$$

$$w_k^{(j)}(\boldsymbol{y}) = p_{D,k}(\boldsymbol{x}) w_{k|k-1}^{(j)} q_k^{(j)}(\boldsymbol{y}) \frac{\left\langle \Psi_k^1[w_{k|k-1}, \boldsymbol{Y}_k \setminus \{\boldsymbol{y}\}], p_{k|k-1} \right\rangle}{\left\langle \Psi_k^0[w_{k|k-1}, \boldsymbol{Y}_k], p_{k|k-1} \right\rangle} \frac{\langle 1, \kappa_k \rangle}{\kappa_k(\boldsymbol{y})} , \tag{6.25}$$

$$\boldsymbol{m}_k^{(j)}(\boldsymbol{y}) = \boldsymbol{m}_{k|k-1}^{(j)} + \boldsymbol{K}^{(j)}(\boldsymbol{y} - \boldsymbol{\eta}^{(j)}) , \tag{6.26}$$

$$\boldsymbol{P}_k^{(j)} = \left[\boldsymbol{I} - \boldsymbol{K}^{(j)} \boldsymbol{H}_k^{(j)} \right] \boldsymbol{P}_{k|k-1}^{(j)} , \tag{6.27}$$

$$w_{k|k-1} = \left[w_{k|k-1}^{(1)}, \ldots, w_{k|k-1}^{(J_{k|k-1})} \right]^T , \tag{6.28}$$

$$q^{(j)}(\boldsymbol{y}) = p_g(\boldsymbol{y}\,;\, \boldsymbol{\eta}^{(j)}, \boldsymbol{S}^{(j)}) , \tag{6.29}$$

$$\boldsymbol{\eta}^{(j)} = \boldsymbol{h}(\boldsymbol{m}_{k|k-1}^{(j)}) , \tag{6.30}$$

$$\boldsymbol{H}_k^{(j)} = \left. \frac{\partial \boldsymbol{h}(\boldsymbol{x})}{\partial \boldsymbol{x}} \right|_{\boldsymbol{x} = \boldsymbol{m}_{k|k-1}^{(j)}} , \tag{6.31}$$

$$\boldsymbol{S}^{(j)} = \boldsymbol{H}_k^{(j)} \boldsymbol{P}_{k|k-1}^{(j)} \boldsymbol{H}_k^{(j)^T} + \boldsymbol{R}_k , \qquad \text{and} \tag{6.32}$$

$$\boldsymbol{K}^{(j)} = \boldsymbol{P}_{k|k-1}^{(j)} \boldsymbol{H}_k^{(j)^T} \boldsymbol{S}^{(j)^{-1}} \tag{6.33}$$

In Equation (6.25), the GM weights are updated based on their associated components' probability of detection $p_{D,k}(\boldsymbol{x})$ and their measurement agreement $q^{(j)}(\boldsymbol{y})$ (see Eq. 6.29). The remaining terms in Equation (6.25) account for all of the pos-

sible target/target-originated measurements/clutter combinations. Equations (6.30)-(6.33) are simply the EKF equations, which for every measurement $\boldsymbol{y} \in \boldsymbol{Y}_k$ are applied to every component of the predicted intensity function $v_{k|k-1}$. As seen in Equations (6.23)-(6.25), the probability of detection $p_{D,k}$ is taken to be state-dependent. The state-dependent probability of detection can be approximated at the prior means, such that

$$p_{D,k}(\boldsymbol{x}) w_{k|k-1}^{(j)} \approx p_{D,k}(\boldsymbol{m}_{k|k-1}^{(j)}) w_{k|k-1}^{(j)}$$

$$\text{and} \qquad \langle 1 - p_{D,k}, v \rangle \approx \sum_{i=1}^{J_{k|k-1}} w_{k|k-1}^{(i)} (1 - p_{D,k}(\boldsymbol{m}_{k|k-1}^{(i)})) \,.$$

Altogether, the posterior intensity takes the form

$$v_k(\boldsymbol{x}) = \sum_{i=1}^{J_k} w_k^{(i)} p_g(\boldsymbol{x}\,;\, \boldsymbol{m}_k^{(i)}, \boldsymbol{P}_k^{(i)}) \,, \tag{6.34}$$

and the recursion continues.

6.3. MEASUREMENT MODEL

Similar to Chapter 5, angular measurements are taken from two cameras that are fixed to the inspector spacecraft. The use of two cameras separated at a known baseline (as opposed to a single-camera system) allows the state of a nearby target, which includes its relative position and velocity, to be resolved over multiple measurements. Furthermore, in using two cameras, no prior knowledge of the target's geometry is required.

6.3.1. Target-Originated Measurements. Robust image processing algorithms are available [43, 69, 70] that identify unique features on an imaged target and match the features between a stereoscopic image pair, such as in Figure 6.3. Similar to the case of Figure 6.3, multiple features are identified and matched for a single

target. Although the angles associated with these matched features will not, in general, correspond to the target's exact center of mass (CM), a simple averaging of the features' angles will result in a good approximation of the target's geometric center, which for geometrically small targets, will be close to the CM. Further improvements in accuracy can be made with prior knowledge of the target's geometry and mass distribution, as might be the case with cooperative swarms.

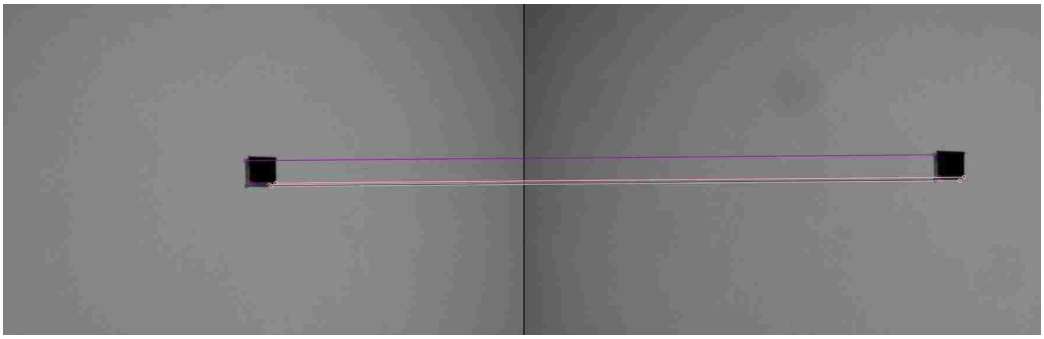

Figure 6.3. Example of image processing subsystem output for a single target. The lines demonstrate matched features between a stereoscopic image pair.

One of the primary benefits of the feature matching algorithm is that, because the features are matched between images, angles can be processed in pairs as opposed to individually. To that end, a single measurement is modeled as containing both angles from the stereo imager with additive Gaussian white noise as

$$\boldsymbol{y}_k = [\theta_{\,\mathrm{c1},k} \quad \theta_{\,\mathrm{c2},k}]^T + \boldsymbol{\nu}_k \,,$$

where $\theta_{\,\mathrm{cn}}$ is the azimuth angle measured from the y axis (assumed to be aligned with the Hill frame $\hat{S}$ axis) of the cn camera frame, $E\{\boldsymbol{\nu}_k\} = \mathbf{0}$, and $E\{\boldsymbol{\nu}_k \boldsymbol{\nu}_k^T\} = \boldsymbol{R}_k = \mathrm{diag}\{\sigma^2_{\theta\,\mathrm{c1},k}\,,\, \sigma^2_{\theta\,\mathrm{c2},k}\}$. For convenience, the camera frames are assumed to be aligned with the Hill frame. With this assumption, a stereoscopic measurement is related to

a target's state by the measurement function

$$\boldsymbol{h}(\boldsymbol{x}_k) = \begin{bmatrix} \tan^{-1}\left(u_{\,\mathrm{c1},k,x}/u_{\,\mathrm{c1},k,y}\right) \\ \tan^{-1}\left(u_{\,\mathrm{c2},k,x}/u_{\,\mathrm{c2},k,y}\right) \end{bmatrix}, \qquad \boldsymbol{u}_{\,\mathrm{cn}} = \frac{\delta\mathbf{r}_k - \boldsymbol{d}_{k,\,\mathrm{cn}}}{\left\|\delta\mathbf{r}_k - \boldsymbol{d}_{k,\,\mathrm{cn}}\right\|},$$

where $\delta\mathbf{r}_k$ is the relative position vector portion of the state $\boldsymbol{x}_k$ and $\boldsymbol{d}_{k,\,\mathrm{cn}}$ is the position of the cn camera frame origin with respect to the Hill frame origin.

6.3.2. False Alarms. Occasionally, the image processing subsystem will return measurements that do not correspond to actual targets, as illustrated in Figure 6.4. Such false alarms can be the result of sensor malfunctions, glint events [71],

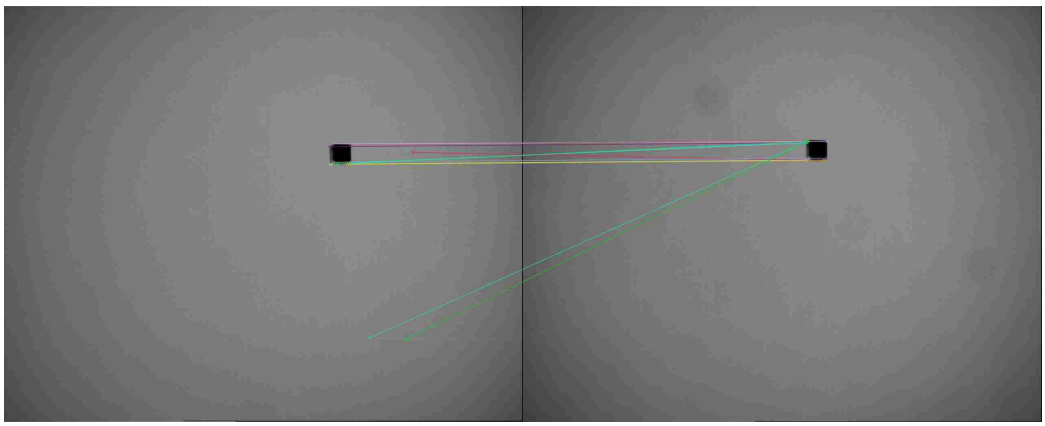

Figure 6.4. Example of false matches.

or other space-lighting phenomena. These false alarms are modeled by the clutter intensity $\kappa_k(\boldsymbol{y})$ and cardinality distribution $p_{K,k}(n)$. The clutter intensity is assumed to be uniform over the valid stereoscopic measurement domain D_s such that

$$\kappa_k(\boldsymbol{y}) = \lambda V \mathcal{U}(\boldsymbol{y}), \qquad \mathcal{U}(\boldsymbol{y}) = \begin{cases} 1/V & , \quad \boldsymbol{y} \in D_s \\ 0 & , \quad \text{otherwise} \end{cases},$$

where λ is the average number of clutter returns per unit "volume" and V is the sensor volume. Because false alarms exhibit the same properties as target-originated measurements, namely, that they correspond to LOSs that intersect in the composite field of view (CFOV), the volume V must represent the space over which stereoscopic measurements are valid. Valid stereo measurements are those for which the angular measurements belong to both of the cameras' fields of view (FOVs), and the LOSs they describe intersect in the positive-y half of the plane (in "front" of the cameras). For aligned cameras, to guarantee that the LOSs intersect, the azimuth angle from the leftmost sensor must always be greater than the azimuth angle from the rightmost sensor. With this, the sensor volume is obtained from the volume integral

$$V = \int_{D_s} 1 d\boldsymbol{y}\,, \qquad D_s = \left\{ \mathrm{FOV}_{\,\mathrm{c1}} \cap \mathrm{FOV}_{\,\mathrm{c2}} | \theta_{\,\mathrm{c1}} > \theta_{\,\mathrm{c2}} \right\}. \tag{6.35}$$

When the FOV angle is identical for both cameras; that is, when $\mathrm{FOV}_{\,\mathrm{c1}} = \mathrm{FOV}_{\,\mathrm{c2}} = \mathrm{FOV}$, the result of Equation (6.35) is simply $V = \frac{1}{2}\mathrm{FOV}^2$. The frequency of false alarms is dependent on a plethora of parameters related to the sensor, the image processing subsystem, lighting conditions, etc. The likelihood of receiving a given number of false alarms at time t_k is modeled by the clutter cardinality distribution $p_{K,k}(n)$. In this study, $p_{K,k}(n)$ is taken as Poisson, such that

$$p_{K,k}(n) = \frac{(\lambda V)^n}{n!} e^{-\lambda V}\,. \tag{6.36}$$

For real-world operations, $p_{K,k}(n)$ should be generated from ground-testing data before spaceflight.

6.3.3. Probability of Detection. The probability of detection $p_{D,k}(\boldsymbol{x}_k)$ represents the probability that a target with state $\boldsymbol{x}_k$ will be measured by the stereoscopic imager at t_k. As mentioned in the previous section, targets will, in general, have multiple features that are matched, such that when the target is visible, there

is a strong likelihood of detection. To that end, detection is taken to be guaranteed if the target exists in the domain of valid stereoscopic measurements and within the maximum ranges of the sensors, such that

$$p_{D,k}(\boldsymbol{x}_k) = \begin{cases} 1 \quad , \quad \boldsymbol{h}(\boldsymbol{x}_k) \in D_s \quad \text{and} \quad \|\delta\mathbf{r}_k - \boldsymbol{d}_{k,\,\mathrm{cn}}\| \leq \rho_{\max,\,\mathrm{cn}} \\ 0 \quad , \quad \text{otherwise} \end{cases} \tag{6.37}$$

where $\rho_{\max,\,\mathrm{cn}}$ is the maximum range of sensor cn.

Equation (6.37) is, in fact, a strong simplification of the complex metrological considerations involved in satellite vision-based navigation. Such considerations include, but are not limited to, the solar illumination geometry, sensor solar keep-out zones, and measurement occlusion caused by other targets [72]. These complex modeling considerations are beyond the scope of this study, as they are very sensor- and mission-dependent.

6.4. TARGET BIRTH

When new targets enter the inspector's stereoscopic FOV, their intensity γ_k must be superposed on the predicted intensity of existing targets $v_{S,k|k-1}$, and the cardinality pmf must be modified accordingly. It is assumed that measurements associated with new targets are identified. The assumption that the measurements of new targets are explicitly identified is certainly one of interest, but the development of such an identification mechanism is beyond the scope of the current work. Such mechanisms are not infeasible, however. For instance, one potential approach consists of applying a parallel process that analyzes image feature data to detect new targets and informs the birth process when a new target is detected. Additionally, this parallel process, when applied to the data, would identify the angular measurements in closest likelihood agreement with the new detection to be used by birth process.

With this, the birth intensity can be computed from a set of stereoscopic measurements using the IROD framework developed in Chapter 5. Recall that, in this framework, two stereoscopic angle measurements are collected at times t_1 and t_2. Henceforth, these times are denoted more generally as t_{k-2} and t_{k-1}, as birth processes can occur at any time step. At t_{k-2} and t_{k-1}, the angle measurement and corresponding uncertainty from Camera 2 are used to bound possible relative range values along Camera 1's LOS. The relative range uncertainty over these bounded regions is taken to be uniform and is approximated by a GM, as illustrated in Figure 5.3. The resulting pdfs are expressed in polar coordinates in the relative position space. Because the intent is to obtain a pdf that can be expressed in the single-target space, the set of positional polar coordinate pdfs are transformed into a full-state Cartesian pdf using a Lambert-linkage process.

As is developed Section 5.3, in the Lambert-linkage, components from the relative position mixture at t_{k-2} are linked to components from the relative position mixture at time t_{k-1} by computing the relative velocities that satisfy a given pair of relative positions and the time elapsed between them. Statistics are collected during this process such that the linkage of every component pair combination between t_{k-2} and t_{k-1} produces a unique birth component in the single-target space with appropriate weight, mean, and covariance.

Suppose that at times t_{k-2} and t_{k-1}, the measurements $\boldsymbol{y}_{k-2,\ell} \in \boldsymbol{Y}_{\text{birth},k-2}$, and $\boldsymbol{y}_{k-1,j} \in \boldsymbol{Y}_{\text{birth},k-1}$ are identified as measurements that originate from a new target. Note that, as implied by the subscripts ℓ and j, it is possible to introduce multiple birth targets at the same time step; however, because $\boldsymbol{Y}_{\text{birth}}$ is unordered, care must be taken to ensure that birth measurements at t_{k-2} and t_{k-1} are correctly matched to the appropriate target. For notational simplicity, the ℓ and j subscripts are dropped for the remainder of this section. Each measurement contains angles

from both cameras; that is

$$\boldsymbol{y}_{k-2} = [\theta_{\,\mathrm{c1},k-2} \quad \theta_{\,\mathrm{c2},k-2}]^T + \boldsymbol{\nu}_{k-2} \qquad \text{and}$$
$$\boldsymbol{y}_{k-1} = [\theta_{\,\mathrm{c1},k-1} \quad \theta_{\,\mathrm{c2},k-1}]^T + \boldsymbol{\nu}_{k-1}\,.$$

At t_{k-2} and t_{k-1}, the LOS of Camera 2 is rotated by a user-specified deviation in all directions, and the intersections between the rotated lines and LOS of Camera 1 are used to determine minimum and maximum relative range bounds $\rho_{\min}$ and $\rho_{\max}$, as is discussed in Chapter 5. In this study, the rotational deviation is chosen as three times the angular standard deviation of Camera 2. The points $\rho_{\min}$ and $\rho_{\max}$ represent the minimum and maximum relative range bounds (with respect to the camera frame) within which the position of the birth target is hypothesized and thus serve as the bounds in the construction of the relative range pdf. Note that $\rho_{\max}$ is not the same as the sensor range limitation $\rho_{\max,\,\mathrm{cn}}$. However, in the event that the bounding process generates a relative range $\rho_{\max}$ that is larger than the known sensor range limitation, $\rho_{\max,\,\mathrm{cn}}$ is appropriately used in the place of $\rho_{\max}$ as the upper bound on the relative range.

In the same fashion of Section 5.3, two single-target probability densities are formed in polar coordinates at t_{k-2} and t_{k-1}, given by

$$p_{z,k-2}(\boldsymbol{z}) = \sum_{\ell=1}^{L_{k-2}} w_{z,k-2}^{(\ell)} p_g(\boldsymbol{z}\,;\, \boldsymbol{m}_{z,k-2}^{(\ell)}, \boldsymbol{P}_{z,k-2}^{(\ell)})$$
$$\text{and} \qquad p_{z,k-1}(\boldsymbol{z}) = \sum_{\ell=1}^{L_{k-1}} w_{z,k-1}^{(\ell)} p_g(\boldsymbol{z}\,;\, \boldsymbol{m}_{z,k-1}^{(\ell)}, \boldsymbol{P}_{z,k-1}^{(\ell)})\,,$$

where

$$w_{z,k}^{(\ell)} = w_{\rho,k}^{(\ell)}\,, \qquad \boldsymbol{m}_{z,k}^{(\ell)} = [m_{\rho,k}^{(\ell)}\,,\, \theta_{\,\mathrm{c1},k}]^T\,, \qquad \text{and} \qquad \boldsymbol{P}_{z,k}^{(\ell)} = \mathrm{diag}\{\sigma_{\rho,k}^2\,,\, \sigma_{\theta\,\mathrm{c1},k}^2\}\,.$$

The Lambert-linkage consists of "linking" these two pdfs together to obtain a new pdf that includes relative velocity information. Every component pair combination must undergo a conversion from polar coordinates to Cartesian coordinates and a transformation from the camera frame to the Hill frame, after which a relative Lambert solution is found to provide the relative velocity that satisfies the two relative position components and their temporal separation. This linkage process is nonlinear, and thus to properly capture the statistics of this process, an unscented transform [51] is employed. Note that the unscented transform is necessary despite the choice of a linear CW Lambert solver due to the nonlinear nature of the coordinate transformations. The result of the Lambert-linkage process is an $L_{k-2} \cdot L_{k-1}$ component GM that approximates the single-target pdf in relative position and velocity and is expressed in Cartesian coordinates as

$$p_{x,k-2|k-1}(\boldsymbol{x}) = \sum_{\ell=1}^{L_{k-2}L_{k-1}} w_{x,k-2}^{(\ell)} p_g(\boldsymbol{x}\,;\, \boldsymbol{m}_{x,k-2}^{(\ell)}, \boldsymbol{P}_{x,k-2}^{(\ell)})\,.$$

The birth intensity at time t_k is then obtained by propagating $p_{x,k-2|k-1}(\boldsymbol{x})$ to time t_k, such that

$$\gamma_k(\boldsymbol{x}) = \int p_{S,k}(\boldsymbol{\xi}) f_{k|k-2}(\boldsymbol{x}|\boldsymbol{\xi}) p_{x,k|k-2}(\boldsymbol{x}) d\boldsymbol{\xi}\,.$$

In the event that multiple births occur simultaneously, the birth intensity is the summation of the new single-target pdfs given by

$$\gamma_k(\boldsymbol{x}) = \sum_{\boldsymbol{Y}_{\text{birth},k-2,k-1}} \int p_{S,k}(\boldsymbol{\xi}) f_{k|k-2}(\boldsymbol{x}|\boldsymbol{\xi}) p_{x,k|k-2}(\boldsymbol{x}) d\boldsymbol{\xi}\,.$$

where $\boldsymbol{Y}_{\text{birth},k-2,k-1}$ denotes the set of temporally-paired (between t_{k-2} and t_{k-1}) birth target measurements. The cardinality of births is taken as Poisson, yielding

$$\Gamma_k(n) = \frac{|\boldsymbol{Y}_{\text{birth},k-2,k-1}|^n}{n!} e^{-|\boldsymbol{Y}_{\text{birth},k-2,k-1}|},$$

so that higher target number birth events are treated with more uncertainty than lower target number birth events.

Because the birth intensity is formed from measurement data at t_{k-2} and t_{k-1}, the birth intensity is not introduced into the intensity model until another measurement is available, such that the birth intensity is not doubly conditioned on the same measurement data. A high-level block diagram of the complete tracking framework can be found in Figure 6.5.

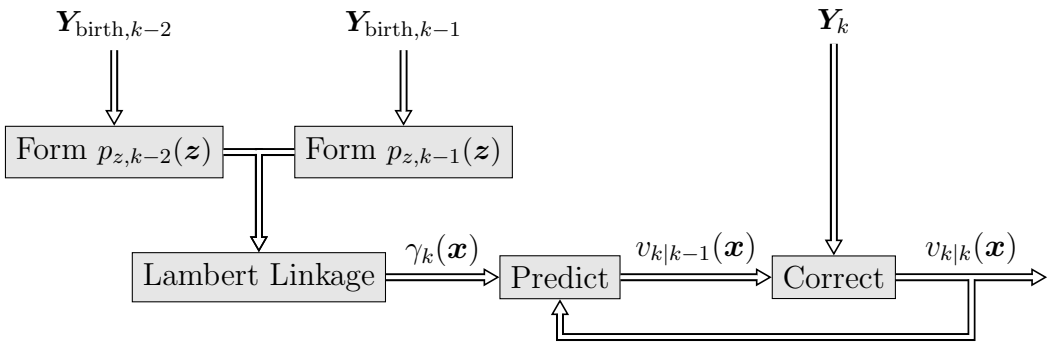

Figure 6.5. Block diagram of space-based relative multitarget tracking framework.

Figure 6.6 illustrates an example of a new birth target with two existing targets. In Figure 6.6a, the distribution on the left corresponds to a birth intensity at t_k. Its elongated nature is due to the large uncertainty in relative range and the uncertainty growth from propagation from t_{k-2} to t_k. Because of this, some birth components, when added to the intensity of surviving targets, reside outside of the

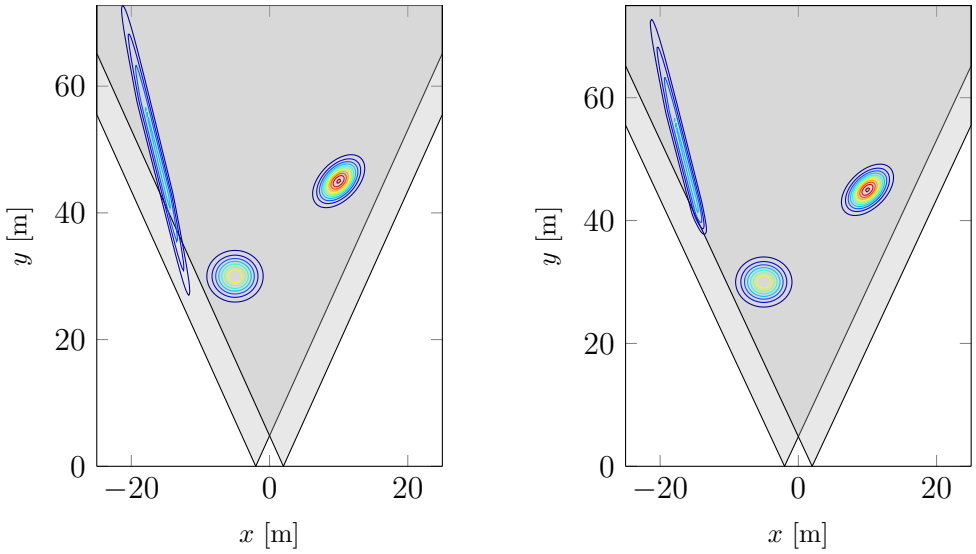

(a) Untruncated birth intensity.

(b) Truncated birth intensity.

Figure 6.6. Example of one birth with two existing targets.

detectable region, which is represented by the darker gray intersection of the cameras' FOVs. These components, if left unhandled, are treated as misdetected components and do not undergo a measurement update. In this specific example, these components will likely enter the detectable region at the following measurement update and thus undergo an update at t_{k+1}. In other cases, however, components may reside outside out of detection region due to their relative range and, furthermore, may never reenter the region. In applications where *all* target tracks are maintained indefinitely (i.e. $p_{S,k} = 1.0$), the persistence of such components can complicate numerical aspects of the filter. Instead, if a measurement is known to be associated with the birth target at t_k, that target is inherently detectable, and thus, all components that fall outside the detectable region can be safely truncated, as illustrated in Figure 6.6b. The truncated distribution is then renormalized and treated as the birth intensity.

The necessity of this truncation is more apparent when measurements are processed at high frequency, and more specifically, when little time is elapsed between

Lambert-linkage measurements. As discussed in Section 5.5, pdfs formed from small linkage times generally lead to a higher uncertainty in the target relative velocity as compared to pdfs formed from longer linkage times. In some cases, such as for exceptionally small linkage times, the large uncertainty in relative velocity will lead to propagated components that fall in the negative-y half plane ("behind" the camera).

Another approach to handling these "runaway" components is to implement a non-unity probability of survival. The effect of this is that components are down-weighted at every step, which over time, significantly reduces the contribution of components that are undetectable. For many terrestrial applications, specifically applications when target motion is secular, values between 0.95 and 0.99 for $p_{S,k}$ are common [73, 74]. Conversely, for ground-based tracking of geostationary satellites, where a future measurement is almost certainly guaranteed due to the satellites' intrinsic periodic motion, $p_{S,k} = 1$ is appropriate. Satellite relative motion is both secular and periodic, and as a result, target survival is not as straightforward. Potential approaches could involve computing the probability of re-detection based on states extracted from the intensity function. The states of targets with low probabilities of re-detection may be converted to inertial states for long-term propagation while their corresponding components are downweighted. Currently, more sophisticated target survival schemes are being investigated and will be considered in future work.

6.5. NUMERICAL CONSIDERATIONS AND ANALYSIS METRICS

6.5.1. GM Reduction. At each measurement update, the PHD and CPHD posterior intensities are reduced according to the same pruning/merging laws. Gaussian components are combined if their Mahalanobis distance, defined between two

Gaussian components i and j as

$$D = (\boldsymbol{m}^{(i)} - \boldsymbol{m}^{(j)})^T \boldsymbol{P}^{(i)^{-1}} (\boldsymbol{m}^{(i)} - \boldsymbol{m}^{(j)}) ,$$

falls below a user-specified merging threshold U. Given a component j, all of the components satisfying the merging threshold (including j) are collected and merged. The merged weight $\tilde{w}$ is simply the sum of the collected weights. The merged mean $\tilde{\boldsymbol{m}}$ is a weighted average of the collected components' means. The merged covariance $\tilde{\boldsymbol{P}}$ is a weighted average of the collected components' covariances and cross-covariances (between the original component and merged component). The complete merging algorithm, which is adapted from Reference [75], is presented in Algorithm 3. After the merging stage, components with weights less than a user-specified pruning threshold T are removed from the mixture.

Algorithm 3: Component Merging

Given $\{w_k^{(i)}, \boldsymbol{m}_k^{(i)}, \boldsymbol{P}_k^{(i)}\}$ and merging threshold U:

Set $\ell = 0$ and $I = \{i = 1, \ldots, J_k\}$.

repeat

$\ell = \ell + 1$.

$j = \underset{i \in I}{\operatorname{argmax}}\, w_k^{(i)}$.

$L = \left\{ i \in I \middle| (\boldsymbol{m}_k^{(i)} - \boldsymbol{m}_k^{(j)})^T \boldsymbol{P}_k^{(i)^{-1}} (\boldsymbol{m}_k^{(i)} - \boldsymbol{m}_k^{(j)}) \leq U \right\}$.

$\tilde{w}_k^{(\ell)} = \sum_{i \in L} w_k^{(i)}$.

$\tilde{\boldsymbol{m}}_k^{(\ell)} = \frac{1}{\tilde{w}_k^{(\ell)}} \sum_{i \in L} w_k^{(i)} \boldsymbol{m}_k^{(i)}$.

$\tilde{\boldsymbol{P}}_k^{(\ell)} = \frac{1}{\tilde{w}_k^{(\ell)}} \sum_{i \in L} \left(\tilde{\boldsymbol{P}}_k^{(i)} + (\tilde{\boldsymbol{m}}_k^{(\ell)} - \boldsymbol{m}_k^{(i)})(\tilde{\boldsymbol{m}}_k^{(\ell)} - \boldsymbol{m}_k^{(i)})^T \right)$.

$I = I \setminus L$.

until $I = \emptyset$.

Output $\left\{ \tilde{w}_k^{(i)}, \tilde{\boldsymbol{m}}_k^{(i)}, \tilde{\boldsymbol{P}}_k^{(i)} \right\}_{i=1}^{\ell}$ as merged Gaussian components.

6.5.2. Cardinality Statistics. After completing the GM reduction step, for analysis purposes, the cardinality means and standard deviations for the CPHD filter are computed as

$$\hat{N}(k) = \sum_{n=0}^{n_{\max}} n p_k(n) \tag{6.38}$$

$$\sigma(k) = \sqrt{\sum_{n=0}^{n_{\max}} (n - \hat{N}(k))^2 p_k(n)}\,. \tag{6.39}$$

Alternatively, cardinality estimates for both PHD and CPHD solutions can be attained by utilizing the important relationship

$$\hat{N}(k) = \int v_k(\boldsymbol{x}) d\boldsymbol{x}\,, \tag{6.40}$$

which can be simply computed by summing the intensity's Gaussian component weights; that is

$$\hat{N}(k) = \sum_{i=1}^{J_k} w_k^{(i)}\,. \tag{6.41}$$

6.5.3. State Extraction. One of the greatest challenges of PHD and CPHD implementation is accurately and reliably extracting target state estimates from the intensity function. One simple approach to state extraction involves selecting all the components with weights that are greater than a threshold (most commonly, 0.5) and treating the corresponding components' means as the state estimates at that time step [75]. This method is attractive because of its simplicity. Although this method performs sufficiently for reasonably simple problems, it often produces inaccurate estimates for more complex models, both in the number of estimates returned and the estimates themselves.

A more sophisticated and reliable method for state extraction is discussed in Reference [76]. This maximum likelihood-based method is performed in three steps: clustering, mode finding, and blending. First, the means of the posterior intensity components are clustered together using the K-means algorithm [77]. The centers of these clusters serve as the initial guesses in the optimization problem that finds the point of locally maximum likelihood. Finally, these points, or peaks, are "blended" by averaging all of the components' means in close proximity of the peak. The blended estimates are sorted by their likelihood, and the highest $\hat{N}(k)$ are taken as the state estimates.

6.5.4. Multitarget Miss Distance. Wherein single-target filtering a multitude of error metrics are readily available, in multitarget filtering, the concept of a "miss distance" is not well-defined. This notion is especially true when attempting to quantify the miss distance between two unequally-sized sets. One proposed metric, known as the optimal subpattern assignment (OSPA) metric [78], defines the p^{th}-order miss distance between two arbitrary sets $\boldsymbol{X} = \{\boldsymbol{x}_1, \ldots, \boldsymbol{x}_m\}$ and $\boldsymbol{Y} = \{\boldsymbol{y}_1, \ldots, \boldsymbol{y}_n\}$ as

$$\bar{d}_p^{(c)}(\boldsymbol{X}, \boldsymbol{Y}) \triangleq \left[\frac{1}{n} \left(\min_{\pi \in \Pi_n} \sum_{i=1}^{m} d^{(c)}(\boldsymbol{x}_i, \boldsymbol{y}_{\pi(i)})^p + c^p(n-m) \right) \right]^{1/p}, \tag{6.42}$$

if $m \leq n$, and $\bar{d}_p^{(c)}(\boldsymbol{X}, \boldsymbol{Y}) \triangleq \bar{d}_p^{(c)}(\boldsymbol{Y}, \boldsymbol{X})$ if $m > n$. Establishing $d(\boldsymbol{x}, \boldsymbol{y})$ to be a distance of some sort (treated as Euclidean in this study) between $\boldsymbol{x}$ and $\boldsymbol{y}$, the modified distance $d^{(c)}$ is defined as $d^{(c)}(\boldsymbol{x}, \boldsymbol{y}) \triangleq \min\big(c, d(\boldsymbol{x}, \boldsymbol{y})\big)$ with cut-off distance c. The cut-off distance c effectively controls how much a cardinality error is penalized relative to localization penalties. For the case $p = 1$, c is exactly the penalty assigned to each missing target. Note that the OSPA metric is minimized over the set Π_k of permutations on $\{1, 2, \ldots, k\}$. In other words, when evaluating the accuracy of a set of state estimates, every possible match between estimate and truth is considered. This

combinatoric nature can be computationally troublesome in naive implementations of the OSPA. Fortunately, a fast implementation of this calculation, as well as further explanation and analysis of the OSPA metric, is provided in Reference [65].

6.6. TRACKING SIMULATION

The performance of the CPHD filter as well as the PHD filter [75, 79] is investigated in the context of a simulated debris cloud tracking problem. The inspector satellite occupies a 400 km altitude circular Earth orbit. For simplicity, the satellite is modeled to rotate with the Hill frame, such that the inspector's cameras always point along the positive $\hat{S}$ axis of the Hill frame (Figure 2.1), and perfect attitude knowledge is assumed.

Two cameras are fixed to the inspector spacecraft, and due to the chosen rotation of the inspector spacecraft, their locations within the Hill frame are constant and are described by

$$\boldsymbol{d}_{\,\mathrm{c1}} = [-2,\, 0]^T \text{ [m]} \qquad \text{and} \qquad \boldsymbol{d}_{\,\mathrm{c2}} = [2,\, 0]^T \text{ [m]}\,.$$

Measurements from the stereo imager (comprised of the two cameras) are received every 60 seconds in the form of bearings angles. In the synthesis of these measurements, the true angles are corrupted by zero-mean Gaussian noise with a standard deviation of 750 [arcsec], which corresponds to a five pixel deviation on a 1080×1080 pixel focal plane array with a 45 [deg] FOV. Targets are treated as undetectable if they fall outside of either camera's FOV or are more than 150 [m] away from either camera. False alarms are generated in accordance with a Poisson cardinality distribution (Eq. (6.36)) with mean $\lambda V = 2$ returns per collection.

Targets are initialized in close proximity to the inspector spacecraft, and their true initial relative states are listed in Table 6.2. The initial target cardinality pmf is

initialized as uniform between zero and nineteen; that is

$$\Pr(N(0) = n) = 0.05 \quad \forall \quad n \in \{0, \ldots, 19\}\,.$$

In plain terms, it is initially assumed that it is equally probable that the total number of targets is anywhere between zero and nineteen. The initial states are propagated using CW dynamics to produce the truth model, of which the positional histories are shown in Figure 6.7. For convenience, the intensity function is initialized with component means at the visible targets' true states, with component covariances given by $\boldsymbol{P}_0^{(i)} = \text{diag}\{2^2,\, 2^2,\, 0.01^2,\, 0.01^2\}$ in m^2 and m^2/s^2 as shown in Figure 6.8. It is clear from Figure 6.7 that only six of the nine targets are initially visible to both cameras, and thus, only six targets are represented in the initial intensity function, as seen in Figure 6.8a. Due to the relatively large uncertainty in the initial relative velocity intensity, the six unique target velocities are indistinguishable in Figure 6.8b.

Table 6.2. Initial relative states of targets.

Target	x [m]	y [m]	$\dot{x}$ [m/s]	$\dot{y}$ [m/s]
1	4.96026332	38.32210715	0.00441559	-0.01124242
2	5.39555258	18.63914052	-0.00715109	-0.00773215
3	-11.33700072	36.87592374	0.00532677	0.02230584
4	-8.86908651	23.98647305	-0.00436219	0.01892312
5	-14.29718807	27.12171413	-0.00070161	0.02893518
6	-3.07473223	14.79459501	-0.00459050	0.00995115
7	-0.16750985	18.95011169	-0.00591691	-0.00320291
8	-6.24943905	39.15861624	0.00750975	0.00747834
9	-16.15237908	18.14938250	-0.00111060	0.03229021

The PHD filter and CPHD filter are employed to recursively predict and correct the intensity function. Using Equations (6.38) and (6.41), the cardinality esti-

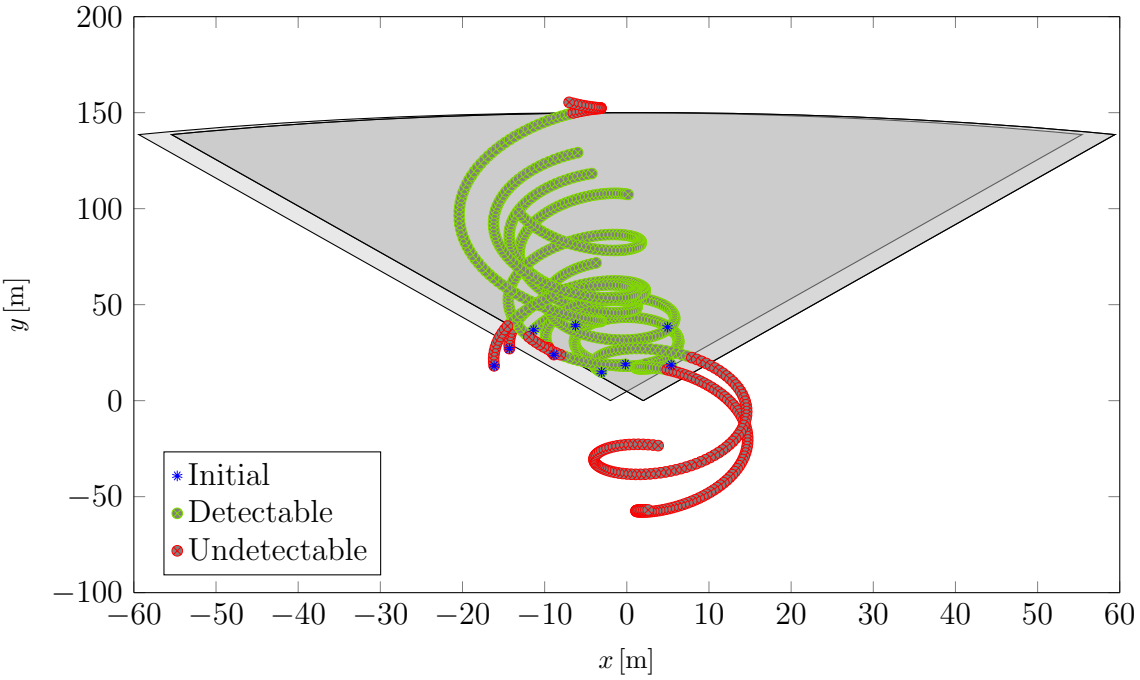

Figure 6.7. Relative position histories of nine targets. The gray shaded regions represent the camera FOVs.

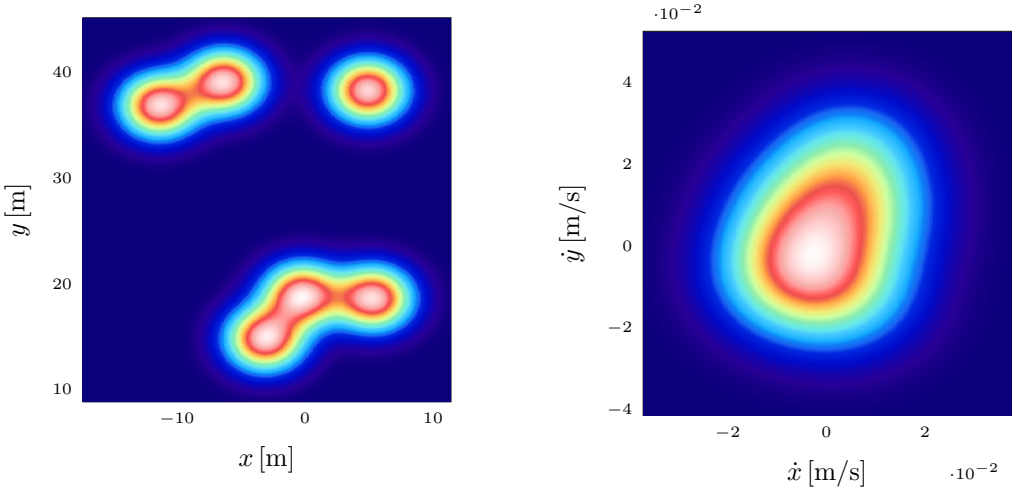

(a) Position.

(b) Velocity.

Figure 6.8. Initial relative position and velocity intensities. Six of the nine targets are represented in the initial intensity. Due to the relatively high uncertainty in the relative velocities, the individual contributions of the targets are indistinguishable.

mates for the CPHD and PHD solutions, respectively, are computed and compared to the true target cardinality in Figure 6.9. As shown, the three targets that are not accounted for by the initial intensity function are instantiated over the first several time steps via the birth process. The PHD filter overestimates the cardinality for

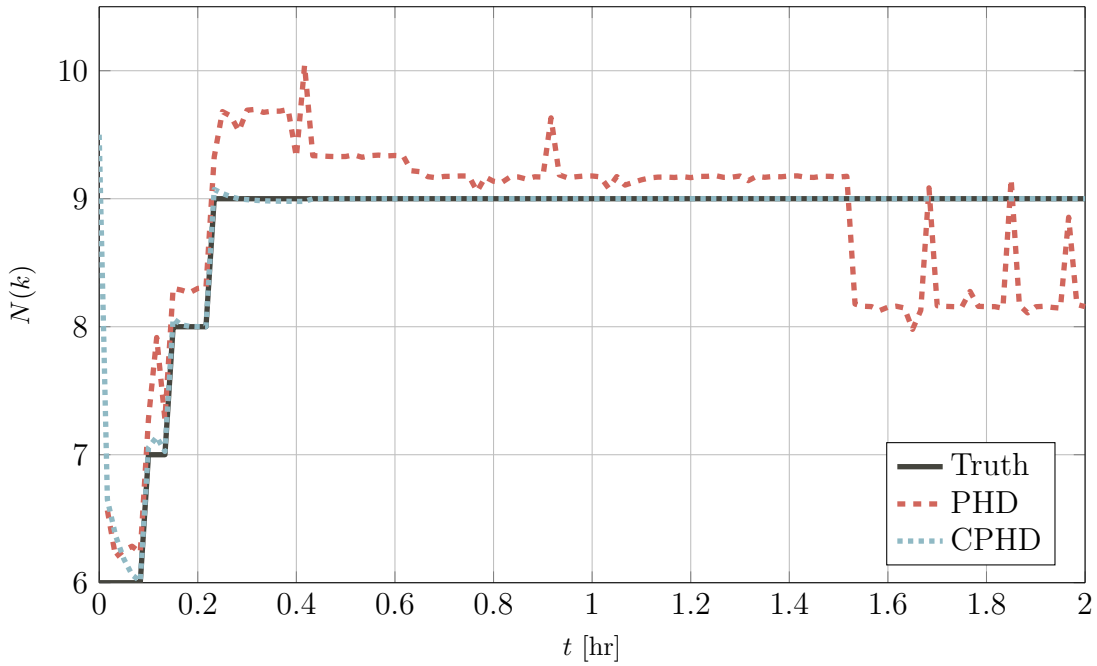

Figure 6.9. PHD and CPHD cardinality estimates and true target cardinality.

two of these three births, and in general, exhibits much less accurate cardinality estimates than its cardinalized counterpart. For a closer examination of the CPHD's cardinality estimate, the cardinality error and pmf standard deviation are provided in Figure 6.10. Note that shortly after $t = 1.5\,[\text{hr}]$, the cardinality error falls below 64-bit machine precision, thus making the log error undefined.

At each time step, the posterior intensity GM is reduced using a merging threshold of $U = 0.1$ and a pruning threshold of $T = 1 \times 10^{-5}$. After GM reduction, the state estimates are extracted from the PHD and CPHD intensities us-

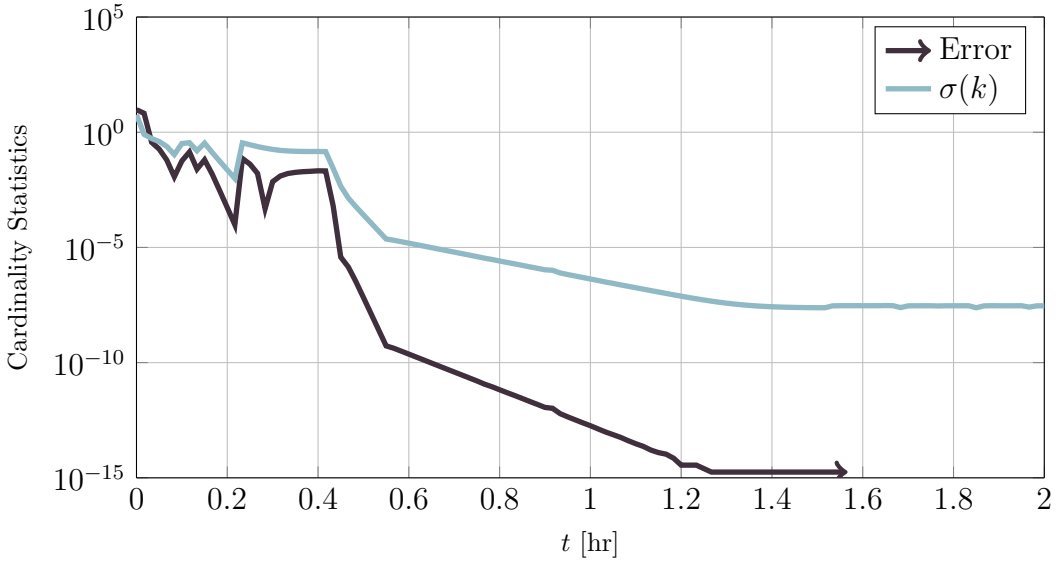

Figure 6.10. CPHD cardinality statistics.

ing the clustering/mode-finding/blending technique as described in Section 6.5.3. The x and y position coordinates of the extracted states are shown over time in Figures 6.11-6.12.

As is apparent in Figures 6.11 and 6.12, a false target state is consistently extracted from the PHD intensity. Recall that the number of estimates returned by the state extraction process directly corresponds to $\hat{N}(k)$. Because the PHD solution consistently over-estimates the target cardinality (Figure 6.9), the state extraction routine provides an extraneous target estimate corresponding to the next-highest likelihood point.

For clarity, Figures 6.11 and 6.12 are repeated with different scales in Figures 6.13 and 6.14, respectively. As seen at many of the time steps, some estimates extracted from PHD solution do not fall near the true tracks. Examples of this trend are labeled in Figures 6.13 and 6.14 using the marker (1). In contrast to the PHD solution state estimates, the estimates taken from the CPHD always closely agree with true tracks with only a few exceptions. However, on multiple occasions, a target's

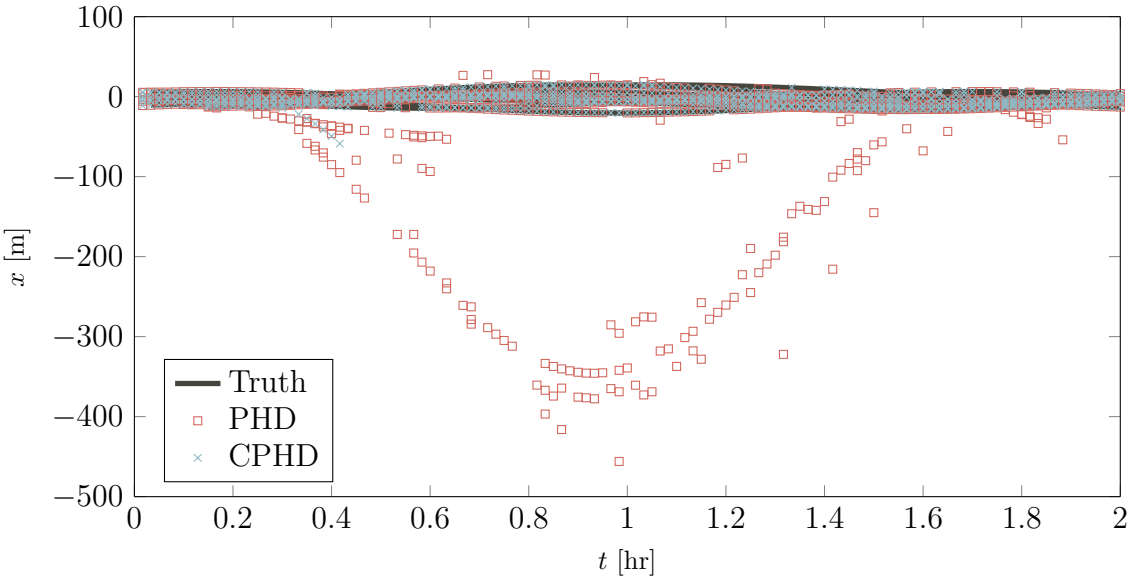

Figure 6.11. Comparison of x-coordinate position estimates to the true x-coordinate position histories.

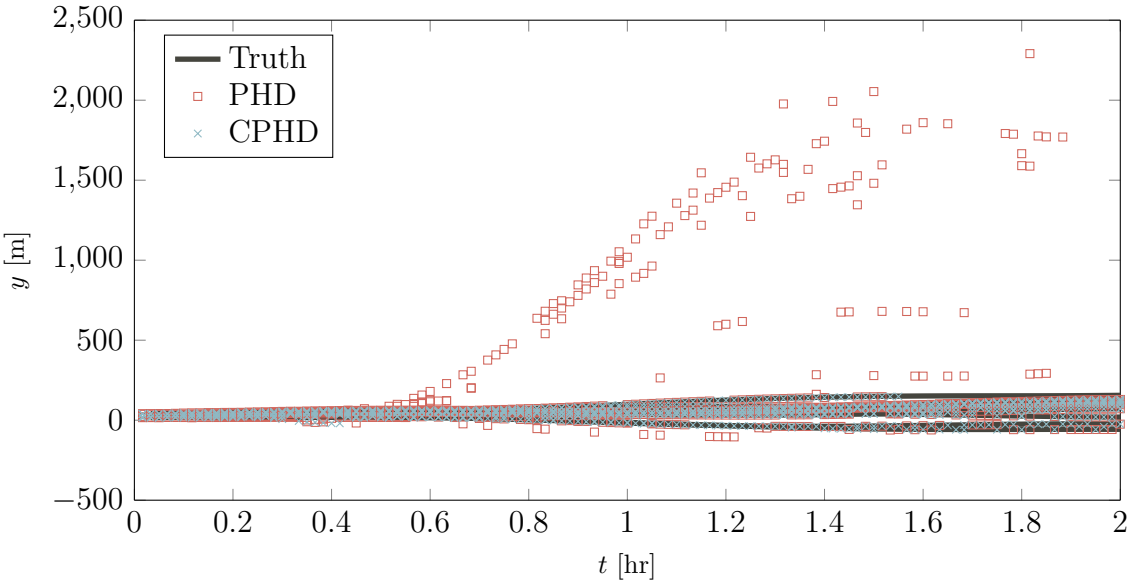

Figure 6.12. Comparison of y-coordinate position estimates to the true y-coordinate position histories.

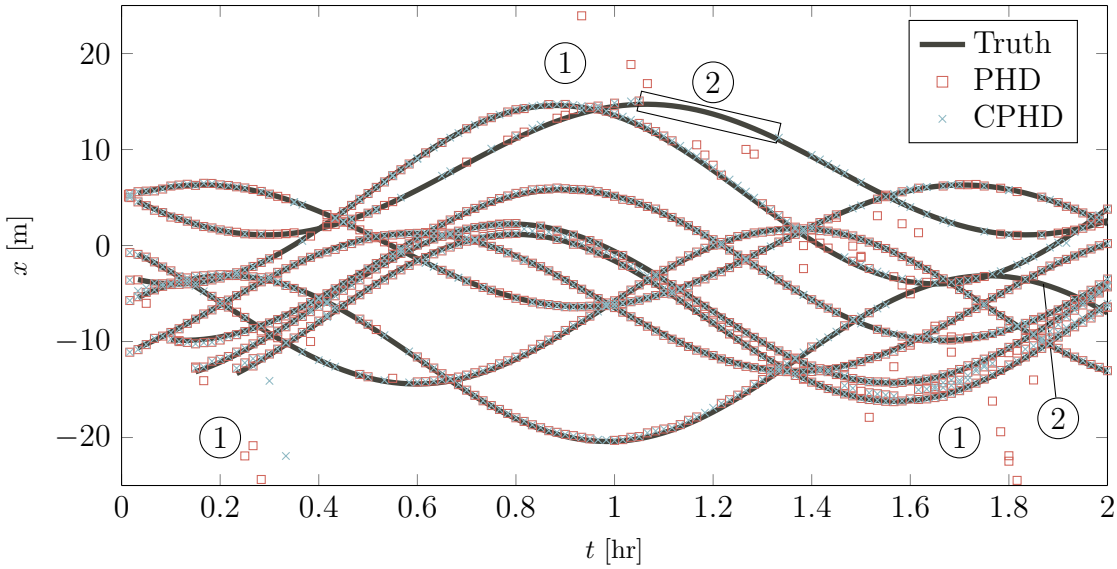

Figure 6.13. Comparison of x-coordinate position estimates to the true x-coordinate position histories. (1) denotes instances of PHD false extraction. (2) denotes instances of CPHD missed tracks due to duplicate extractions.

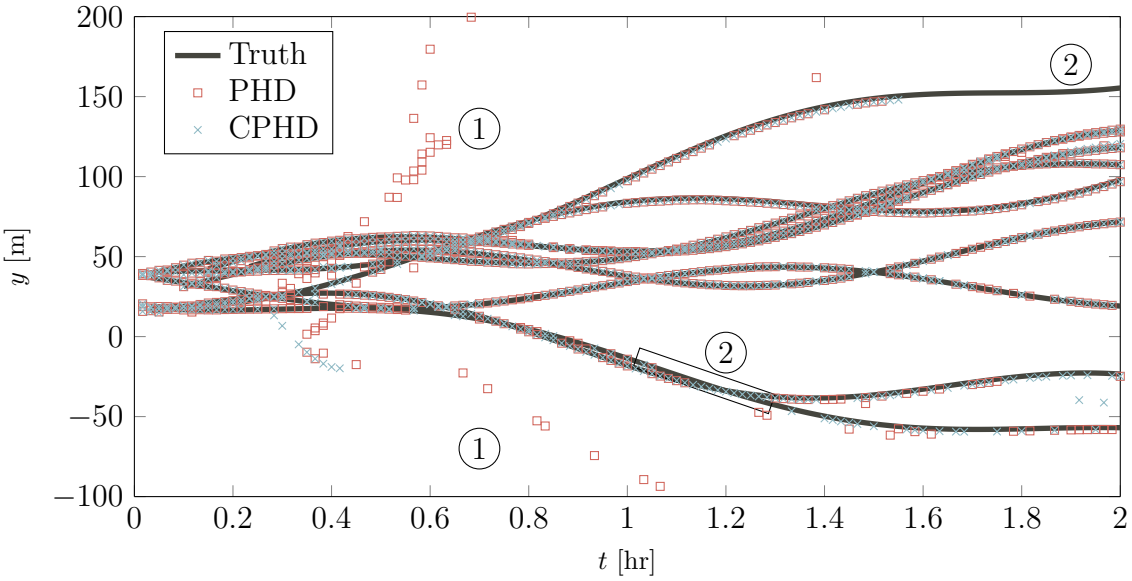

Figure 6.14. Comparison of y-coordinate position estimates to the true y-coordinate position histories. (1) denotes instances of PHD false extraction. (2) denotes instances of CPHD missed tracks due to duplicate extractions.

true state has no corresponding state estimate from either intensity solution. These instances are labeled in Figures 6.13 and 6.14 using the marker (2). In the case of the CPHD, these "missing" estimates are the result of the state extraction routine producing one or more duplicate estimates in lieu of the unaccounted target(s). Duplicate estimates occur when two or more local maxima are found in close proximity and the corresponding likelihoods are large enough to make the $\hat{N}(k)$-highest "cut." Note that these duplicates cannot simply be discarded, as it is possible for two or more closely-spaced targets to produce a similar result. Although not pursued in this study, proper tuning of the state extraction parameters can greatly reduce the number of false duplicates. In the case of the PHD, the missing estimates are either the result of duplicate estimates, false estimates caused by an inaccurate cardinality estimate, or simply poor accuracy in the PHD intensity solution.

The miss distance between these extracted state estimates and the true target states is computed using the OSPA metric [78]. In order to maintain a physical interpretability, the metric is computed using only the relative position coordinates of the states; this allows the cutoff distance c to be defined using physical units. Here, a cutoff of $c = 10\,[\text{m}]$ is chosen. In the computation of the OSPA metric, in a given permutation π, if the distance between the true position state $\boldsymbol{x}_i$ and estimated position state $\boldsymbol{y}_{\pi(i)}$ exceeds $10\,[\text{m}]$, it is treated as a missed target. With this, the OSPA metric is computed and shown in Figure 6.15. The accuracy of the CPHD clearly filter exceeds that of the PHD filter with the exception of only a few time steps, as is expected. The first-order OSPA metric ($p = 1$) can be interpreted as a measure of the "per target" error. With this interpretation, both the PHD and CPHD filters achieve a submeter level per target tracking errors during the first $0.2\,[\text{hr}]$ of the simulation due to the close proximity of the targets. As the targets drift farther away, the OSPA metric increases slightly for both solutions. The maximum per target errors experienced are $\sim 6\,[\text{m}]$ for the PHD filter and $\sim 5\,[\text{m}]$ for the CPHD filter.

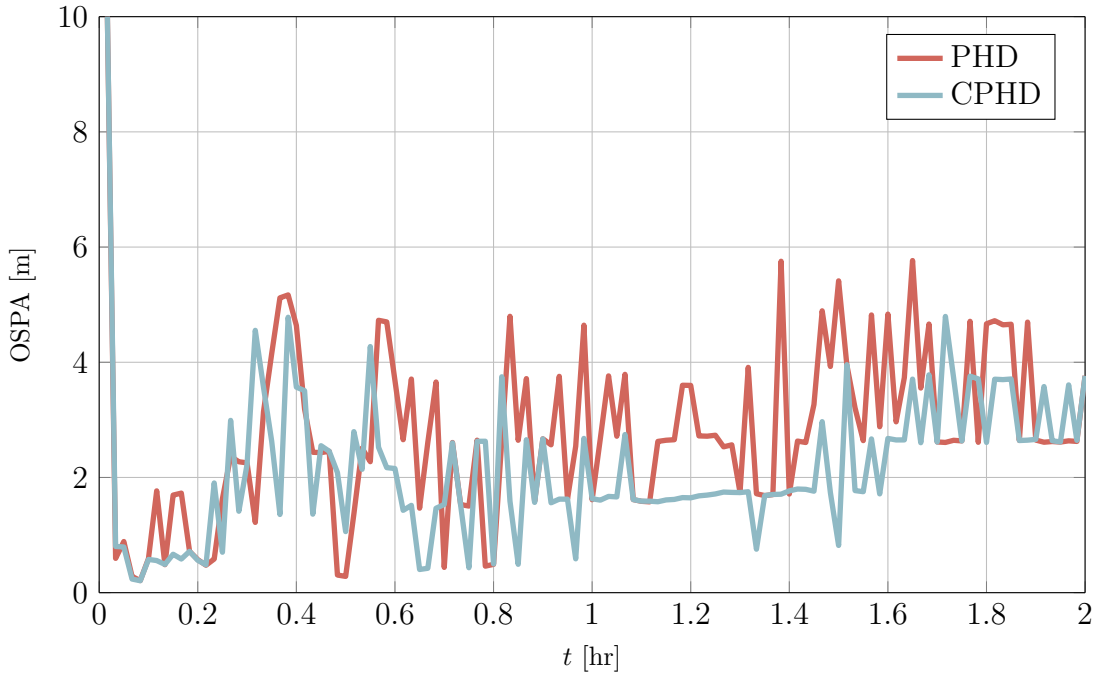

Figure 6.15. First-order OSPA metric with cutoff $c = 10\,[\mathrm{m}]$.

It is often accepted that the CPHD filter requires additional execution time in its recursion in comparison to the PHD because of its cubic complexity in measurements. This generalization, however, is only valid under the assumption that the number of components between the PHD and CPHD intensity mixtures remains the same. In many cases, such as the presented example, the CPHD update and subsequent reduction step, in fact, produces a more tightly concentrated intensity function with far fewer components. To that end, the total recursion time, or time elapsed from the beginning of the prediction step to the end of the correction step, for the CPHD filter is often less than the PHD filter. This trend is exemplified in Figure 6.16, which compares the nondimensional execution times of the PHD and CPHD filters. As execution time is highly system-dependent, all of the times are divided by the maximum execution time, such that all of the execution times fall between zero and one. As shown in Figure 6.16, in this example, the PHD filter is responsible for the

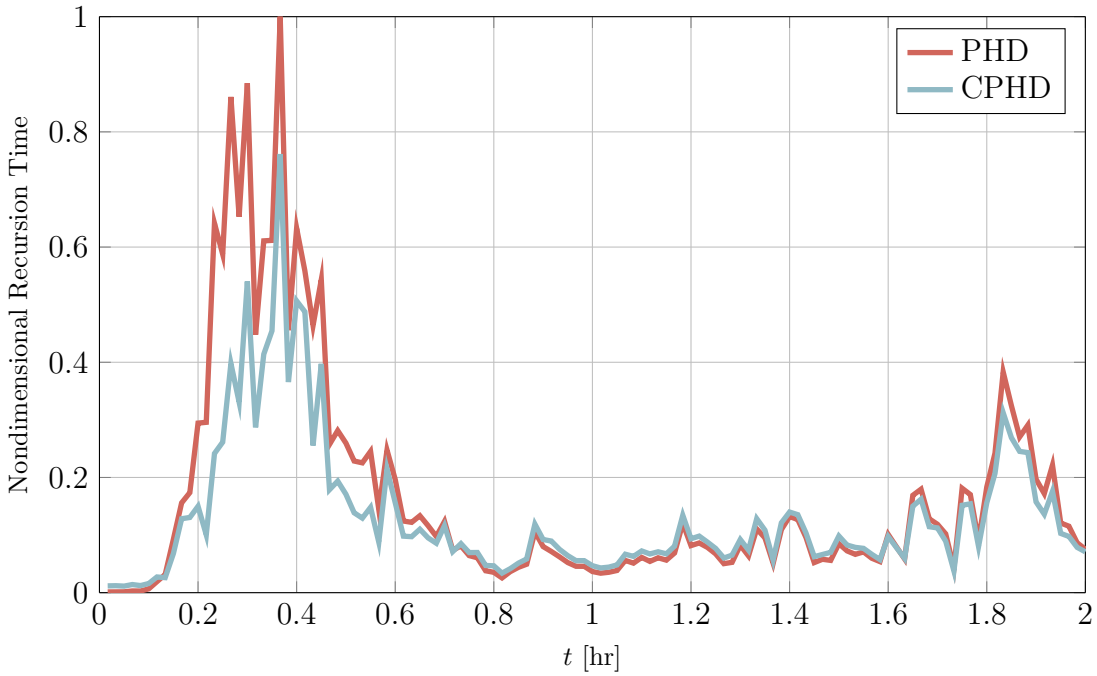

Figure 6.16. Nondimensionalized recursion execution times.

highest single-step recursion time. In fact, the recursion time of the CPHD filter is often less than that of the PHD filter, specifically during and following time steps when new targets are instantiated.

The simulation presented in this study is far from exhaustive. There exist far too many simulation parameters to consider an exhaustive study of their influence on filter performance. These parameters include, but are not limited to, number of targets, frequency and cardinality of births, measurement noise distribution, frequency of measurements, camera baseline separation, frequency and distribution of false alarms, and choice of GM reduction method. Although such a study is not pursued, it should noted that the simulation parameters are chosen here to reflect reasonable multitarget scenarios and small satellite hardware; values are not "cherry-picked" to support any hypothesis. It thus stands to reason that the trends observed in cardinality accuracy, localization accuracy, and recursion execution time are not unique to the presented results and can be observed for a variety of simulation parameter selections.

7. CONCLUSIONS

A Lambert solver for relative satellite motion is presented, which computes an initial relative velocity of a satellite given two unique relative positions and their associated times. The relative Lambert solver finds all of the relative velocity vectors that satisfy a set of CW2 equations, which can be expressed mathematically as a set of degree-two trivariate polynomials and geometrically as three quadric surfaces. The solutions of these polynomials are computed non-iteratively using Macaulay resultant expressions and eigendecomposition methods. This second-order relative Lambert solver, or CW2 solver, is compared to the first-order Clohessy-Wiltshire (CW) solver equivalent, as well as a method that involves mapping the relative vectors back into the inertial frame and performing a traditional Lambert solver. It is shown that the CW2 solver, in terms of solution accuracy, surpasses the CW solver by several orders of magnitude, and that sub-centimeter miss-distances are consistently achieved except for in the degenerate cases when the time of flight is equal to the orbital half-period.

The applications of Gaussian mixture models and space-based stereoscopic imaging to satellite close proximity operations are presented. The limitations of typical stereoscopic measurement schemes are mitigated by using stereoscopic geometry to bound relative position range, for which uniform uncertainty is assumed. It is shown that the uniform range uncertainty can be approximated with a mixture of Gaussian probability density functions (pdfs). By applying these approximations over two discrete measurements and linking all possible combinations of the Gaussian components with a relative Lambert solver, a full state Cartesian pdf is composed. For single-target tracking, the resultant pdf is further refined by processing subsequent angle measurements in a Bayesian framework, which results in high accuracy relative orbit determination.

When performing bearings-only initial relative orbit determination (IROD), it is found that, in general, using measurements taken farther apart in time results in initial pdfs that are more tightly concentrated about the mean; that is, they have less uncertainty. One exception to this trend is when measurements are taken at integer-multiples of the orbital half-period, as there exist infinitely many relative velocity solutions that satisfy such a set of measurements. By examining the Shannon entropies of the pdfs, it is shown that the pdf's correlations and higher-order moments are more influential at larger along-track separation distances. A Monte Carlo simulation with synthetic data characterizes the performance of the Bayesian filter, which demonstrates average tracking errors of less than 10 [cm] and 10 [μm/s] in relative position and velocity, respectively, in a common relative orbit determination scenario, where synthetic angular measurements with a standard deviation of 67 [arcsec] are processed at 1 [Hz]. Finally, it is shown that these errors can be improved by widening the separation between the stereo cameras, and that doubling the baseline can result in a twofold improvement in accuracy.

Multitarget frameworks for tracking an unknown number of noncooperative targets in nearby orbits from a space-based platform using the probability hypothesis density (PHD) and cardinalized probability hypothesis density (CPHD) filters are presented. The relative motion of several targets and the number of targets are estimated by propagating the first-moment approximation of the multitarget pdf and the target cardinality distribution, respectively. A stereoscopic imaging system onboard the inspector satellite produces noisy inspector-to-target angular measurements and sporadic false alarms, both of which are processed jointly to refine the state and cardinality estimates. A measurement-driven model for introducing previously untracked targets into the tracking solution is formulated using the bearings-only IROD algorithm.

To evaluate the performance of the presented multitarget frameworks, a satellite debris cloud tracking problem is simulated using synthetic measurements, in which stereoscopic angle measurements are corrupted with 750 [arcsec] standard deviation white noise. A total of nine targets are tracked, and the Gaussian mixture implementations of the PHD and CPHD filters are compared based on their state estimate accuracy, cardinality estimate accuracy, and recursion execution time. In the presented example, the CPHD filter consistently produces solutions that are far more accurate than the PHD filter in their state and cardinality estimates. Furthermore, when the Gaussian mixture representations of the intensity are subjected to the same pruning/merging rules, the resulting CPHD intensity solution often contains significantly fewer components and thus benefits from shorter total execution times in its subsequent recursions. In the presented example, the highest execution time savings of the CPHD filter over the PHD filter are observed when new targets are introduced into the tracking solutions times.

APPENDIX: CW2 SYSTEM MATRIX

By consolidating the redundant state elements in the Kronecker form state $\boldsymbol{x}^{\otimes}$ (42×1) to form the new state $\bar{\boldsymbol{x}}$ (27×1), the system matrix $\bar{\boldsymbol{A}}$ is reduced to

$$\bar{\boldsymbol{A}} = \begin{bmatrix} \mathbf{0}_{3\times3} & \boldsymbol{I}_{3\times3} & \mathbf{0}_{3\times3} & \mathbf{0}_{3\times3} & \mathbf{0}_{3\times3} & \mathbf{0}_{3\times3} & \mathbf{0}_{3\times3} & \mathbf{0}_{3\times3} & \mathbf{0}_{3\times3} \\ \bar{\boldsymbol{A}}_{21} & \bar{\boldsymbol{A}}_{22} & \bar{\boldsymbol{A}}_{23} & \mathbf{0}_{3\times3} & \bar{\boldsymbol{A}}_{25} & \bar{\boldsymbol{A}}_{26} & \mathbf{0}_{3\times3} & \mathbf{0}_{3\times3} & \mathbf{0}_{3\times3} \\ \mathbf{0}_{3\times3} & \mathbf{0}_{3\times3} & \mathbf{0}_{3\times3} & \bar{\boldsymbol{A}}_{34} & \bar{\boldsymbol{A}}_{35} & \mathbf{0}_{3\times3} & \bar{\boldsymbol{A}}_{37} & \mathbf{0}_{3\times3} & \mathbf{0}_{3\times3} \\ \mathbf{0}_{3\times3} & \mathbf{0}_{3\times3} & \bar{\boldsymbol{A}}_{43} & \bar{\boldsymbol{A}}_{44} & \mathbf{0}_{3\times3} & \mathbf{0}_{3\times3} & \mathbf{0}_{3\times3} & \boldsymbol{I}_{3\times3} & \mathbf{0}_{3\times3} \\ \mathbf{0}_{3\times3} & \mathbf{0}_{3\times3} & \bar{\boldsymbol{A}}_{53} & \mathbf{0}_{3\times3} & \mathbf{0}_{3\times3} & \bar{\boldsymbol{A}}_{56} & \bar{\boldsymbol{A}}_{57} & \bar{\boldsymbol{A}}_{58} & \mathbf{0}_{3\times3} \\ \mathbf{0}_{3\times3} & \mathbf{0}_{3\times3} & \mathbf{0}_{3\times3} & \mathbf{0}_{3\times3} & \bar{\boldsymbol{A}}_{65} & \mathbf{0}_{3\times3} & \bar{\boldsymbol{A}}_{67} & \mathbf{0}_{3\times3} & \bar{\boldsymbol{A}}_{69} \\ \mathbf{0}_{3\times3} & \mathbf{0}_{3\times3} & \bar{\boldsymbol{A}}_{73} & \mathbf{0}_{3\times3} & \mathbf{0}_{3\times3} & \bar{\boldsymbol{A}}_{76} & \bar{\boldsymbol{A}}_{77} & \bar{\boldsymbol{A}}_{78} & \bar{\boldsymbol{A}}_{79} \\ \mathbf{0}_{3\times3} & \mathbf{0}_{3\times3} & \mathbf{0}_{3\times3} & \bar{\boldsymbol{A}}_{84} & \mathbf{0}_{3\times3} & \mathbf{0}_{3\times3} & \bar{\boldsymbol{A}}_{87} & \bar{\boldsymbol{A}}_{88} & \bar{\boldsymbol{A}}_{89} \\ \mathbf{0}_{3\times3} & \mathbf{0}_{3\times3} & \mathbf{0}_{3\times3} & \mathbf{0}_{3\times3} & \mathbf{0}_{3\times3} & \mathbf{0}_{3\times3} & \bar{\boldsymbol{A}}_{97} & \bar{\boldsymbol{A}}_{98} & \mathbf{0}_{3\times3} \end{bmatrix}$$

where

$$\bar{\boldsymbol{A}}_{21} = n_0^2 \begin{bmatrix} 3 & 0 & 0 \\ 0 & 0 & 0 \\ 0 & 0 & -1 \end{bmatrix}, \quad \bar{\boldsymbol{A}}_{22} = 2n_0 \begin{bmatrix} 0 & 1 & 0 \\ -1 & 0 & 0 \\ 0 & 0 & 0 \end{bmatrix}, \quad \bar{\boldsymbol{A}}_{23} = \frac{3n_0^2}{R_0} \begin{bmatrix} -1 & 0 & 0 \\ 0 & 1 & 0 \\ 0 & 0 & 1 \end{bmatrix},$$

$$\bar{\boldsymbol{A}}_{25} = \frac{3n_0^2}{2R_0} \begin{bmatrix} 1 & 0 & 0 \\ 0 & 0 & 0 \\ 0 & 0 & 0 \end{bmatrix}, \quad \bar{\boldsymbol{A}}_{26} = \frac{3n_0^2}{2R_0} \begin{bmatrix} 0 & 0 & 1 \\ 0 & 0 & 0 \\ 0 & 0 & 0 \end{bmatrix}, \quad \bar{\boldsymbol{A}}_{34} = \begin{bmatrix} 2 & 0 & 0 \\ 0 & 1 & 0 \\ 0 & 0 & 1 \end{bmatrix},$$

$$\bar{\boldsymbol{A}}_{35} = \begin{bmatrix} 0 & 0 & 0 \\ 0 & 0 & 1 \\ 0 & 0 & 0 \end{bmatrix}, \qquad \bar{\boldsymbol{A}}_{37} = \begin{bmatrix} 0 & 0 & 0 \\ 0 & 0 & 0 \\ 1 & 0 & 0 \end{bmatrix}, \qquad \bar{\boldsymbol{A}}_{43} = \bar{\boldsymbol{A}}_{21}\,, \quad \bar{\boldsymbol{A}}_{44} = \bar{\boldsymbol{A}}_{22}\,,$$

$$\bar{\boldsymbol{A}}_{53} = 3n_0^2 \begin{bmatrix} 0 & 0 & 0 \\ 0 & 0 & 0 \\ 0 & 1 & 0 \end{bmatrix}, \qquad \bar{\boldsymbol{A}}_{56} = \begin{bmatrix} 2 & 0 & 0 \\ 0 & 1 & 0 \\ 2n_0 & 0 & 0 \end{bmatrix}, \qquad \bar{\boldsymbol{A}}_{57} = \begin{bmatrix} 0 & 0 & 0 \\ 0 & 1 & 0 \\ 0 & 0 & 0 \end{bmatrix},$$

$$\bar{\boldsymbol{A}}_{58} = \begin{bmatrix} 0 & 0 & 0 \\ 0 & 0 & 0 \\ 0 & 1 & 0 \end{bmatrix}, \quad \bar{\boldsymbol{A}}_{65} = n_0 \begin{bmatrix} 0 & 0 & -2 \\ 0 & -n_0 & 0 \\ 0 & 0 & 0 \end{bmatrix}, \qquad \bar{\boldsymbol{A}}_{67} = \begin{bmatrix} 0 & 0 & 0 \\ 0 & 0 & 0 \\ 0 & 0 & 2 \end{bmatrix},$$

$$\bar{\boldsymbol{A}}_{69} = \begin{bmatrix} 1 & 0 & 0 \\ 0 & 1 & 0 \\ 0 & 0 & 0 \end{bmatrix}, \quad \bar{\boldsymbol{A}}_{73} = 3n_0^2 \begin{bmatrix} 0 & 0 & 1 \\ 0 & 0 & 0 \\ 0 & 0 & 0 \end{bmatrix}, \qquad \bar{\boldsymbol{A}}_{76} = n_0^2 \begin{bmatrix} 0 & 0 & 0 \\ 0 & 0 & 0 \\ 0 & 0 & -1 \end{bmatrix},$$

$$\bar{\boldsymbol{A}}_{77} = \bar{\boldsymbol{A}}_{22}\,, \qquad \bar{\boldsymbol{A}}_{78} = \begin{bmatrix} 0 & 0 & 1 \\ 0 & 0 & 0 \\ 0 & 0 & 0 \end{bmatrix}, \qquad \bar{\boldsymbol{A}}_{79} = \begin{bmatrix} 0 & 0 & 0 \\ 0 & 1 & 0 \\ 0 & 0 & 1 \end{bmatrix},$$

$$\bar{\boldsymbol{A}}_{84} = 3n_0^2 \begin{bmatrix} 2 & 0 & 0 \\ 0 & 1 & 0 \\ 0 & 0 & 1 \end{bmatrix}, \quad \bar{\boldsymbol{A}}_{87} = n_0^2 \begin{bmatrix} 0 & 0 & 0 \\ 0 & 0 & 0 \\ -1 & 0 & 0 \end{bmatrix}, \qquad \bar{\boldsymbol{A}}_{88} = 2n_0 \begin{bmatrix} 0 & 2 & 0 \\ -1 & 0 & 0 \\ 0 & 0 & 0 \end{bmatrix},$$

$$\bar{\boldsymbol{A}}_{89} = 2n_0 \begin{bmatrix} 0 & 0 & 0 \\ 1 & 0 & 0 \\ 0 & 1 & 0 \end{bmatrix}, \quad \bar{\boldsymbol{A}}_{97} = n_0^2 \begin{bmatrix} 0 & 0 & 0 \\ 0 & -1 & 0 \\ 0 & 0 & -2 \end{bmatrix}, \qquad \bar{\boldsymbol{A}}_{98} = 2n_0 \begin{bmatrix} 0 & -2 & 0 \\ 0 & 0 & -1 \\ 0 & 0 & 0 \end{bmatrix}.$$

BIBLIOGRAPHY

[1] Elizabeth Buchen. Small satellite market observations. In *Proceedings of the 29th Conference on Small Satellites*, number SSC15-VII-7, pages 1–5, 2015.

[2] Stephen Clark. OneWeb selects Airbus to build 900 internet satellites. *Spaceflight Now*, `http://spaceflightnow.com/2015/06/15/oneweb-selects-airbus-to-build-900-internet-satellites`. Accessed: 15 October 2015.

[3] Peter B. de Selding. Facebook and Eutelsat lease Ka-band capacity to help connect Africa. *Space News*, `https://shar.es/15gLPB`. Accessed: 05 October 2015.

[4] Jeff Foust. The return of the satellite constellations. *The Space Review*, `http://www.thespacereview.com/article/2716/1`. Accessed: 15 October 2015.

[5] G. Tommei, A. Milani, and A. Rossi. Orbit determination of space debris: Admissible regions. *Celestial Mechanics and Dynamical Astronomy*, 97(4):289–304, April 2007.

[6] Nicholas J. Willis. *Bistatic Radar*. SciTech Publishing, Inc., Raleigh, NC, 2005.

[7] Zakhary N. Khutorovsky, Sergey Yu Kamensky, Nickolay N. Sbytov, and Kyle T. Alfriend. Comparison of different methods of LEO satellite orbit determination for a single pass through a radar. In *Proceedings of the AAS/AIAA Space Flight Mechanics Meeting*, volume 134 of *Advances in the Astronautical Sciences*, pages 71–88, February 2009.

[8] Kyle J. DeMars and Moriba K. Jah. Probabilistic initial orbit determination using radar returns. In *Proceedings of the 2013 AAS/AIAA Astrodynamics Specialist Conference*, number AAS 13-704, 2013.

[9] W.H. Clohessy and R.S. Wiltshire. Terminal guidance system for satellite rendezvous. *Journal of the Aerospace Sciences*, 27(9):653–358, 1960.

[10] James A. Chamberlin and James T. Rose. Gemini rendezvous program. *Journal of Spacecraft and Rockets*, 1(1):13–18, January 1964. doi: 10.2514/3.27585.

[11] J. Tschauner. Elliptic orbit rendezvous. *AIAA Journal*, 5(6):1110–1113, June 1967. doi: 10.2514/3.4145.

[12] Gabriella Gaias, Simone Damico, and Jean-Sebastien Ardaens. Angles-only navigation to a noncooperative satellite using relative orbital elements. *Journal of Guidance, Control, and Dynamics*, 37(2):439–451, 2014.

[13] David C. Woffinden and David K. Geller. Relative angles-only navigation and pose estimation for autonomous orbital rendezvous. *Journal of Guidance, Control, and Dynamics*, 30(5):1455–1469, 2007.

[14] Koji Yamanaka and Finn Ankersen. New state transition matrix for relative motion on an arbitrary elliptical orbit. *Journal of Guidance, Control, and Dynamics*, 25(1):60–66, 2002.

[15] Dong-Woo Gim and Kyle T. Alfriend. State transition matrix of relative motion for the perturbed noncircular reference orbit. *Journal of Guidance, Control, and Dynamics*, 26(6):956–971, 2003.

[16] William E. Wiesel. *Spaceflight Dynamics*. Aphelion Press, 2010.

[17] Jacob E. Darling, James S. McCabe, Henry J. Pernicka, and Kyle J DeMars. Linear and unscented covariance analysis for spacecraft close proximity relative navigation. In *Proceedings of the 24th AIAA/AAS Space Flight Mechanics Meeting*, number AAS 14-257, 2014.

[18] Mary T. Stringer, Brett Newman, T. Alan Lovell, and Ashraf Omran. Second order nonlinear initial value solution for relative motion using Volterra theory. In *Proceedings of the 23rd AAS/AIAA Space Flight Mechanics Meeting*, number AAS 13-469, pages 2133–2149, 2013.

[19] Keith A. LeGrand, Kyle J. DeMars, and Henry J. Pernicka. Initial relative orbit determination for close-in proximity operations. *Journal of Guidance, Control, and Dynamics*, 38:1833–1842, 2015. doi: 110.2514/1.G000933.

[20] David C. Woffinden and David K. Geller. Observability criteria for angles-only navigation. In *Proceedings of the AAS/AIAA Astrodynamics Specialist Conference*, number AAS 07-402, 2007.

[21] David C. Woffinden and David K. Geller. Observability criteria for angles-only navigation. *Aerospace and Electronic Systems, IEEE Transactions on*, 45(3): 1194–1208, July 2009. ISSN 0018-9251. doi: 10.1109/TAES.2009.5259193.

[22] David K. Geller and Itzik Klein. Angles-only navigation state observablity during orbital proximity operations. *Journal of Guidance, Control, and Dynamics*, 37 (6):1976–1983, 2014. doi: 10.2514/1.G000133.

[23] Laura M. Hebert, Andrew J. Sinclair, and T. Alan Lovell. Angles-only initial relative-orbit determination via maneuver. In *to appear, Proceedings of the 25th AAS/AIAA Space Flight Mechanics Meeting*, number AAS 15-3525, 2015.

[24] Brett Newman, T. Alan Lovell, Ethan Pratt, and Eric Duncan. Quadratic hexa-dimensional solution for relative orbit determination. In *Proceedings of the AIAA/AAS Astrodynamics Specialist Conference*, number AIAA 2014-4309, 2014. doi: 10.2514/6.2014-4309.

[25] Shay Segal, Avishy Carmi, and Pini Gurfil. Stereoscopic vision-based spacecraft relative state estimation. In *Proceedings of the AIAA Guidance, Navigation, and Control Conference and Exhibit*, 2009.

[26] Shay Segal, Avishy Carmi, and Pini Gurfil. Vision-based relative state estimation of non-cooperative spacecraft under modeling uncertainty. In *IEEE Aerospace Conference*, 2011. doi: 10.1109/AERO.2011.5747479.

[27] Shay Segal, Pini Gurfil, and K. Shahid. In-orbit tracking of resident space objects: A comparison of monocular and stereoscopic vision. *IEEE Transactions on Aerospace and Electronic Systems*, 50(1):676–688, January 2014. ISSN 0018-9251. doi: 10.1109/TAES.2013.120006.

[28] Dehann Fourie, Brent E Tweddle, Steve Ulrich, and Alvar Saenz-Otero. Flight results of vision-based navigation for autonomous spacecraft inspection of unknown objects. *Journal of Spacecraft and Rockets*, pages 2016–2026, 2014.

[29] Gkhan Inalhan, Michael Tillerson, and Jonathan P. How. Relative dynamics and control of spacecraft formations in eccentric orbits. *Journal of Guidance, Control, and Dynamics*, 25(1):48–59, 2002.

[30] David A. Vallado. *Fundamentals of Astrodynamics and Applications*. Microcosm Press, Hawthorne, CA, 2013.

[31] John E Prussing and Bruce A Conway. *Orbital Mechanics*. Oxford University Press, 1993.

[32] Richard H. Battin. *An Introduction to the Mathematics and Methods of Astrodynamics*. AIAA, 1999.

[33] Keith A. LeGrand and Kyle J. DeMars. Analysis of a second-order relative motion Lambert solver. In *Proceedings of the 2014 AIAA/AAS Astrodynamics Specialist Conference*, number AIAA 2014-4361, 2014. doi: 10.2514/6.2014-4361.

[34] B.L. van der Waerden. *Modern Algebra*, volume 2. Frederick Ungar Publishing Company, New York, 1931.

[35] Dinesh Manocha and Shankar Krishnan. Solving algebraic systems using matrix computations. *ACM SIGSAM Bulletin*, 30(4):4–21, 1996.

[36] Francis Sowerby Macaulay. *The Algebraic Theory of Modular Systems*. Cambridge University Press, 1916.

[37] Peter F. Stiller. An introduction to the theory of resultants. Technical report, ISC-96-02-MATH, Texas A&M University, Institute for Scientific Computation, 1996.

[38] Chanderjit Bajaj, Thomas Garrity, and Joe Warren. On the applications of multi-equational resultants. (88-826), 1988.

[39] Keith A. LeGrand, Kyle J. DeMars, and Jacob E. Darling. Solutions of multivariate polynomial systems using Macaulay resultant expressions. In *Proceedings of the 24th AAS/AIAA Space Flight Mechanics Meeting*, number AAS 14-229, 2014.

[40] Paul McCall, Gildo Torres, Keith A. LeGrand, Malek Adjouadi, Chen Liu, Jacob E. Darling, and Henry J. Pernicka. Many-core computing for space-based stereoscopic imaging. In *Proceedings of the IEEE Aerospace Conference*, 2013.

[41] John Canny. A computational approach to edge detection. *IEEE Transactions on Pattern Analysis and Machine Intelligence*, PAMI-8(6):679–698, Nov 1986. ISSN 0162-8828. doi: 10.1109/TPAMI.1986.4767851.

[42] Chris Harris and Mike Stephens. A combined corner and edge detector. In *Alvey Vision Conference*, volume 15, page 50. Manchester, UK, 1988. doi: 10.5244/C.2.23.

[43] Herbert Bay, Andreas Ess, Tinne Tuytelaars, and Luc Van Gool. Speeded-up robust features (SURF). *Computer Vision and Image Understanding*, 110(3): 346–359, 2008. doi: 10.1016/j.cviu.2007.09.014.

[44] Gabe Sibley, Larry Matthies, and Gaurav Sukhatme. Bias reduction and filter convergence for long range stereo. In Sebastian Thrun, Rodney Brooks, and Hugh Durrant-Whyte, editors, *Robotics Research*, volume 28 of *Springer Tracts in Advanced Robotics*, pages 285–294. Springer Berlin Heidelberg, 2007. ISBN 978-3-540-48110-2. doi: 10.1007/978-3-540-48113-3_26. URL `http://dx.doi.org/10.1007/978-3-540-48113-3_26`.

[45] Daniele Mortari and Manoranjan Majji. Multiplicative measurement model. *The Journal of the Astronautical Sciences*, 57(1-2):47–60, 2009. doi: 10.1007/BF03321493.

[46] Keith A. LeGrand. Initial relative orbit determination using stereoscopic imaging and Gaussian mixture models. In *Proceedings of the 27th Conference on Small Satellites*, number SSC13-VIII-6, pages 1–12, 2013.

[47] Chris A. Sabol, Alan Segerman, Aaron Hoskins, Bryan Little, Paul W. Schumacher Jr., and Shannon Coffey. Search and determine integrated environment (SADIE) for space situational awareness. Technical report, Air Force Research Laboratory, Directed Energy Directorate, Kihei, 2012.

[48] Keith A. LeGrand, Kyle J. DeMars, and Henry J. Pernicka. Bearing-only initial relative orbit determination. *Journal of Guidance, Control, and Dynamics*, 38: 1699–1713, 2015. doi: 10.2514/1.G001003.

[49] Daniel L. Alspach and Harold W. Sorenson. Nonlinear bayesian estimation using Gaussian sum approximations. *IEEE Transactions on Automatic Control*, 17(4): 439–448, 1972. ISSN 0018-9286. doi: 10.1109/TAC.1972.1100034.

[50] Rudolph van der Merwe and Eric A. Wan. Gaussian mixture sigma-point particle filters for sequential probabilistic inference in dynamic state-space models. In *IEEE International Conference on Acoustics, Speech, and Signal Processing*, volume 6, pages VI–701–4, 2003. doi: 10.1109/ICASSP.2003.1201778.

[51] Simon J. Julier and Je rey K. Uhlmann. Unscented Filtering and Nonlinear Estimation. *Proceedings of the IEEE*, 92(3):401–422, 2004. ISSN 0018-9219. doi: 10.1109/JPROC.2003.823141.

[52] Rudolph van der Merwe and Eric A. Wan. The square-root unscented Kalman filter for state and parameter-estimation. In *IEEE International Conference on Acoustics, Speech and Signal Processing*, volume 6, pages 3461–3464, 2001. doi: 10.1109/ICASSP.2001.940586. URL `http://dx.doi.org/10.1109/ICASSP.2001.940586`.

[53] Lloyd N. Trefethen and David Bau III. *Numerical Linear Algebra*, volume 50. Siam, 1997.

[54] Simo Särkkä. *Bayesian Filtering and Smoothing*. Cambridge University Press, 2013.

[55] Rudolph van der Merwe. *Sigma-point Kalman Filters for Probabilistic Inference in Dynamic State-space Models*. PhD thesis, Oregon Health & Science University, 2004.

[56] David K. Geller and T. Alan Lovell. Initial relative orbit determination performance analysis in cylindrical coordinates using angles-only measurements. In *Proceedings of the 24th AAS/AIAA Space Flight Mechanics Meeting*, number AAS 14-212, 2014.

[57] United Nations. Technical report on space debris. Technical Report A/AC.105/720, 1999.

[58] Aubrey B. Poore and Nenad Rijavec. A Lagrangian relaxation algorithm for multidimensional assignment problems arising from multitarget tracking. *SIAM Journal on Optimization*, 3:544–563, 1993. doi: 10.1137/0803027.

[59] Samuel S. Blackman. Multiple hypothesis tracking for multiple target tracking. *IEEE Aerospace and Electronic Systems Magazine*, 19(1):5–18, 2004.

[60] Kyle J. DeMars, Islam I. Hussein, Carolin Frueh, Moriba K. Jah, and R. Scott Erwin. Multiple object space surveillance tracking using finite set statistics. *Journal of Guidance, Control, and Dynamics*, pages 1741–1756. doi: 10.2514/1.G000987.

[61] Brandon A. Jones, Steven Gehly, and Penina Axelrad. Measurement-based birth model for a space object cardinalized probability hypothesis density filter. In *Proceedings of the 2014 AIAA/AAS Astrodynamics Specialist Conference*, number AIAA 2014-4311, 2014.

[62] Ronald P.S. Mahler. PHD filters of higher order in target number. *IEEE Transactions on Aerospace and Electronic Systems*, 43(4):1523–1543, October 2007. ISSN 0018-9251. doi: 10.1109/TAES.2007.4441756.

[63] Ba-Tuong Vo, Ba-Ngu Vo, and Antonio Cantoni. Analytic implementations of the cardinalized probability hypothesis density filter. *IEEE Transactions on Signal Processing*, 55(7):3553–3567, July 2007. ISSN 1053-587X. doi: 10.1109/TSP.2007.894241.

[64] Keith A. LeGrand and Kyle J. DeMars. Relative multiple space object tracking using intensity filters. In *18th International Conference on Information Fusion (Fusion)*, pages 1253–1261. IEEE, 2015.

[65] Ba-Tuong Vo. *Random Finite Sets in Multi-Object Filtering*. PhD thesis, The University of Western Australia, 2008.

[66] Ronald P.S. Mahler. *Statistical Multisource-Multitarget Information Fusion*. Artech House Boston, 2007.

[67] Ba-Tuong Vo, Ba-Ngu Vo, and Antonio Cantoni. The cardinalized probability hypothesis density filter for linear gaussian multi-target models. In *Information Sciences and Systems, 2006 40th Annual Conference on*, pages 681–686, March 2006. doi: 10.1109/CISS.2006.286554.

[68] Andrew H. Jazwinski. *Stochastic Processes and Filtering Theory*. Courier Corporation, 2007.

[69] Edward Rosten and Tom Drummond. Fusing points and lines for high performance tracking. In *Tenth IEEE International Conference on Computer Vision*, volume 2, pages 1508–1515. IEEE, 2005.

[70] Edward Rosten and Tom Drummond. Machine learning for high-speed corner detection. In *Computer Vision–ECCV 2006*, pages 430–443. Springer, 2006.

[71] Kira Michelle Jorgensen. *Using Reflectance Spectroscopy to Determine Material Type of Orbital Debris*. 2000.

[72] Laetitia Lamard, Roland Chapuis, and Jean-Philippe Boyer. CPHD filter addressing occlusions with pedestrians and vehicles tracking. In *2013 IEEE Intelligent Vehicles Symposium (IV)*, pages 1125–1130, June 2013. doi: 10.1109/IVS.2013.6629617.

[73] Ya-Dong Wang, Jian-Kang Wu, A.A. Kassim, and Weimin Huang. Data-driven probability hypothesis density filter for visual tracking. *IEEE Transactions on Circuits and Systems for Video Technology*, 18(8):1085–1095, Aug 2008. ISSN 1051-8215.

[74] Ozgur Erdinc, Peter Willett, and Stefano Coraluppi. The Gaussian mixture cardinalized PHD tracker on MSTWG and SEABAR'07 datasets. In *FUSION*, pages 1–8, 2008.

[75] Ba-Ngu Vo and Wing-Kin Ma. The Gaussian mixture probability hypothesis density filter. *IEEE Transactions on Signal Processing*, 54(11):4091–4104, Nov 2006. ISSN 1053-587X.

[76] Kyle J. DeMars and James S. McCabe. Tracking of the LANDSAT 2 rocket body primary breakup. In *Proceedings of the 2015 AAS/AIAA Space Flight Mechanics Meeting*, number AAS 15-420, 2015.

[77] Trevor Hastie, Robert Tibshirani, Jerome Friedman, and James Franklin. The elements of statistical learning: Data mining, inference and prediction. 2005.

[78] Dominic Schuhmacher, Ba-Tuong Vo, and Ba-Ngu Vo. A consistent metric for performance evaluation of multi-object filters. *IEEE Transactions on Signal Processing*, 56(8):3447–3457, 2008.

[79] Daniel E. Clark, Kusha R. Panta, and Ba-Ngu Vo. The GM-PHD filter multiple target tracker. In *9th International Conference on Information Fusion*, pages 1–8, July 2006. doi: 10.1109/ICIF.2006.301809.

VITA

Keith LeGrand spent his childhood years in the small village of Kelso, Missouri. After many cornfield model rocket launches and the denied request to make homemade rocket fuel on his parent's barbecue grill, Keith decided to pursue a professional education in aerospace engineering at the Missouri University of Science and Technology in Rolla, Missouri. Through his work on the Missouri S&T satellite team, Keith developed a passion for astrodynamics and state estimation. During the course of his undergraduate education, he participated in internships with the Air Force Research Laboratory Space Vehicles Directorate, Garmin International, and Sandia National Laboratories. Through the sponsorship of Sandia National Laboratories, Keith received his MS in Aerospace Engineering from the Missouri University of Science and Technology in December, 2015.